

INDENTATION FRACTURE OF GALLIUM ARSENIDE

THÈSE N° 3864 (2007)

PRÉSENTÉE LE 31 AOÛT 2007

À LA FACULTÉ DES SCIENCES ET TECHNIQUES DE L'INGÉNIEUR
LABORATOIRE DE CONCEPTION DE SYSTÈMES MÉCANIQUES
PROGRAMME DOCTORAL EN SYSTÈMES DE PRODUCTION ET ROBOTIQUE

ÉCOLE POLYTECHNIQUE FÉDÉRALE DE LAUSANNE

POUR L'OBTENTION DU GRADE DE DOCTEUR ÈS SCIENCES

PAR

Cédric POUVREAU

DEA de mécanique des matériaux et des fluides, Université Rennes 1, France
et de nationalité française

acceptée sur proposition du jury:

Prof. R. Glardon, président du jury
Prof. J. Giovanola, Dr J.-M. Breguet, directeurs de thèse
Dr W. Clegg, rapporteur
Prof. E. Le Bourhis, rapporteur
Dr J. Michler, rapporteur



ÉCOLE POLYTECHNIQUE
FÉDÉRALE DE LAUSANNE

Suisse
2007

Contents

Remerciements	IX
Abstract	X
Résumé	XI
1 Introduction	1
1.1 Context	2
1.2 Motivation for the Work	3
1.3 Methodology	4
1.3.1 Approach	4
1.3.2 Methods	4
1.3.3 Scope of the Investigation	5
1.4 Summary of Results	6
1.5 Original Contributions	6
1.6 Document Structure	7
Bibliography	8
2 State of the Art	9
2.1 Structure and Properties of GaAs	10
2.2 Deformation of GaAs under Indentation	13
2.2.1 Introduction to Dislocations in GaAs	13
2.2.2 Deformation Mechanisms under Indentation of GaAs	15
2.2.3 Investigation of Indenter Geometries	16
2.3 Nomenclature of Cracking Systems	17
2.3.1 Half-Penny Cracks	18
2.3.2 Palmqvist Cracks	18
2.3.3 Lateral Cracks	19
2.4 Indentation Fracture Mechanics	20
2.4.1 Elements of Fracture Mechanics	20
2.4.2 Application to Indentation Fracture	23
2.4.3 Special Applications to Fracture of GaAs	25
2.4.4 Semiconductor Dicing	26
2.5 Summary	26
Bibliography	28
3 Experimental Procedures	33
3.1 Cathodoluminescence	34
3.2 Indenters	35
3.2.1 Wedge Indenter	35
3.2.2 Conical Indenters	36

3.2.3	Pyramidal Indenters	36
3.2.3.1	Cube Corner	36
3.2.3.2	Vickers	37
3.3	Sample Preparation	38
3.3.1	Cross-Sectioning of Indentations	38
3.3.2	Focused Ion Beam (FIB)	39
3.4	Mechanical Testing Instruments	41
3.4.1	Nanoindenter XP	41
3.4.2	In-situ SEM Indenter	41
	Bibliography	43
4	Crack Morphologies & Cracking Sequence	45
4.1	Introduction	46
4.2	Wedge Indenters	46
4.2.1	Results	46
4.2.1.1	Wedge 60° Indenter	46
4.2.1.2	Wedge 120° Indenter	50
4.2.2	Discussion	52
4.2.2.1	Load-Displacement Curves	52
4.2.2.2	Analysis of the Half-Penny Cracks	59
4.2.2.3	Palmqvist Cracks, Lateral Cracks and Flaking	63
4.3	Point Indenters	67
4.3.1	Results	67
4.3.1.1	Conical 60°	67
4.3.1.2	Conical 120°	71
4.3.1.3	Cube Corner	73
4.3.1.4	Vickers Indenter	76
4.3.1.5	Summary	78
4.3.2	Discussion	80
4.3.2.1	Load-Displacement Curves	80
4.3.2.2	Cracking Patterns Around Point Indenters	82
4.3.2.3	Prediction of Crack Growth	83
4.4	Conclusions	87
	Bibliography	91
5	Crack Initiation Mechanisms	93
5.1	Introduction	94
5.2	Results	94
5.2.1	The Case of Wedge Indenters	94
5.2.1.1	Effect of the Apex Angle	95
5.2.1.2	Effect of Crystal Orientation	100
5.2.2	The Case of Point Indenters	104
5.2.2.1	Conical Indenters	104
5.2.2.2	Pyramidal Indenters	106
5.3	Discussion	108
5.3.1	Perfect Dislocations or Micro-twinning	108
5.3.2	Arrangement of Dislocations around Indentations	111
5.3.3	The Role of the Indenter Shape	113
5.4	Conclusions	116
	Bibliography	117

6	Practical Applications	121
6.1	Experimental Procedure	122
6.2	Results and Discussion	122
6.3	Conclusions	128
7	Conclusions and Perspectives	129
7.1	Work Overview and Main Contributions	130
7.1.1	Indentation Cracking in GaAs	130
7.1.1.1	Wedge Indenters	130
7.1.1.2	Point Indenters	131
7.1.2	Deformation and Crack Nucleation Mechanisms	131
7.1.3	Application to Dicing of Commercial Lasers	132
7.1.4	Indentation vs Scratching: Advantages and Drawbacks	133
7.1.4.1	Advantages	133
7.1.4.2	Drawbacks	133
7.1.4.3	Practical Guidelines for Dicing of GaAs	133
7.1.5	Original Contributions	134
7.2	Perspectives	134
7.2.1	Crack initiation and propagation	134
7.2.2	Deformation mechanisms	135
7.2.3	In-Situ SEM Testing and Extension of the Work to Other III-V Semiconductors	136
	Bibliography	136
A	Microscopy techniques	137
A.1	Atomic Force Microscopy (AFM)	138
A.1.1	Principle	138
A.1.2	Operating Modes	138
A.1.3	AFM/SEM Comparison	139
A.2	Electron Microscopy	139
A.2.1	Operating Principle of Electron Microscopes	139
A.2.2	Transmission Electron Microscope(TEM)	140
A.2.3	Scanning Electron Microscope(SEM)	141
	Bibliography	142
B	Methodology for Subsurface Damage Determination	143
C	Finite Element Simulations	145
	Bibliography	149

List of Figures

1.1	Singulation process	3
1.2	Micrographs of particles and cracks formed under scratching	4
2.1	Photography of a wafer	10
2.2	GaAs Young's modulus	11
2.3	Unit cell of GaAs	12
2.4	Important crystal planes in GaAs	12
2.5	Schematic view of a dislocation loop	13
2.6	Stacking sequence of $\{111\}$ planes in GaAs	14
2.7	Schematic view of the half-penny crack system	18
2.8	Schematic view of Palmqvist crack system	19
2.9	Schematic view of the lateral crack system	19
2.10	Energetic analysis using the compliance method	22
2.11	Center Loaded Half-Penny Crack	24
3.1	Experimental setup for cathodoluminescence investigations	35
3.2	Schematic view of the wedge indenter	36
3.3	HRSEM micrograph of conical indenters	37
3.4	Schematic view of the cube corner indenter	37
3.5	Schematic view of the Vickers indenter	38
3.6	The transverse cross-sectioning procedure	38
3.7	The longitudinal cross-sectioning procedure	39
3.8	Examples of transverse and longitudinal cross-sections	39
3.9	Preparation of a TEM Lamella	40
3.10	In-situ SEM microindenter setup	42
4.1	In-situ SEM indentation with a wedge 60°	47
4.2	Wedge 60° cross-sections of a 500 mN indentation	48
4.3	Wedge 60° cross-section of a 200 mN indentation	49
4.4	Longitudinal cross-sections	50
4.5	In-situ SEM indentation with a wedge 120° indenter	51
4.6	Cross-section of a wedge 120° indentation	52
4.7	Evolution of the pop-in load with load rate	53
4.8	Evolution of the tensile stress with edge radii	54
4.9	Cracking sequence in an edge indentation	55
4.10	Wedge 60° indentation curves with partial unload	57
4.11	Indentation curves 60° wedge indenter	59
4.12	Longitudinal cross-section of a wedge 60° indentation	61

4.13	Weight function for a center loaded half-penny crack	62
4.14	Evolution of crack size with the indentation load	63
4.15	F_T versus the indenter angle	64
4.16	Palmqvist crack repartition	65
4.17	Chips locations for wedge 60°	66
4.18	Lateral cracks extension at various loading rate	67
4.19	Cone 60° in-situ SEM indentation	68
4.20	Top view of a conical 60° indentation	69
4.21	Cross-section of cone 60° indentations	70
4.22	Cone 120° in-situ SEM indentation	71
4.23	Residual imprint of a conical 120° indentation	72
4.24	Cross-section of cone 120°	73
4.25	Cracking sequence under a cube corner indentation	74
4.26	Cross-section of a cube corner indentation	75
4.27	SEM micrograph of a $\langle 100 \rangle$ Vickers indentation	76
4.28	SEM micrograph of a $\langle 110 \rangle$ Vickers indentation	77
4.29	Cross-section of a Vickers indentation	78
4.30	Cracking patterns under wedge and point indenters	79
4.31	Time-displacement curve	81
4.32	Repartition of cracks for Vickers indentations	83
4.33	Crack size evolution for point indenters (1)	85
4.34	Crack size evolution for point indenters (2)	86
4.35	Edge and face first configurations	89
5.1	SE and CL images of the cross-section of a 60° wedge indentation	94
5.2	CL micrographs for wedge 60° and wedge 120°	95
5.3	TEM lamella of a wedge 60° indentation	96
5.4	SAED - wedge 60°	97
5.5	TEM micrograph - wedge 120°	97
5.6	First SAED-wedge 120°	98
5.7	Second SAED-wedge 120°	99
5.8	Wedge 90° indentation-(001)	99
5.9	TEM micrograph wedge 60° lamella $\{\bar{1}\bar{1}0\}$	100
5.10	SAED pattern of $\{\bar{1}\bar{1}0\}$ wedge 60° indentation	101
5.11	Schematic of the diverging/converging slip patterns	101
5.12	Wedge 90° indentation-(110)	102
5.13	Comparison of slip traces below conical indenters	104
5.14	AFM view of a conical 60° indentation	105
5.15	AFM micrograph of a cube corner indentation	106
5.16	AFM view of a Vickers indentation	107
5.17	Schematic of the surface slip traces around point indenters	108
5.18	Wedge 60° indentation curves along orthogonal $\langle 110 \rangle$ orientations	111
5.19	Schematic view of the Burger's vector configurations	112
5.20	AFM scan of slip bands	114
5.21	Initiation sites in cube corner indentations	115
6.1	Structure of a laser	123
6.2	Indentation curves for single indentations	124
6.3	Indentation curves of 300 mN indentations	124
6.4	60° wedge indentations, maximum loads of 100 and 200 mN	125

6.5	60° wedge indentations, maximum loads of 300, 400 and 500 mN	125
6.6	Optical micrographs showing different chipping configurations . .	127
6.7	Results for single indentations	128
7.1	The distributed load configuration modelling wedge indentation.	135
A.1	AFM setup	138
A.2	The Hitachi S-4800 FEG-SEM and the working principle of a SEM.	140
A.3	Description of the TEM	141
B.1	Longitudinal cross-section of a 60° wedge indentation	144
B.2	Binarised image of 60° wedge indentation	144
C.1	Meshing of the substrate	146
C.2	Contact pressure distributions	148

List of Tables

1.1	Advantages and drawbacks of different singulation methods	2
2.1	Mechanical properties of GaAs.	11
2.2	Types of dislocations	13
2.3	Dislocation structures around Vickers indentation	16
2.4	Toughness values by several authors	25
4.1	Coefficients Λ for the different crack systems	87
4.2	Summary of the results	88
5.1	Summary of the results obtained from TEM observations	103
6.1	Classification of the levels of chipping-out	126
C.1	Stress and plastic strain values for GaAs	147

Notations

Symbol	Description
$\{111\}$	Family of crystallographic planes
(111)	Single crystallographic plane
$\langle 111 \rangle$	Family of crystallographic direction
$[111]$	Single crystallographic direction
a	Depth of the half-penny crack (μm)
c	Length of the half-penny crack (μm)
E	Young's modulus (GPa)
F_T	Tangential force (mN)
F_ϕ	Weight function of the CLHPC model
G	Shear modulus (GPa)
H	Hardness (GPa)
K	Stress Intensity Factor ($\text{MPa}\cdot\sqrt{\text{m}}$)
K_{Surf}	Stress Intensity Factor at the surface ($\text{MPa}\cdot\sqrt{\text{m}}$)
K_{Depth}	Stress Intensity Factor in the depth ($\text{MPa}\cdot\sqrt{\text{m}}$)
K_{Ic}	Plane strain fracture toughness ($\text{MPa}\cdot\sqrt{\text{m}}$)
K_c	Indentation fracture toughness ($\text{MPa}\cdot\sqrt{\text{m}}$)
k_B	Boltzmann constant
P	Indentation load (mN)
T	Temperature ($^\circ\text{C}$)
U	Activation energy (J)
U_S	Energy released in crack formation (J)
ε	Strain
$\dot{\varepsilon}$	Strain rate (s^{-1})
γ_c	Cleavage surface energy (J/m^2)
Λ	Slope of the P - $c^{3/2}$ curves
ϕ	Dimensionless factor representative of boundary conditions
ψ	Indenter semi-angle ($^\circ$)
$\sigma_{tensile}$	Tensile stress (also S11) (GPa)
τ	Shear stress (GPa)
τ_{eff}	Effective shear stress (GPa)
τ_{uy}	Upper yield stress (GPa)

Remerciements

Mes remerciements vont tout d'abord à Jacques Giovanola et Jean-Marc Breguet mes directeurs et co-directeurs de thèse ainsi qu'à Kilian Wasmer de l'EMPA Thun. Vos encouragements, suggestions et discussions furent une aide précieuse qui m'ont permis de progresser tout au long de ces quatre années. J'ai réellement apprécié travailler avec vous.

Merci à Rémy Glardon pour avoir présidé le jury ainsi qu'au différents membres du jury pour leur disponibilité, leurs commentaires et corrections éclairées sur le manuscrit.

Ce travail a été réalisé en grande partie à l'EMPA Thun grâce à Johann Michler et Lukas Rohr. Qu'ils soient remerciés pour leur soutien tant moral que financier. Merci également à Christophe Ballif pour m'avoir épaulé lors de mes premiers pas en thèse à l'EMPA.

Un immense merci à Daniel Schulz de Bookham AG, Zürich pour sa gentillesse, sa disponibilité, sa patience ainsi que pour le soutien matériel lors de ce projet. J'espère que d'autres collaborations fructueuses verront le jour.

Cette thèse n'aurait sans doute pas vu le jour sans les idées de Rodolfo Rabe qui a conçu et réalisé cet outil magique qu'est l'indenteur in-situ. Mille fois merci pour cette réalisation unique ! Merci à Aïcha Hessler-Wyser du CIME pour les clichés TEM qui illustrent agréablement le chapitre 5 et à Jean-Daniel Ganière du département de physique pour les images en cathodoluminescence. Merci à tout les deux pour tout ce temps passé à m'expliquer les subtilités de la microscopie électronique. Merci à Joy Tharian de l'EMPA Dübendorf pour le soin apporté à la préparation des échantillons TEM et à Gerhard Buerki pour le temps passé à m'initier aux joies du SEM haute résolution.

Mes remerciements vont également à tout mes collègues qu'ils soient de Lausanne, de Thun ou d'ailleurs pour m'avoir permis de travailler dans un environnement chaleureux. Un grand merci à Adrien Bidiville, Walter Driesen, Robert Dunsch, Rémy Gassilloud, Vincent Le Houérou, Philippe Kern pour tous les bons moments passés (et également les futurs...). Merci à Claire Chabanel et Katrin Gurtner pour m'avoir aidé durant tout ce temps à surmonter les obstacles administratifs qui agrémentent le parcours du doctorant. Merci enfin à toutes les personnes impliquées de près ou de loin dans ce travail et qui n'ont pas été citées nommément ... la liste est longue et le nombre de pages limité mais je ne vous oublie pas... soyez donc remerciés pour votre contribution !

Une thèse est par essence un exercice long et difficile au cours duquel le moral du doctorant est comparable à un train lancé à vive allure sur des montagnes russes. Dans ce cas, le soutien familial est une des clés fondamentales du bon déroulement d'une thèse. Un grand merci à tout mes proches, parents, beaux-parents, frères, amis pour leur soutien.

Le plus important de tout, tout mon Amour à Sandrine qui à toujours cru en moi, même dans les moments les plus difficiles. Merci pour ton soutien, ta patience et ta générosité. Merci de t'être occupée de moi pendant ces quatre longues années...

Cette thèse à laquelle tu as largement contribué t'es dédiée... je t'aime.

Abstract

The scribe and break technique (or dicing) is a widely employed method in the industry of semiconductors to separate infrared laser diodes made from gallium arsenide (GaAs). The scribing step allows to create a precursor crack which is then propagated during the breaking step, along preferential $\{110\}$ cleavage planes of GaAs. The main drawback of the scribing process is that it generates a lot of undesirable cracks and particles that degrade the performances of devices. In this dissertation, we have investigated the indentation process as a possible way to replace the scribing operation.

For that purpose, we have investigated the morphology of the crack field and the cracking sequence as a function of the indenter geometry (shape, apex angle) and experimental conditions (maximal load, loading rate). Such investigations have been made with the help of a new tool: the in-situ SEM instrumented indentation which allows us to establish the cracking sequence and to correlate direct observations with the load-displacement histories. A new experimental technique has also been developed: cleavage cross-sectioning techniques allow us to determine the morphology of the crack field beneath the surface. The second research axis was focused on the interaction between deformation mechanisms and crack initiation. These investigations have been conducted with the help of Transmission Electron Microscopy (TEM) and cathodoluminescence.

In the first part of the dissertation, we have shown that acute wedge indenters with an included angle of 60° promote the formation of a well defined half-penny crack, the nucleation of which is affected by load rate and indenter radius. The relation between the final half-penny crack size and the maximum indentation load was made with the help of a fracture mechanics model. The crack field has been compared for several indenter shape including conical (60° and 120° apex angles), cube corner and Vickers indenters.

In the second part of this dissertation we have determined that the indenter apex angle influences the slip systems that are activated and the nature of dislocations that are found under the indenter. In particular, we have shown that below 60° wedge indenters, mainly diverging slip systems are activated whereas under obtuse wedge indenters, mainly converging slip systems are activated. The converging pattern predominant under obtuse indenters is correlated with a delayed half-penny crack formation and is so interpreted as a plastic shielding phenomenon.

Some experiments have been performed on commercial devices under production conditions. Although some adjustments are needed to reduce the chipping-out effect that occurs at the indenter extremities, the results are encouraging.

Keywords: in-situ SEM indentation, cross-sectioning, half-penny crack, dislocations, microtwinning, divergent/convergent, cathodoluminescence, TEM.

Résumé

La séparation des lasers est une opération cruciale qui intervient dans la phase finale du procédé de fabrication des lasers semi-conducteurs à base d'arséniure de gallium (GaAs). Cette opération comporte deux étapes essentielles: premièrement une fissure est initiée en rayant la surface du semi-conducteur avec un outil diamanté puis les lasers sont séparés en propageant cette fissure le long des plans de clivage préférentiels. L'inconvénient majeur du procédé de rayage est qu'il nécessite une optimisation fine de l'outil et des paramètres utilisés (vitesse de rayage, force), afin de réduire les phénomènes d'écaillage et de fissuration parasites qui peuvent fortement dégrader les performances des composants.

Le but de cette thèse est d'étudier le procédé d'indentation comme un moyen de remplacer l'opération de rayage. Dans un premier temps, nous nous attachons à décrire la morphologie des différents types de fissures et la séquence de formation de ces fissures en fonction de la géométrie de l'indenteur. Dans un deuxième temps, nous étudions l'interaction entre les mécanismes de déformation de GaAs sous l'indenteur et la formation des fissures. La première partie de l'étude utilise un outil novateur: l'indentation instrumentée dans un Microscope Électronique à balayage. Cet outil permet d'étudier *in-situ* la formation des fissures et de relier les observations en surface à la courbe charge-déplacement. De nouvelles techniques telles que le sectionnement transversal ou longitudinal d'indentations en utilisant les plans de clivage de GaAs ont été développées pour étudier la morphologie des fissures en dessous de la surface.

Parmi les résultats obtenus, nous avons montré que sous un indenteur wedge, une fissure semi-elliptique se forme durant la phase de charge. Lors d'indentations dans la direction [110], l'initiation et la propagation soudaine de cette fissure sont associées avec un déplacement, couramment appelé pop-in, dans la courbe charge-déplacement. L'évolution de la taille de cette fissure semi-elliptique peut être corrélée à la charge d'indentation en utilisant un modèle de mécanique de la rupture décrivant l'évolution de K le long du front de fissure. L'étude de différentes formes d'indenteurs montre qu'il y a une compétition entre les effets dus à la forme de l'indenteurs et ceux liés à la structure cristalline de GaAs.

En ce qui concerne les mécanismes d'initiation des fissures semi-elliptiques, nous avons déterminé que l'angle de l'indenteur joue un rôle prépondérant dans les mécanismes de déformation qui prennent place sous l'indenteur. En particulier, les systèmes de glissement activés sous un indenteur wedge aigu (angle inclus 60°) sont divergents alors que les systèmes de glissement activés deviennent principalement convergents lorsque l'angle inclus de l'indenteur est augmenté. Cette distinction est cruciale pour la formation de fissures de type semi-elliptiques et la présence de systèmes convergents tend à retarder leur apparition.

Pour finir, nous avons démontré que l'utilisation d'un indenteur wedge pour séparer des lasers est possible dans un contexte industriel. Cette utilisation est cependant liée à l'optimisation de certains paramètres d'indentation et de clivage.

Mots-clés: indentation in-situ, fissure semi-elliptique, indenteur wedge, dislocation, micromaclage, divergent/convergent, cathodoluminescence, TEM.

Chapter 1

Introduction

1.1 Context

Nowadays, semiconductors from the III-V family, of which gallium arsenide (GaAs) is a technologically important member, are used for a variety of engineering applications. Due to their particular opto-electronic properties, the possible applications range from high efficiency solar cells to laser diodes employed in telecommunication networks.

In this last example, the fabrication process is very complex and requires numerous steps, such as epitaxial growth of layers, patterning, etc. . . . The final step before packaging consists of separating the devices from each other. This singulation process is a critical step since the quality of the mirror faces, at each extremities of the device, acts upon the final performances of the laser. Different ways to singulate the lasers are available on the market. A review of the different methods with their main advantages and drawbacks is given in Table 1.1.

Process	Minimum line width	Particle generation	Complex shapes
Scribe & break	10 μm	could	no
LaserJet	40 μm	no	yes
Sawing	60 μm	yes	yes

Table 1.1: Advantages and drawbacks of different singulation methods

The sawing process generates a lot of debris and is generally limited to microprocessors and other silicon components. The main interest of the LaserJet method is the possibility to obtain complex forms and so it is particularly well suited for MEMS applications.

In the field of opto-electronic devices, mirror surfaces need to be atomically flat over a range of several millimeters. The scribe and break technique is to our knowledge the only method that meets this requirement. Another advantage of this technique is that the space between devices is reduced when compared to other methods. This reduction allows to increase the number of processed lasers per wafer. The main drawbacks of the scribe and break method include the deviation of cracks from the desired path and the generation of particles coming from the scratching process.

The scribe and break technique consists of scratching first the wafer surface with a diamond tool. The scratching process induces the so-called median crack which then serves as a precursor defect for the subsequent cleavage step [1]. Later, the devices are separated by propagating the median crack throughout the wafer using the $\{110\}$ preferential cleavage planes of GaAs [2]. This last operation consists of several steps where the wafer is progressively divided into cells, bars and single devices as depicted in Figure 1.1.

In the context of the CTI project "Nanoclé" conducted in collaboration with Bookham AG in Zürich, problems linked to the breaking step of the process of GaAs laser were addressed [1, 2, 3, 4]. In particular, the deviation of precursor cracks from the prescribed path was investigated with the help of Finite Element simulations and significant improvements were made on this process.

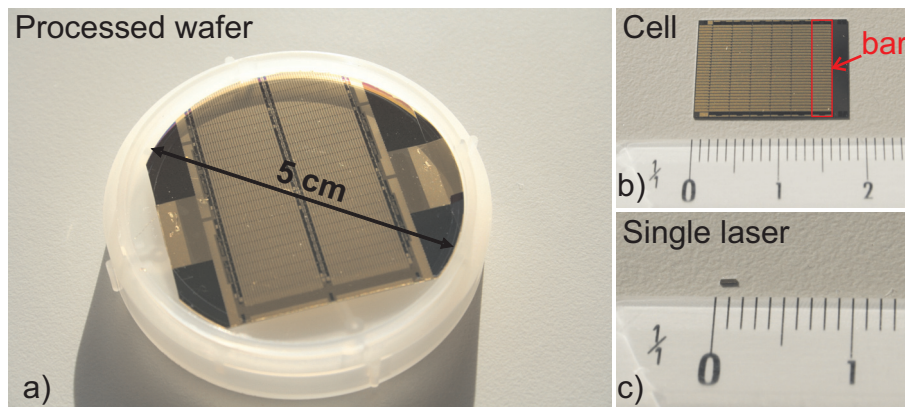


Figure 1.1: The different steps from a) a processed wafer to b) a single cell with 7 bars and finally c) a single device.

Although some general guidelines were drawn concerning the reduction of particles generation during the scratching process, the high number of controlling parameters made it difficult to optimize the process in the limited time of the project.

This dissertation addresses the problem of indentation fracture of GaAs as a precursor step to the technologically important problem of cleavage singulation.

1.2 Motivation for the Work

One of the main issue of the scribe and break technique remains the creation of particles. These particles lead to problems during laser packaging, degrade device performances when sticking on mirror cavities or pollute the clean environment necessary for the process.

They can form in two ways:

- Small particles form during the scribing process and scatter away from the scratch track as illustrated in Figure 1.2 a);
- Cracks developing into a chevron shape as depicted in Figure 1.2 b) extend during the cleavage step driven by the applied cleavage load and merge with lateral cracks propagating under the surface to form big flakes.

The scratching load and speed, as well as the indenter shape and the crystal orientation are some of the most important parameters controlling the median crack nucleation and particle generation in GaAs, as shown by Wasmer *et al.* in a previous study [1, 4].

Although some adjustments were made to reduce particle generation by playing with the parameters mentioned above, it is difficult to find the right compromise between reduced chipping-out and a size of the median crack sufficient for well controlled cleavage.

In parallel, preliminary studies conducted by C. Ballif [5] and J.-M. Solletti, reported in [3], on indentation of GaAs, showed that reduced chip formation usually takes place under respectively Knoop and wedge indentations. Further

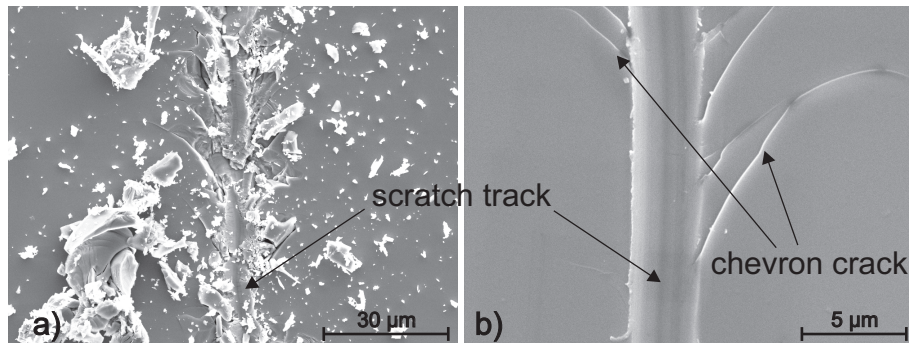


Figure 1.2: SEM micrographs showing a) particles formed during scratching at high loads and b) chevron cracks that extend from the scratch track.

work by Pouvreau *et al.* [6] also reports results on the cracking sequence of GaAs under wedge indentation. In both cases cracks, equivalent to the median cracks produced by scratching, were observed and it was possible to cleave samples from these experiments. This observation serves to establish the main postulate of this thesis:

Indentation fracture using an indenter of appropriate shape will strongly reduce particles formation in both indentation and cleavage steps and provide a suitable half-penny crack for the cleavage process.

1.3 Methodology

1.3.1 Approach

To prove that indentation fracture is a valuable method to create a precursor crack for GaAs cleavage, we use the following approach:

1. first, we characterise the indentation crack field and cracking sequence of GaAs for various indenter shapes and indentation conditions;
2. once the crack field is known, we attempt to predict the extension of cracks from the indentation load;
3. we also establish the physical mechanisms leading to the nucleation and propagation of these cracks;
4. finally, we conduct tests on commercial opto-electronic component structures to validate the indentation and cleavage procedure derived from the experimental observations.

1.3.2 Methods

The surface crack field is characterised through in-situ instrumented SEM indentation and the sub-surface crack field by cleavage cross-sectioning of indentations. With the help of an in-situ SEM instrumented indentation setup, it is possible to observe the cracking sequence at the surface while recording the

applied load and displacement. This procedure allows a direct correlation of load-displacement histories with cracking events at the surface.

The cross-sectioning technique serves to investigate cracking systems which develop under the surface. It allows also to measure the size of the cracks used for dicing (half-penny crack) and the level of damage below the surface.

The prediction of crack growth from the indentation load is of particular interest in order to determine the optimum parameters for industrial applications. For that purpose, fracture mechanics models using Stress Intensity Factors (SIF) solutions are adapted to the wedge geometry and predictions using the models are compared to experimental results.

At last, understanding the fundamental mechanisms that govern crack nucleation is a necessary step to determine the controlling parameters in such process. In GaAs, it is known that these mechanisms involve nucleation and movement of dislocations. Consequently, Cathodoluminescence (CL) and Transmission Electron Microscopy (TEM) are the appropriate techniques to investigate these mechanisms.

1.3.3 Scope of the Investigation

In every experimental study, it is relevant to define the scope of the investigation, i.e. the range of parameters that will be investigated. The definition of this domain is usually done by preliminary studies and literature review. In the case of indentation fracture of GaAs, numerous parameters are known or are expected to influence the cracking behaviour. Nevertheless, the industrial context of the study restricts the number of these parameters.

As a brief example, temperature, dopant and doping level are known parameters that affect the cracking behaviour of GaAs. However, in the industrial process, dicing operations take place at room temperature and at fixed doping level so that optical properties of the lasers remain stable. Hence, these parameters are not of critical interest in our context, despite their possible interactions with the investigated parameters. The parameters we considered are the indenter geometry (shape and apex angles), the maximum load, the loading rate and the crystallographic orientation of the indented material. In order to test various stress states (plane strain, singularities), three types of indenter are used here:

Wedge indenters: indenters with a 55 μm contact edge and 60°, 90° and 120° apex angle

Conical indenters: indenters with a 60° and 120° apex angle

Pyramidal indenters: Vickers and cube corner

Intuitively, the elongated shape of wedge indenters is expected to promote the creation of median cracks, the size of which should be sufficient for cleavage operations. However, the used wedges have a finite length and end effects are known to occur at their extremities. To limit such effects, we want to investigate different indenter shapes that could be employed to terminate the wedge. This is the aim of the study on conical, Vickers and cube corner indenters. Conical indenters help to reveal effects that can be attributed to the crystal anisotropy

of GaAs. Pyramidal indenters will help determine the influence of shape singularities on the crack field. The reader will be provided with more details about the different indenter geometries in the section on experimental procedures.

1.4 Summary of Results

Main results of the dissertation are as follow:

- The cracking pattern and cracking sequence has been established for wedge indenters. A deep propagating half-penny crack is created under the whole indenter and additional shallow Palmqvist cracks extend at the indenter extremities. Lateral cracks merge with Palmqvist cracks to form chips at the indenter extremities.
- For wedge indenters, the variation of the half-penny crack size and geometry as a function of the indentation load has been established on the basis of weight function modelling.
- The cracking patterns of several point indenters have been compared. The cracking sequence was established for cube corner and conical indenters. Obtuse indenters minimise Palmqvist cracks as well as flakes formation at comparable loads and the threefold symmetry of the cube corner limits the number of chips that are formed.
- The apex angle of the wedge indenter interacts with the slip planes of GaAs. Acute (or sharp) wedge indenters preferentially activate diverging slip systems and promote the nucleation of the half-penny crack, whereas obtuse (or blunt) indenters favour converging slip systems that act as shields for crack initiation;
- Fracture mechanics modelling predicts a dependence of the crack size c with the applied indentation load P . The usual $P \propto c^{3/2}$ relationship, derived from fracture mechanics principles, is experimentally verified.

1.5 Original Contributions

The original contributions of this dissertation include:

- establishment of a detailed map of cracking patterns and cracking sequences as a function of indenter shape and load level for GaAs;
- prediction of crack growth as a function of the indentation load and confrontation to theoretical and semi-empirical models;
- insight in the physical mechanisms responsible for crack initiation in GaAs and experimental evidences of the controlling parameters;
- development or adaptation of unique experimental techniques and demonstration of their advantages and limitations ;
- establishment of a sound basis as well as practical guidelines for the development of indentation fracture with wedge indenters for industrial dicing applications and fracture studies.

1.6 Document Structure

Chapter 2 gives a state of the art on both deformation mechanisms and indentation fracture in III-V semiconductors. Basic concepts on dislocation structures in GaAs are first given. Then, a review on deformation mechanisms under indentation is made. Last, a description of the different crack fields usually found in indentation testing as well as principles of indentation fractures are reviewed.

Chapter 3 is an overview of the different experimental procedures that have been used during this research work. This chapter also includes details on the testing apparatus and the indenter geometries employed.

Chapter 4 deals first with the crack morphologies as well as the cracking sequences encountered under wedge indentation of GaAs. Indentation fracture modelling aspects are discussed for this indenter geometry. Indentation with point indenters is subsequently treated and crack fields, cracking sequence and crack growth prediction are also analysed for this kind of indenters.

Chapter 5 focuses on the crack nucleation mechanisms. The first part of this chapter treats of the wedge indenter and the half-penny crack formation. In the second part, the reader is provided with some explanations on the deformation mechanisms around point indenters and their influence on cracking.

Chapter 6 illustrates how the previous fundamental study found applications to practical cases. Wedge indentation is employed to generate precursor cracks on commercial laser structures. The devices are then separated by the industrial partner on a production system and the quality of cleavage is then controlled.

Bibliography

- [1] K. Wasmer, C. Ballif, C. Pouvreau, D. Schulz, and J. Michler. Dicing of gallium-arsenide high performance laser diodes for industrial applications: Part i: Scratching operation. *J. Mater. Process. Tech.*, 2007.
- [2] K. Wasmer, C. Ballif, C. Pouvreau, D. Schulz, and J. Michler. Dicing of gallium-arsenide high performance laser diodes for industrial applications: Part ii: Cleavage operation. *J. Mater. Process. Tech.*, 2007.
- [3] Wasmer K., C. Ballif, C. Pouvreau, and J.-M. Solletti. Project n° 6025.2 final report. Technical report, CTI, March 2005. CTI internal report.
- [4] K. Wasmer, C. Ballif, R. Gassilloud, C. Pouvreau, R. Rabe, J. Michler, J.-M. Breguet, J.-M. Solletti, A. Karimi, and D. Schulz. Cleavage fracture of brittle semiconductors from the nanometer to the centimeter scale. *Advanced Engineering Materials*, 7:309–317, 2005.
- [5] C. Ballif. Knoop indentation report. Technical report, EMPA, April 2004. EMPA internal report.
- [6] C. Pouvreau, K. Wasmer, J.H. Giovanola, J.-M. Breguet, J. Michler, and A. Karimi. In-situ scanning electron microscope indentation of GaAs. In Springer, editor, *Fracture of Nano and Engineering Materials and Structures*, pages 61–62, 2006.

Chapter 2

State of the Art

Two important subjects are treated in this dissertation: the plastic deformation by nucleation and propagation of dislocations and the initiation and propagation of cracks under indentation. Therefore, this chapter is divided into four sections:

- To start with, the structure and properties of GaAs are introduced;
- the second one deals with aspects linked to the deformation mechanisms under indentations in GaAs;
- the third reviews the crack systems usually found under indentations;
- finally, the last section is a state of the art of fracture mechanics specifically related to indentation fracture.

Nucleation and propagation of dislocations play a crucial role in the process leading to fracture under indentation. The theory of dislocations is complex and an extensive amount of literature is available on the subject. However, it is beyond the scope of this manuscript to give a detailed review of the dislocation structures in semiconductors. We will therefore focus on the main concepts necessary to the understanding of the results and discussion presented in Chapter 5 as well as on aspects concerning more specifically indentation of GaAs. The interested reader will find more details about dislocation theory in the classical books of Hirth [1] and Nabarro [2].

2.1 Structure and Properties of GaAs

The material investigated in this dissertation is single crystal GaAs available in 2" wafer format. Wafers are either 150 or 350 μm thick with one side electrochemically polished. The wafers are doped with silicon at a level of approximately $1 - 2 \times 10^{14}$ atoms/ cm^3 . Figure 2.1 (left) shows an unprocessed wafer that has already been cleaved and a schematic (right) of the wafer with the important crystalline directions.

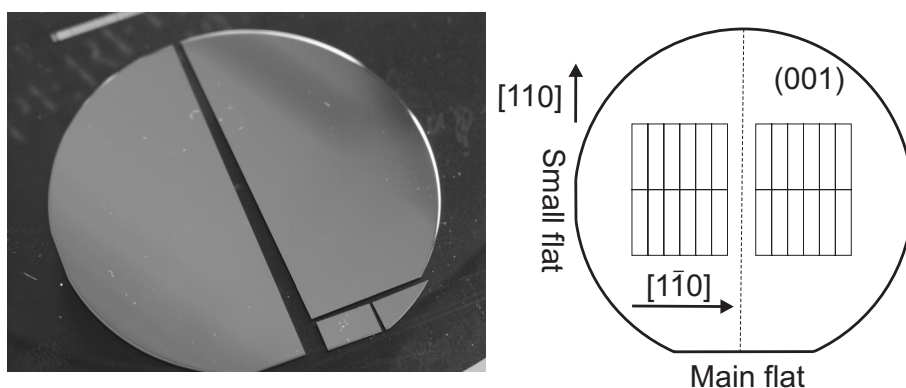


Figure 2.1: Typical wafer and schematic view representing the crystalline directions of interest as well as the orientation of processed laser bars.

The values of Young's modulus, shear modulus and Poisson's ratio are summarised in Table 2.1 for different orientations of the wafer. In this table, moduli

and hardness values obtained from nanoindentation tests with a Berkovich tip are also included.

Face	Isotropic E (GPa)	G (GPa)	H (GPa)	ν
(110) ¹	125	61.4		0.30
(111) ¹	144	43.5		0.30
(100) ¹	89.3	61.4		0.30
(100) ²	111	61.4	7.64	0.30

Table 2.1: Mechanical properties of GaAs.

GaAs is sensitive to the Indentation Size Effect (ISE) commonly observed when testing mechanical properties with nanoindentation techniques. Hence, the apparent Young's modulus drops from a value of about 120 GPa to 110 GPa when the load increases from 10 mN to 200 mN. In the same way, hardness decreases from 8 to 7 GPa. The values indicated in Table 2.1 are mean values through this range.

Figure 2.2 plots the evolution of Young's modulus with the crystallographic directions and illustrates the anisotropy of GaAs.

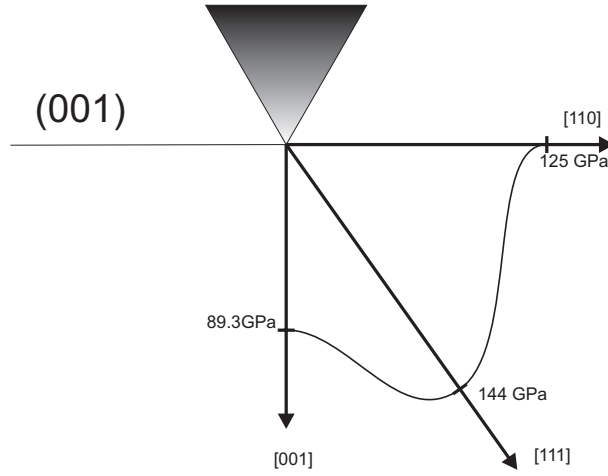


Figure 2.2: Young's modulus evolution with principal crystallographic directions.

Single crystal GaAs has the so-called *zincblende* structure which is similar to the *diamond structure* of silicon. This structure can be described using crystallographic planes and directions. Basically, only a unit cell is necessary to describe the arrangement of atoms and the whole crystal can then be reconstructed by translations and rotations of this unit cell, using the symmetry properties. The unit cell of GaAs is presented in Figure 2.3. It is composed of two Face Centred Cubic (FCC) lattices shifted by $1/4$ of the cube diagonal length along the cube

¹Chen, [3]

²Present study, Berkovich indentation

diagonal. *Ga* atoms (in red in Figure 2.3) are located on the first FCC cell whereas the *As* atoms (in green in the figure) are located on the second one.

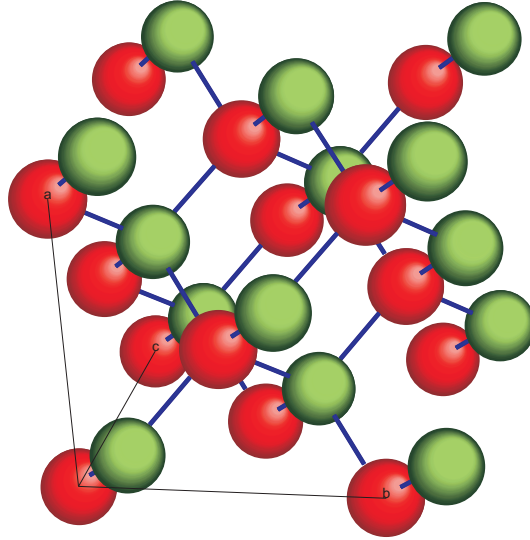


Figure 2.3: Unit cell of GaAs. Red and green spheres represent respectively gallium and arsenic atoms.

A crystalline direction is defined as the normal to a given crystalline plane. This is illustrated in Figure 2.4 where the $[110]$ direction is orthogonal to the (110) plane. Due to the symmetry of the crystal, family of equivalent planes can be defined. A family is a group of planes which have the same properties.

Among others, the $\{110\}$ and the $\{111\}$ families of planes will be frequently referred to in this manuscript. Indeed, the preferential cleavage planes of GaAs belong to the $\{110\}$ family whereas dislocations move preferentially in the $\{111\}$ equivalent planes (see Figure 2.4).

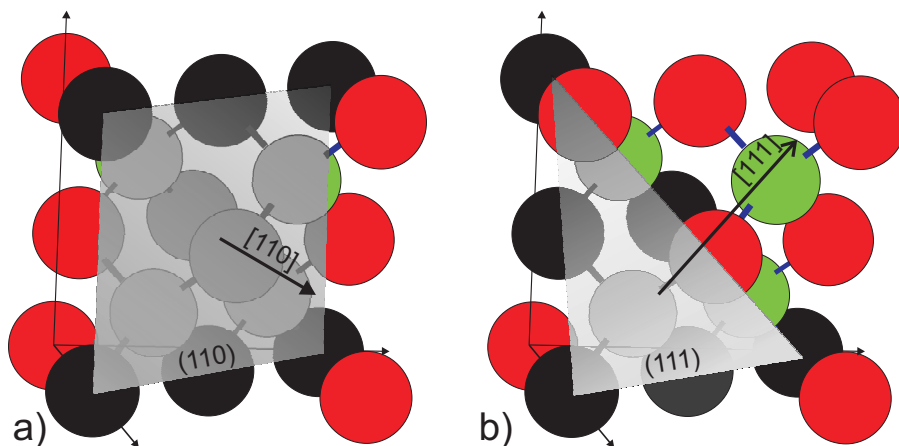


Figure 2.4: Schematic of: a) preferential cleavage plane (110) and b) close packed plane (111)

2.2 Deformation of GaAs under Indentation

2.2.1 Introduction to Dislocations in GaAs

The nucleation and propagation of perfect or partial dislocations and microtwinning are the major mechanisms of plastic deformation in a GaAs crystal. Table 2.2 shows how perfect dislocations (60° or screw in character) usually dissociate in GaAs [1].

Dislocation type	60° dislocation	Screw dislocation
Dissociate into:	Partial 30° Partial 90°	Partial 30° Partial 30°
Microtwins possible	Yes	No

Table 2.2: Possible configurations for the dissociation of perfect dislocations 60° or screw in character (after Hirth and Lothe [1]).

A single loop is composed of different segments that all have the same Burger's vector \vec{b} . Figure 2.5 represents a schematic of a single loop with dislocation segments having either a screw or a 60° character. Screw segments have their Burger's vector colinear with the line vector \vec{u} whereas 60° dislocations have their line vector inclined by 60° to the Burger's vector direction.

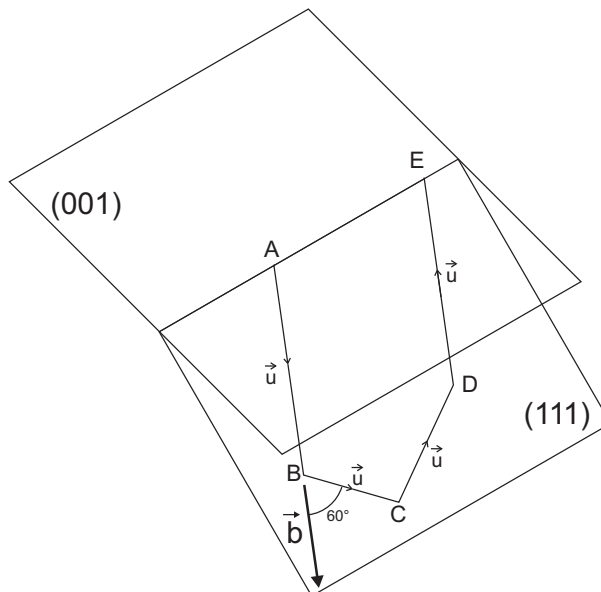


Figure 2.5: Schematic of a dislocation loop in GaAs propagating in a (111) plane with Burger's vector being of $\langle 110 \rangle$ type. \vec{b} represents the Burgers vector. AB and DE represent screw segments of the dislocation (line vector \vec{u} aligned with \vec{b} , BC and CD represent segments of 60° dislocations ($\vec{u} \cdot \vec{b} = 60^\circ$).

Looking more carefully at the stacking sequence of the $\{111\}$ planes shown

in Figure 2.6, we easily see that the double-layered arrangement of the atomic structure makes that the dislocation can belong to:

- the glide set A-a (closely spaced planes);
- the shuffle set a-B (widely spaced planes).

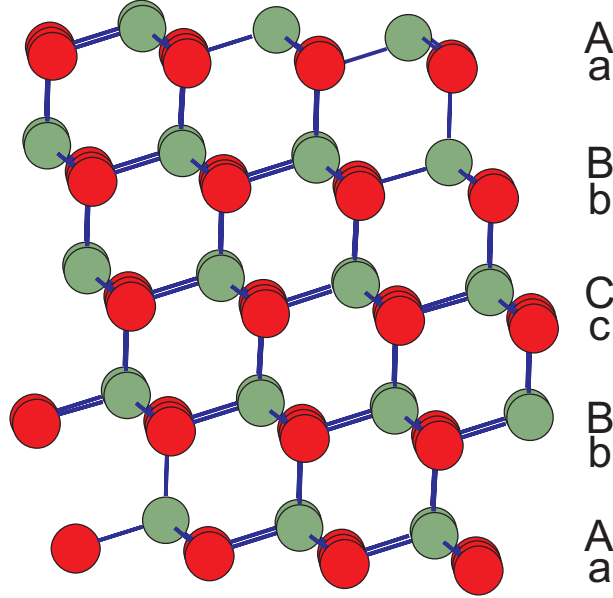


Figure 2.6: Stacking sequence of $\{111\}$ planes in GaAs. Red and green spheres represent respectively gallium and arsenic atoms.

Thus, a 60° perfect dislocation in the glide set with \vec{b} being along $[1\bar{1}0]$ easily dissociate into two Shockley partial dislocations via the reaction [4]:

$$\frac{a}{2}[1\bar{1}0] \rightarrow \frac{a}{6}[1\bar{2}1] + \frac{a}{6}[2\bar{1}\bar{1}] \quad (2.1)$$

These partial dislocations bound a stacking fault, i.e. a default in the stacking sequence (the A-a-B-b-C-c sequence is not respected locally). In the FCC structure, the movement of a wall of partial dislocations leads to the creation of microtwins [1].

The decomposition of perfect dislocations into partial ones takes place preferentially in the glide set configuration [4]. On the contrary, the decomposition of perfect dislocations gliding in the shuffle set is much more difficult and generally takes place at temperatures much higher than Room Temperature (RT).

The extra half-plane of a dislocation can terminate on either a row of *As* or *Ga* atoms. Depending on the atomic species lying at the core of the dislocation, it can be either of the α (*As* atoms) or of the β (*Ga* atoms) type following the Hünfeld convention [5]. As will be seen later in the review, these differences in the composition of the core introduce also significant differences in the mobility of dislocations.

To summarise, the main features in the dislocation structures that are found in GaAs are as follows:

- perfect dislocations, partial dislocations and microtwins are the main mechanisms of deformation in GaAs
- microtwins are most likely observed in the glide set configuration;
- dislocations of α or β types have different mobilities.

This basic knowledge of the dislocation structure in GaAs is necessary for a better understanding of the deformation mechanisms under indentation which is the purpose of the following section.

2.2.2 Deformation Mechanisms under Indentation of GaAs

Under indentation, the high shear stresses combined with the intense confining (hydrostatic) pressure favours the nucleation of abundant dislocation loops moving in $\{111\}$ planes that accommodate the deformation (see [6] for a review on indentation of GaAs).

Different authors [6, 7, 8, 9] reported a sudden displacement (called pop-in event) in the nanoindentation curves of compound semiconductors. This pop-in is usually attributed to the sudden nucleation and propagation of dislocation loops. Leipner *et al.* [7] estimated that the number of nucleated dislocation loops at pop-in during a nanoindentation with a Vickers tip (indenter radius $\sim 1 \mu\text{m}$, penetration $\sim 30 \text{ nm}$) is approximately 1.3×10^6 . The load at which the pop-in occurs is dependent on the doping level and tip bluntness. As an example, Bradby *et al.* [10] reported that it took place at around 25 mN with a spherical tip having a $4.3 \mu\text{m}$ radius whereas Patriarche and Le Bourhis [11] found that it occurs typically below 1 mN with a sharp Berkovich tip. We remark here that the indenter geometry plays a significant role starting with the earliest step of the indentation process.

After their nucleation, dislocation loops arrange in a specific configuration called the *rosette arm* arrangement. A rosette arm is defined by two $\{111\}$ planes forming a V shape and generally aligned with the $\langle 110 \rangle$ directions. When indenting on a $\{001\}$ faces, this arrangement has a fourfold symmetry, i.e. two orthogonal arms cross under the indentation aligned with $\langle 110 \rangle$ directions. For illustration purpose, the reader is referred to the article from Warren *et al.* [5].

When indenting a (001) face with the diagonals of the indenter oriented along $[110]$ or $[\bar{1}10]$, the rosette arms also follow these directions. Observations by either chemical etching [5, 12] or by TEM [13, 14] reveal that either microtwins or perfect dislocations are present depending on the rosette arm. A review on the subject has been made by Le Bourhis *et al.* [6]. Table 2.3 summarises the results obtained for GaAs at room temperature on indented (001) surfaces. The variety of results exposed in this table shows that the formation of microtwins in either the α or β rosette arm is not yet clearly understood.

The asymmetry in the length of the dislocation pattern is not systematically observed [7, 14, 16, 18]. To explain this phenomenon, we remark that most of the experimental results showing the asymmetric behaviour in the rosette arms come from surface observations of dislocation etch pits [5]. Lefebvre *et al.* [14, 20] and Koubaïtai [18] have proposed that perfect dislocations nucleate in the bulk while microtwins form at or close to the indented surface. It becomes therefore obvious that chemical etching will reveal microtwins and not perfect dislocations

Dopant	Indentation load (mN)	Perfect dislocations	Microtwins (M) Stacking Faults (SF)	Reference
Si	300	In one arm (not specified)	SF in other arm	[15]
n type	49	In both arms	M in α arm	[16]
n type	50	In α arm	M in β arm	[14]
In	49-196	In both arms	M in α arm	[17]
undoped	49-196	In both arms	M in α arm	[18]
undoped	0.8-1.7	In both arms	M in one arm (not specified)	[19]

Table 2.3: Summary of dislocation structures around Vickers indentations from Le Bouhris *et al.* [6]. Only the structures at room temperature and in GaAs are reported.

that are nucleated deeper in the bulk thus explaining the asymmetric behaviour of surface observations.

The dopant type, the doping level and the temperature are known to have a non-negligible influence on dislocation structures and might explain some of the differences in observations found in the literature. Nonetheless, the crystallographic orientation seems to play a significant role in the deformation process and, more interestingly, seems also to influence the cracking patterns around the imprint as reported by Warren *et al.* [5]. Indeed, they observed that cracks were present along the β dislocation arm ($[110]$ direction and not in the α arm ($[110]$ direction) and correlated this behaviour to the length of α (longer) and β (shorter) arms. They suggested that the different mobilities of α and β dislocations were responsible for the rosette arm asymmetry and also proposed that dislocation mobility is a major issue in the cracking mechanisms.

Such correlation was confirmed by Fujita *et al.* [12] who indented $\{111\}$ faces of GaAs. They monitored the brittle to ductile transition by measuring the crack lengths induced by Vickers indentations. By varying both temperature and loading rate, they showed that the cracking behaviour of GaAs was controlled by the dislocation mobility and governed by an Arrhenius Kinetic relation.

Bradby *et al.* worked on the spherical indentation of many semiconductors, including silicon, InP and GaAs. Looking at FIB cross-sections of indentations, they reported that cracks nucleate at the pile-up of dislocations under the indentation site [10, 21].

2.2.3 Investigation of Indenter Geometries

In the literature, all experimental investigations concerning wedge indentations were conducted on metals. To our knowledge, no work has been done on the wedge indentation of brittle materials or semiconductors. Thus, Hill [22], Dugdale [23] and Grunzweig *et al.* [24] conducted experiments with wedge-shaped

indenters of various angles. In their work, they showed the significant influence of the indenter angle on the deformation behaviour of metals and particularly on the change of the piling-up behaviour with this angle. For sharp angles (typically less than 60°), the deformation process was best described by the so called slip-line field theory established by Hill [25]. On the contrary, under indenters with large included angles, the plastic zone exhibits an hemispherical symmetry and shows similarities with the elastic/plastic deformation expected to occur around a spherical cavity under internal pressure. In addition, the angle at which the transition between the cutting mode (described by the slip-line field) and the compressive mode (described by the pressurised cavity model) depends on the investigated material. The transition itself is characterised by a change of the degree of material pile-up around the indentation site.

Mulhearn [26], and Atkins [27] conducted similar experiments with cone indenters and also found transitions in the deformation behaviour but at different angles. Although these studies were all conducted on ductile metals (so with no influence of fracture), they are of particular interest for us. Indeed, we will see in Section 5.3.3 that the amount of pile-up also changes with the indenter angle in GaAs.

The work of Morris *et al.* [28] treats the influence of indenter apex angle on brittle fracture. They varied the indenter apex angle of three sided pyramidal indenters from Berkovich (142° total angle) to cube corner one (90° total angle) and investigated the resulting effect on the cracking behaviour of various glass, ceramics and single crystal baryum fluoride. They showed first that increasing acuity of the indenter results in well developed cracking systems. In addition, they found that in most materials cracks stem from indenter corners whereas in single crystal they nucleate preferentially along the faces of the indenter. This result indicates that both the angle and the crystalline structure influences the mechanisms of crack nucleation.

From this brief literature review, we see that the indenter geometry (shape, apex angle) plays a crucial role in the deformation mechanisms that take place during indentation. Also, in GaAs, the nucleation of cracks is intimately related to the dislocation structure found around indentations.

Although some points, like the pop-in effect and the rosette arrangement of dislocations, are widely accepted, the occurrence of microtwinning under indentation is not clearly understood. In addition, effects of the indenter geometry on both deformation and cracking mechanisms have neither been compared nor investigated into details for GaAs and we propose to bridge this gap in this dissertation.

2.3 Nomenclature of Cracking Systems

A very interesting review of cracking systems found under Vickers contacts was made by Cook and Pharr [29]. In this paper, each cracking system is detailed in terms of geometry, development and observations. An extensive list of references is also given for each cracking system. The reader will find here all the required information about indentation of brittle materials, especially in glasses and ceramics.

The cracking behaviour of brittle semiconductors is however significantly

different from the one of glasses and ceramics. For that reason, a different nomenclature is introduced in this manuscript when compared to the one of Cook and Pharr.

2.3.1 Half-Penny Cracks

In the singulation operation, a relatively long and deep crack is needed to separate laser devices properly. In that context, the half-penny crack system is appropriate for dicing applications. For a GaAs wafer with a (001) surface, we define half-penny cracks as cracks that propagate in planes of the $\{110\}$ family which are orthogonal to the (001) face (Figure 2.7). The trace of these cracks at the indented surface follows either the $[\bar{1}\bar{1}0]$ (Figure 2.7 a)) or the $[110]$ direction (Figure 2.7 b)) depending on the orientation of the indenter main edge.

In the case of wedge indentation, half-penny cracks have a well defined semi-elliptical shape and are thus easy to identify. The case of point indenters is more complex as will be seen in Chapter 4. For convenience, and although they have not always a well defined semi-elliptical (or half-penny) shape, cracks propagating in the $\{110\}$ planes orthogonal to the indented surface have been classified into the half-penny category.

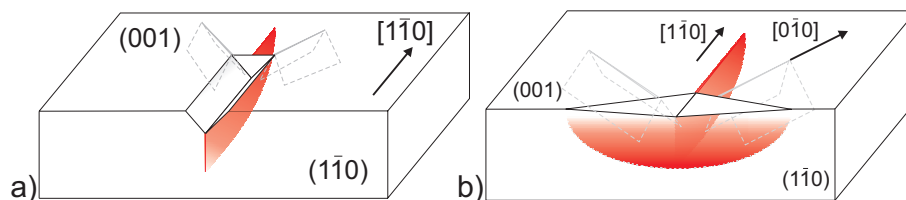


Figure 2.7: Idealised view of a half-penny crack (red) propagating in the (110) plane perpendicular to the (001) indented face in the case of a) a wedge indentation and b) a Vickers indentation. The half-penny cracks are highlighted in red.

2.3.2 Palmqvist Cracks

Usually, Palmqvist cracks are shallow cracks aligned with the edge of the Vickers indenter [31, 32, 33, 34, 35]. In the context of this study, this definition is too restrictive and we define Palmqvist cracks as surface cracks that do not propagate in a **$\{110\}$ plane perpendicular** to the indented face. The schematic view in Figure 2.8 illustrates this condition for two types of indenters. In the case of a wedge indentation, Palmqvist cracks can be either perpendicular or make an angle with the indented surface. In the case of point indenters, these cracks follow mainly $\langle 100 \rangle$ directions and propagate in $\{110\}$ planes making a 45° angle with the surface.

Lankford [32] first proposed a model relating the Palmqvist crack size with the indentation load to the power $2/3$ but conflicting results exist in the literature where various semi-empirical models have been proposed to fit experimental data [33, 34]. However, it has been shown [35] that the solutions used to model half-penny or Palmqvist cracks propagation give similar results when the

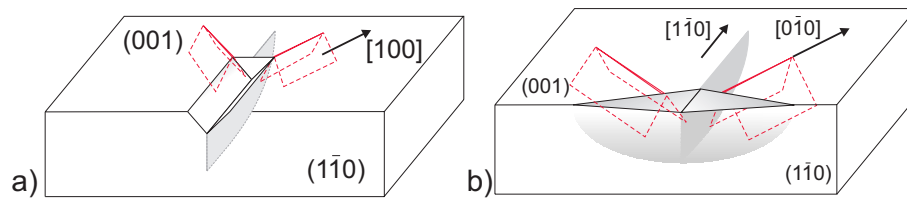


Figure 2.8: Idealised view of the Palmqvist crack system under a) wedge and b) Vickers indentations. The Palmqvist cracks are highlighted in red.

crack size becomes sufficiently large when compared to the size of the residual impression.

Fujita *et al.* [12] and Maeda *et al.* [30], reported that, depending on the experimental conditions (load and temperature), either Palmqvist or Half-penny cracks are observed under Vickers indentation.

2.3.3 Lateral and Shallow Lateral Cracks

Two types of subsurface cracks are described in the literature. The lateral crack system, nucleates at sharp indenter contacts. This system was first described by Lawn and Swain in a paper about Knoop indentation of glasses [36] and was analysed later in a paper by Marshall *et al.* [37]. Lateral cracks nucleate at the boundary of the inelastically deformed area beneath the indentation and run nearly parallel to the surface as illustrated in Figure 2.9 a). In the shallow lateral crack system, described in Figure 2.9 b), cracks nucleate at the contact edges and propagate close to the surface frequently bounded by Palmqvist cracks [29, 38].

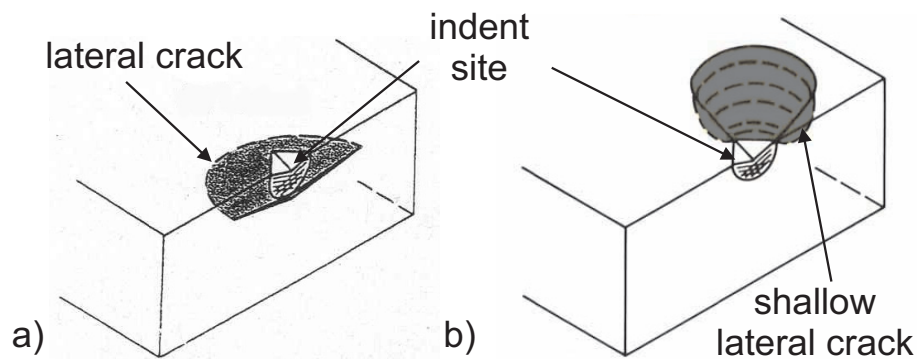


Figure 2.9: Idealised view of a) the lateral and b) the shallow lateral crack systems developing under Vickers indentations (After Cook and Pharr [29]).

In our study, the term of lateral cracks is used for subsurface cracks independently of whether they run nearly parallel to the surface or not. In particular, under wedge indentations, these lateral cracks often follow a V-shape arrangement. The extension of lateral and shallow lateral cracks must be prevented since the merging of these cracks produces flakes and undesirable material removal in the dicing process.

2.4 Indentation Fracture Mechanics

The indentation fracture method was introduced during the 70's to evaluate the resistance of brittle materials to contact damage with the help of spherical or sharp indenters. Particular interest was placed at that time on describing the cracking sequence as a function of the loading sequence and also to predict the evolution of the crack size with the applied indentation load. Early studies were conducted with spherical indenters [39, 40] following the pioneering work of Hertz on the contact of solids [41]. The progressive introduction of sharp indenters (Knoop, Vickers), initially employed for hardness determination, imposes an adaptation of the models to the different crack systems that develop under such indenters [42, 43].

The main goals of such models are to obtain predictions of crack growth with the applied indentation load and the determination of the resistance to fracture for brittle materials.

2.4.1 Elements of Fracture Mechanics

Since the 1920's, and work of Griffith [44], it is well known that cracks are a controlling parameters in the prediction of the lifetime of structural components. In the field of fracture mechanics, Linear Elastic Fracture Mechanics (LEFM) addresses the problems linked to the initiation and propagation of cracks in brittle solids, i.e. solids behaving quasi elastically up to failure. In such problems, we have to answer basically two questions:

1. when does the crack start to propagate? (the problem of crack initiation)
2. how does the crack propagate? (the problem of the propagation stability)

In LEFM, two major concepts have been developed to answer these questions: the Stress Intensity Factor (SIF or K) based on the description of the stress field at the crack tip and the Energy Release Rate (ERR or G) based on a global energy balance.

Three basic loading modes exist for cracks that are called mode I (opening mode), II (in-plane shearing mode) and III (out-of-plane shearing mode) [45]. A SIF defined as K_I , K_{II} and K_{III} corresponds to each mode. The SIF at the crack tip is expressed as a function of the remote stress σ and the crack size c according to:

$$K = \phi \sigma \sqrt{c} \quad (2.2)$$

where ϕ is a dimensionless function representative of the loading geometry and boundary conditions.

In the following lines we concentrate on the opening mode: mode I. Although exact expressions of the SIF can be derived for some simple loading configurations, closed form solutions are not always available. In such cases, the SIF can be obtained by numerical methods [46, 47, 48].

For a given crack subjected to given loading conditions, once the expression of the SIF is determined, we are able to compute the numerical value of the SIF at the crack tip. As the SIF at the crack tip reaches a critical value, known as the fracture toughness of the material and defined as K_{Ic} for mode I, the crack starts to propagate. The fracture toughness K_{Ic} is assumed to be an intrinsic property of the material which is determined through standard

testing procedures¹. We insist on the fact that the SIF is a numerical value that is derived from analytical expressions or numerical calculations and that the fracture toughness is a property of the material that determines its ability to resist the propagation of a crack.

The Energy Release Rate (ERR or G) approach is based on a global energy balance. The potential energy of a cracked body with a crack subjected to a load can be written:

$$\Pi = -W + U_E \quad (2.3)$$

where Π is the potential energy of the system, W is the potential energy of load and U_E is the elastic strain energy.

The equilibrium condition between the potential energy Π and the energy of surface creation U_s is achieved when:

$$\frac{d(\Pi + U_s)}{da} = 0 \quad (2.4)$$

G is defined as the variation in the potential energy of the cracked body ($\partial\Pi$) for a small extension of crack growth (da) according to:

$$G = -\frac{\partial\Pi}{\partial a} \quad (2.5)$$

where ∂a represents a small extension of the crack front.

If we consider a cracked body subjected to a load, the expression for G allows us to determine a necessary condition for crack growth when:

$$G = 2\gamma_s \quad (2.6)$$

where γ_s is the specific surface energy of a newly created crack given in J/m^2 . The ERR at this instance is also called the critical ERR and referred as G_c ². A sufficient condition for the stability of crack growth is:

$$\frac{\partial G}{\partial a} < 0 \rightarrow \text{stable crack propagation} \quad (2.7a)$$

$$\frac{\partial G}{\partial a} > 0 \rightarrow \text{unstable crack propagation} \quad (2.7b)$$

G can be interpreted in terms of the load-displacement curve as illustrated in Figure 2.10 and briefly discussed below³. The principle of the energetic analysis of load-displacement curves (also called the compliance method) is important since similar analysis is used for the determination of the cleavage energy of GaAs from indentation load-displacement curves as presented in Section 4.2.2.1.

In order to derive G from the compliance method, we have to consider the load-displacement curves of two consecutive crack lengths on a specimen subjected to a given loading (see Figure 2.10 for details). Figure 2.10 presents such graphical analysis in two different loading configurations: a) constant load and b) fixed grip (constant displacement) applied.

¹example: ASTM E399-90, Standard Test Method for Plane Strain Fracture Toughness of Metallic Materials.

² G_c becomes G_{Ic} in the specific case of pure mode I loading

³More details can be found about this analysis in the books of Anderson [45] or Lawn [49]

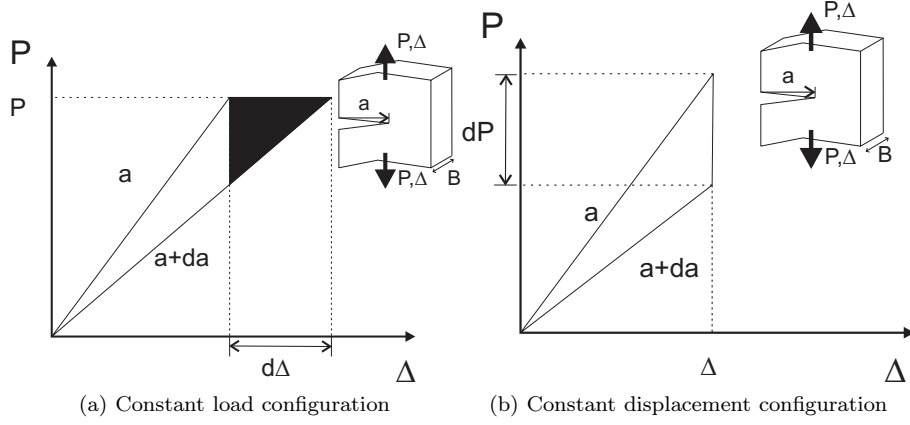


Figure 2.10: Energetic analysis using the compliance method for two different loading configurations: a) fixed load and b) fixed grip.

From the precedent argument, one can also show that G can be expressed in terms of the system compliance C , both for fixed load and grip conditions. The compliance C is given by the relation:

$$C = \frac{P}{\Delta} \quad (2.8)$$

where P is the applied load and Δ the displacement.

In the constant load case G is determined according to [45]:

$$G = \frac{P^2}{2B} \left(\frac{dC}{da} \right) \quad (2.9)$$

where B is the width of the cracked body. In the constant displacement case G is determined according to [45]:

$$G = -\frac{\Delta^2}{2B} \left(\frac{d(C^{-1})}{da} \right) \quad (2.10)$$

In the presented case, the crack propagation is stable under fixed grip conditions ($\frac{\partial G}{\partial a} < 0$) and unstable when constant load conditions are achieved ($\frac{\partial G}{\partial a} > 0$).

The two concepts of SIF and ERR are equivalent [45]. This equivalence can be established assuming fixed grip conditions and calculating the work done by the crack face stresses when they are released during a small increment of crack growth. The integration of the crack face stresses and displacement yields the relationship:

$$G_{Ic} = \frac{K_{Ic}^2}{E'} \quad (2.11)$$

where G_{Ic} is the critical energy release rate for mode I and E' is the effective Young's modulus which depends on whether plane strain or plane stress conditions are achieved in the experiment.

2.4.2 Application to Indentation Fracture

The treatment of indentation problems based on conventional fracture mechanics tools has some restrictions. Firstly, due to the complexity of the stress field under indentation, it is not accurate to speak about pure mode I (or also mode II or mode III) loading for indentation fracture problems. For that reason, the term K_c defined as the indentation fracture toughness replaces the conventional fracture toughness K_{Ic} hereafter.

Secondly, in the modelling of indentation fracture experiments, the complex question of crack nucleation (i.e. the creation of the crack) is separated from the ensuing crack propagation. In the indentation process, the initiation of the crack refers to the nucleation or creation of the crack rather than to the moment where an existing crack starts to propagate (as in conventional fracture mechanics). So, while the nucleation step is important in determining the threshold to fracture as a function of different parameters, the models used here pertain only to the propagation of well developed crack systems.

As previously stated, two approaches of indentation fracture problems are essentially found in the literature. In the semi-empirical analysis, the crack is assumed to have a semi-circular geometry. The crack configuration is thus simplified into the Center Loaded Half-Penny Crack (see Figure 2.11 a)) and the analytical solution gives the indentation fracture toughness K_c according to [50]:

$$K_c = \chi \frac{P}{c^{3/2}} \quad (2.12)$$

where P is the indentation load, c is the size of the crack trace at the surface and χ an adimensional function. Contrary to ϕ , which is representative of the loading geometry and crack shape, in Equation 2.2, χ is a function that depends on materials properties (E,H) and indenter geometry. For a given indenter geometry, χ is usually determined by experimental calibration. Once the expression of χ is determined, it is possible to compute a value of K_c from experimental data of indentation load and crack size.

Despite the limiting assumptions that restrict severely the field of application of such models, this kind of modelling is widely found in the literature. Some of the most used indentation fracture models have been developed by Lawn *et al.* [51, 52], Antsis *et al.* [50, 53] for median/half-penny crack systems, or Lankford [32], Niihara *et al.* [33, 34], and Laugier [35] for Palmqvist crack systems. Among these models, we will give a particular attention to the model developed by Antsis *et al.* [50]. The main reasons to focus on this particular model are that it has been successfully tested over a wide range of materials and it is dedicated to the median/half-penny geometry.

The second approach is based on the development of weight functions. The weight functions are widely employed in fracture mechanics to obtain the SIF for various loading conditions or crack geometries [46, 54]. As an example, such solutions have been used for semi-elliptical cracks subjected to tension or bending [47, 48]. In this approach, the expression of the SIF is determined with the help of adimensional functions (weight functions) that are derived exclusively from the crack geometry and loading configuration.

The weight function approach has found only a limited audience in the field of indentation fracture mechanics. To our knowledge, only Fett and Rizzi [55, 56] have considered this approach to solve sharp indentation contact problems.

However, the analysis developed in these articles concentrates on theoretical developments and only few experimental validating results are found. In this dissertation, we propose to apply this approach to the case of wedge indentation. The weight function developed by Fett [54] for a Center Loaded Half-Penny Crack (also called CLHPC in the manuscript), and initially dedicated to point indenters, is interesting as a first approximation of the wedge indentation case.

In the CLHPC configuration, a point force F_T acts on the crack faces at the centre of the crack [54, 57] as illustrated in Figure 2.11 a). In this drawing P is the indentation load and F_T the load acting upon the crack edge. The geometric description of the half-penny crack is given in Figure 2.11 b). In this figure, the crack front is defined in polar coordinates by the angle φ and the radius r (which varies with φ). The crack size is in turn defined by its length $2c$ and its depth a .

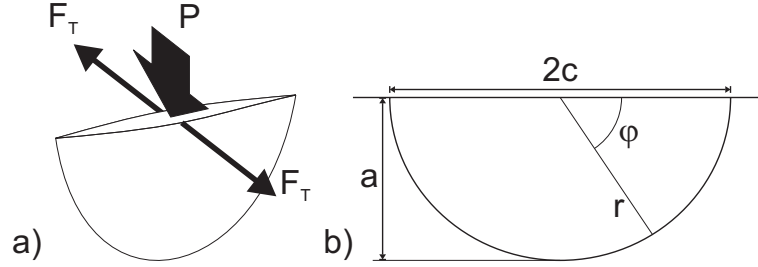


Figure 2.11: Sketch of the the Center Loaded Half-Penny Crack configuration (CLHPC) a) the loading configuration, b) the geometric description of the half-penny crack.

In such case, the SIF K_P has been numerically obtained by Fett *et al.* [54] and is given according to :

$$K_P = \frac{(1.13 - 0.09 \left(\frac{a}{c}\right))P}{2c\sqrt{\pi a}E(k)} [1 + 0.1(1 - \sin^2(\varphi))] \left[\left(\frac{a}{c}\right)^2 \cos^2(\varphi) + \sin^2(\varphi) \right]^{1/4} \quad (2.13)$$

with $E(k)$, the elliptical integral of second kind :

$$E(k) = \int_0^{\pi/2} \sqrt{1 - k^2 \sin^2(\varphi)} d\varphi \quad (2.14)$$

and k :

$$k = \sqrt{1 - \left(\frac{a}{c}\right)^2} \quad (2.15)$$

The weight function F_φ is given as:

$$F_\varphi = [1 + 0.1(1 - \sin^2(\varphi))] \left[\left(\frac{a}{c}\right)^2 \cos^2(\varphi) + \sin^2(\varphi) \right]^{1/4} \quad (2.16)$$

In this case, the SIF at the surface (K_{surf}) and at the deepest point (K_{depth}) are written [54]:

$$K_{surf} = (1.13 - 0.09 \left(\frac{a}{c}\right)) 1.1 \frac{F_T}{2c^{3/2}\sqrt{\pi}E(k)} \quad (2.17a)$$

$$K_{depth} = (1.13 - 0.09 \left(\frac{a}{c}\right)) \frac{F_T}{2c\sqrt{\pi a}E(k)} \quad (2.17b)$$

with F_T being equal to:

$$F_T = \frac{P \cot(\psi)}{2} \quad (2.18)$$

where P , is the indentation load, and ψ the half angle of the wedge indenter.

The weight function approach predicts the same dependency of the crack size on the indentation load ($P \propto c^{3/2}$). However, in our opinion, it has the advantage over semi-empirical models to give a complete description of the SIF along the crack front. The main interest for dicing applications is that both the length and the depth of the crack can be predicted.

2.4.3 Special Applications to Fracture of GaAs

Fracture toughness of GaAs was estimated by several methods and for various orientations [3, 58, 59, 60]. Table 2.4 compares the obtained results.

Method	Fracture plane	K_C (MPa \sqrt{m})	Reference
IBF ⁴	(110)	0.31 \pm 0.03	[3]
IBF ¹	(111)	0.45 \pm 0.03	[3]
IBF ¹	(100)	0.43 \pm 0.03	[3]
DCB ⁵	(110)	0.44 \pm 0.04	[58]
IBF ⁶	(110)	0.46 \pm 0.02	[59]
IBF ³	($\bar{1}$ 10)	0.46 \pm 0.02	[59]
IBF ³	(110)	0.43 \pm 0.04	[60]
IBF ⁷	(110)	0.49 \pm 0.03	[60]
ASTM E-399	(110)	0.49 \pm 0.03	[60]
Vickers Indentation	(110)	0.53	[60]
Vickers Indentation	($\bar{1}$ 10)	0.98	[60]

Table 2.4: Summary of fracture toughness values reported by several authors.

In most studies, the computed fracture toughness values of GaAs are comprised between 0.43 and 0.49 MPa \sqrt{m} and this range is independent of the measurement method, except in two cases.

¹IBF: Indentation Beam Fracture, $K_c = \sigma_f \frac{M_b}{Q^{1/2}} (\pi a)^{1/2}$

²DCB: Double Cantilever Beam

³IBF: Indentation Beam Fracture, $K_c = \sigma_f \frac{M_b}{Q^{1/2}} a^{1/2}$

⁴Same technique as in ³ but $K_c = \eta \left(\frac{E}{H_V}\right)^{1/8} (\sigma_f P_i^{1/3})^{1/4}$

The first exception is found in the work of Chen and Morrissey [3] which underestimates the fracture toughness ($0.31 \text{ MPa}\sqrt{m}$). A difference in the formula they used to compute fracture toughness might be at the origin of these different values. The second exception is found in the work of Margevicius and Gumbsch [60] with the direct measurement of crack stemming from Vickers indentations. This latter work highlights also the huge difference between values obtained for (110) and ($\bar{1}\bar{1}0$) planes (nearly a ratio 1 to 2) characteristic of an asymmetric cracking behaviour.

2.4.4 Semiconductor Dicing

Despite its widespread application in the industry and also in laboratories, few studies exist about the scribe and break technique [61, 62, 63]. Misra and Finnie [64] investigated the particles formation as well as the formation of median vents when scratching silicon and presented recommendations to optimise the dicing process using the scribe and break technique.

Sauthoff *et al.* [65] investigated the effect of the speed at which a cleavage crack propagates on the aspect of cleaved surfaces in GaAs. Using fractographic analysis at different scales, they demonstrated that the quality of cleaved surfaces is strongly related to the velocity at which the crack travels. In particular, they showed that when the crack speed reaches a certain level, dynamic propagation instabilities appear that deteriorate the quality of cleaved surfaces.

More recently Wasmer *et al.* [66, 67, 68] investigated the whole dicing process of GaAs wafers. In particular, they showed that when the median vent produced by scratching is too small, catastrophic failure of the sample occurs. On the contrary, when the median crack reaches a critical depth, the fracture can be controlled and the quality of cleaved surfaces is greatly improved confirming the results of Sauthoff *et al.* [65].

Most of these contributions that have been published in the field of semiconductor dicing concentrates either on the optimisation of scratching parameters or on the development of laser techniques [69, 70] in order to minimise particles generation.

2.5 Summary

In this literature review, we have seen that conflicting observations exist about the occurrence of microtwinning in either the [110] or the [$\bar{1}\bar{1}0$] direction. We have also seen that no studies have been conducted on the influence of the indenter geometry on the deformation mechanisms in GaAs. The comparison of the indentation crack field obtained with different indenter geometries has, to our knowledge, never been done. The literature review has shown that the indentation process has never been employed as a way to produce a precursor crack for dicing. This lack of information is one motivation for the work we propose to do in this dissertation.

In Chapter 4, we propose to establish a detailed map of cracking as a function of the indenter geometry (shape and apex angle) in GaAs. We will show that the CLHPC configuration usually employed for Vickers indentations can also be extended to predict the evolution of the crack size under wedge indentations.

We will also see that the weight function approach yields a good estimate of the fracture toughness of $\{110\}$ planes in GaAs.

In Chapter 5, we propose to examine the interaction between the indenter geometry, the deformation mechanisms and the cracking behaviour of GaAs. We will especially look at the influence of the indenter angle on the nature and arrangement of dislocations around indentations.

In Chapter 6, we will demonstrate that the indentation with a wedge indenter is an appropriate method to create precursor cracks for GaAs dicing. Advantages and drawbacks of the indentation process will be demonstrated.

Bibliography

- [1] J. P. Hirth and J. Lothe. *Theory of dislocations*. Wiley-Interscience publication. John Wiley & Sons, 2nd edition, 1982.
- [2] F. R. N. Nabarro. *Dislocations in Solids*. Elsevier, 2nd edition, 1979.
- [3] C. P. Chen and C. J. Morrissey. Evaluation of GaAs fracture mechanics. *Nasa Tech Brief*, 11(1):1–63, 1987.
- [4] E.A. Stach, T. Freeman, A.M. Minor, D.K Owen, J. Cumings, M.A. Wall, T. Chraska, R. Hull, Jr Morris, J.W., A. Zetl, and U. Dahmen. Development of a nanoindenter for in-situ transmission microscopy. *Microscopy and Microanalysis*, 7:507–517, 2001.
- [5] P.D Warren, P. Pirouz, and S.G. Roberts. Simultaneous observation of α and β -dislocation movement and their effect on the fracture behaviour of GaAs. *Philosophical Magazine A*, 50(5):23–28, 1984.
- [6] E. Le Bourhis and Patriarche G. Plastic deformation of III-V semiconductors under concentrated load. *Progress in Crystal Growth and Characterization of Materials*, pages 1–43, 2003.
- [7] H. S. Leipner, L. Lorenz, A. Zecker, H. Lei, and P. Grau. Nanoindentation pop-in effect in semiconductors. *Physica B*, 308-310:446–449, 2001.
- [8] J.E. Bradby, J.S. Williams, J. Wong Leung, S.O. Kucheyev, M.V. Swain, and P. Munroe. Spherical indentation of compound semiconductors. *Philosophical Magazine A*, 82(10):1931–1939, 2002.
- [9] J.E. Bradby, J.S. Williams, and M.V. Swain. Pop-in events induced by spherical indentation in compound semiconductors. *Journal of Materials Research*, 19(1):380–386, 2004.
- [10] J.E. Bradby, J.S. Williams, J. Wong Leung, M.V Swain, and P. Munroe. Mechanical deformation of InP and GaAs by spherical indentation. *Applied Physics Letter*, 78(21):3235–3237, 2001.
- [11] G. Patriarche and E Le Bourhis. Low load deformation of InP under contact loading; comparison with GaAs. *Philosophical Magazine A*, 82(10):1953–1961, 2002.
- [12] S. Fujita, K. Maeda, and S. Hyodo. Dislocation mobility-controlled cracking in GaAs caused by constant-rate indentation. *Philosophical Magazine A*, 65(1):131–147, 1992.
- [13] E. Le Bourhis and G. Patriarche. Deformations induced by a Vickers indenter in InP at room temperature. *Eur. Phys. J.*, 12:31–36, 2000.
- [14] A. Lefebvre, Y. Androussi, and G. Vanderschaeve. A TEM investigation of the dislocation rosettes around a Vickers indentation in GaAs. *Phys. Stat. Sol. A*, 99:405, 1987.
- [15] H. R. Höche and J. Schreiber. Anisotropic deformation behavior of GaAs. *Physica Status Solidi A: Applied Research*, 86(1):229–236, 1984.

- [16] C. Levade and G. Vanderschaeve. Rosette microstructure in indented (001) GaAs single crystal and the α/β symmetry. *Phys. Stat. Sol. A*, 171:83–88, 1999.
- [17] S. Koubaïti, C. Levade, J.J. Couderc, and G. Vanderschaeve. On the influence of indium addition on the mechanical properties of GaAs at room temperature. *European Physical Journal: Applied Physics C*, 1:141–146, 1998.
- [18] S. Koubaïti, C. Levade, and G. Vanderschaeve. Vickers indentation on the {001} GaAs under illumination and in darkness. *Philosophical Magazine A*, 80:83–104, 2000.
- [19] E. Le Bourhis and Patriarche G. Transmission electron microscopy observations of low-load indents in GaAs. *Philosophical Magazine Letters*, 79(10):805–812, 1999.
- [20] A. Lefebvre and G. Vanderschaeve. The origin of microtwinning in room temperature indented undoped and n-doped GaAs. *Phys. Stat. Sol. A*, 107:647–653, 1988.
- [21] J.E. Bradby, J.S. Williams, J. Wong Leung, M.V Swain, and P. Munroe. Transmission electron microscopy observation of deformation microstructure under spherical indentation. *Applied Physics Letter*, 77(23):3749–3751, 2000.
- [22] R. Hill. On the mechanics of cutting metal strips with knife-edged tools. *J. Mech. Phys. Solids*, 1(3):265–270, 1953.
- [23] D.S. Dugdale. Wedge indentation experiments with cold worked metals. *Journal of the Mechanics and Physics of Solids*, 2:14–26, 1953.
- [24] J. Grunzweig, I. M. Longman, and J. Petch. Calculations and measurements on wedge-indentation. *Journal of the Mechanics and Physics of Solids*, 2:81–86, 1954.
- [25] R. Hill. *The mathematical theory of plasticity*. Oxford engineering science series. Oxford university press, London, 1st edition, 1950.
- [26] T.O Mulhearn. The deformation of metals by Vickers type pyramidal indenters. *J. Mech. Phys. Solids*, 7(2):85–96, 1959.
- [27] A.G Atkins and D. Tabor. Plastic indentation in metals with cones. *J. Mech. Phys. Solids*, 13(3):149–164, 1965.
- [28] D. J. Morris, S. B. Myers, and R.F. Cook. Sharp probes of varying acuity: instrumented indentation and fracture behavior. *Journal of Materials Research*, 19(1):165–175, 2004.
- [29] R. F. Cook and G. M. Pharr. Direct observation and analysis of indentation cracking in glasses and ceramics. *J. Am. Ceram. Soc.*, 73(4):787–817, 1990.
- [30] K. Maeda, H. Nishioka, N. Narita, and S. Fujita. Brittle-to-ductile transition studied by constant-rate indentation cracking. *Materials Science and Engineering*, A176:121–126, 1994.

- [31] S. Palmqvist. A method to determine the toughness of brittle materials, especially hard metals. *Jernkontorets Ann.*, 141:303–307, 1957.
- [32] J. Lankford. Thresold microfracture during elastic-plastic indentation of ceramics. *Journal of Materials Science*, 16:1177–1182, 1981.
- [33] K. Niihara, R. Morena, and D. P. H. Hasselman. Evaluation of K_{IC} of brittle solids by the indentation method with low crack-to-indent ratios. *Journal of Materials Science Letters*, 1(13), 1982.
- [34] K. Niihara. A fracture mechanics analysis of indentation-induced Palmqvist cracks in ceramics. *Journal of Materials Science Letters*, 2(5), 1983.
- [35] M.T. Laugier. New formula for indentation toughness in ceramics. *Journal of Materials Science Letters*, 6:355–356, 1987.
- [36] B. R. Lawn and M. V. Swain. Microfracture beneath point indentations in brittle solids. *Journal of Materials Science*, 10(1):113–122, 1975.
- [37] D.B. Marshall, B.R. Lawn, and A.G. Evans. Elastic/plastic indentation damage in ceramics: The laterals cracks system. *J. Americ. Ceram. Soc.*, 65:561, 1982.
- [38] A.G. Evans and T.R. Wilshaw. Quasi-static solid particle damage in brittle solids. *Acta Materiala*, 24:939–956, 1976.
- [39] F.C. Frank and B.R. Lawn. On the theory of Hertzian fracture. *Proceedings of the Royal Society of London: Series A, Mathematics*, 299:291, 1967.
- [40] B. R. Lawn. Hertzian fracture in single crystals with the diamond structure. *Journal of Applied Physics*, 39:4828, 1968.
- [41] H. Hertz. On the contact of elastic solids. *Zeitschrift für die Reine und Angewandte Mathematik*, 92:156–171, 1881.
- [42] B. R. Lawn, M. V. Swain, and K. Phillips. Mode of chipping fracture in brittle solids. *Journal of Materials Science*, 10(7):1236–1239, 1975.
- [43] B. R. Lawn and R. Wilshaw. Indentation fracture: principles and applications. *Journal of Materials Science*, 10:1049–1081, 1975.
- [44] A. A. Griffith. The phenomena of rupture and flow in solids. *Philosophical Transactions of the Royal Society of London, Series A.*, 221:163–198, 1921.
- [45] T.L. Anderson. *Fracture Mechanics*. CRC Press, third edition, 2005.
- [46] H. Tada, P. C. Paris, and G. R. Irwin. *The Stress Analysis of Cracks Handbook*. American Society of Mechanical Engineers, third edition, 2000.
- [47] I.S. Raju and J.C. Jr Newman. Stress intensity factors for a wide range of semi-elliptical surface cracks in finite thickness plates. *Engineering Fracture Mechanics*, 11:817–829, 1979.
- [48] J.C. Jr Newman and I.S. Raju. An empirical stress intensity factor equation for the surface crack. *Engineering Fracture Mechanics*, 15(1-2):185–192, 1981.

- [49] B.R. Lawn. *Fracture of brittle solids*. Solid state science series. Cambridge university press, 2nd edition, 1997.
- [50] G.R Antsis, P. Chantikul, B.R. Lawn, and D. B. Marshall. A critical evaluation of indentation techniques for measuring fracture toughness: I, direct crack length measurements. *Jour. Amer. Ceram. Soc.*, 64(9):533–538, 1981.
- [51] B. R. Lawn and D. B. Marshall. Hardness, toughness, and brittleness - indentation analysis. *Journal of the American Ceramic Society*, 62(7-8):347–350, 1979.
- [52] B.R. Lawn, A.G. Evans, and D.B. Marshall. Elastic/plastic indentation damage in ceramics: the median/radial crack system. *Jour. Amer. Ceram. Soc.*, 63(9-10):574–581, 1980.
- [53] P. Chantikul, G. R. Anstis, B.R. Lawn, and D. B. Marshall. A critical evaluation of indentation techniques for measuring fracture toughness: Ii, strength method. *Journal of the American Ceramic Society*, 64(9):539–543, 1981.
- [54] T. Fett and D. Munz. *Stress Intensity Factors and Weight Functions*. Advances in Fracture series. Southampton UK, 1997.
- [55] T. Fett, G. Rizzi, and E. Diegele. Weight functions for cone cracks. *Engineering Fracture Mechanics*, 71:2551–2560, 2004.
- [56] T. Fett, A. B. Kouna Njiwa, and J. Radel. Crack opening displacements of Vickers indentation cracks. *Engineering Fracture Mechanics*, 72:647–659, 2005.
- [57] T. Fett and G. Rizzi. *Problems in fracture mechanics of indentation cracks*. Forschungszentrum Karlsruhe, 2003.
- [58] G. Michot and A. and George. Fracture toughness of pure and In doped GaAs. *Scripta Metallurgica*, 22:1043–1048, 1988.
- [59] K. Yasutake, Y. Konishi, K. Adachi, K. Yosh, M. Umeno, and H. Kawabe. Fracture of GaAs wafers. *Japanese Journal of Applied Physics*, 27:2238, 1988.
- [60] R. W. Margevicius and P. Gumbsch. Influence of crack propagation direction on {110} fracture toughness of gallium arsenide. *Philosophical Magazine A*, 78:567–581, 1998.
- [61] D. Scannell and D. Smith. Scribing compound semiconductors: An application primer. Technical report, Karl Suss, November 1987.
- [62] J. W. Ure. Application of scribing to optoelectronic devices. Technical report, Karl Suss Report, May 1988.
- [63] Loomis Inc. *A Fresh Perspective on Scribing and Breaking Applied to Semiconductor Wafer Processing*, February 2006. available at www.loomisinc.com.

- [64] A. Misra and I. Finnie. On the scribing and subsequent fracturing of silicon semiconductor wafers. *Journal of Materials Science*, 14(11):2567–2574, 1979.
- [65] K. Sauthoff, M. Wenderoth, A.J. Heinrich, M.A. Rosentreter, K.J. Engel, T.C.G. Reusch, and R.G. Ulbrich. Non linear dynamic instability in brittle fracture of GaAs. *Physical Review B*, 60(7):4789–4795, 1999.
- [66] K. Wasmer, C. Ballif, R. Gassilloud, C. Pouvreau, R. Rabe, J. Michler, J.-M. Breguet, J.-M. Solletti, A. Karimi, and D. Schulz. Cleavage fracture of brittle semiconductors from the nanometer to the centimeter scale. *Advanced Engineering Materials*, 7:309–317, 2005.
- [67] K. Wasmer, C. Ballif, C. Pouvreau, D. Schulz, and J. Michler. Dicing of gallium-arsenide high performance laser diodes for industrial applications: Part i: Scratching operation. *J. Mater. Process. Tech.*, 2007.
- [68] K. Wasmer, C. Ballif, C. Pouvreau, D. Schulz, and J. Michler. Dicing of gallium-arsenide high performance laser diodes for industrial applications: Part ii: Cleavage operation. *J. Mater. Process. Tech.*, 2007.
- [69] Laetitia Mayor. Dicing of GaAs wafers -security and yield issues: What dicing technologies have to offer? *Future Fab Intl.*, 15:21, 2003.
- [70] N. Dushkina. Safely dicing GaAs wafers with lasers. *Technical Papers of ISA*, 438:175–183, 2003.

Chapter 3

Experimental Procedures

The aim of this chapter is to give an overview of the different experimental techniques and setups that have been used during this dissertation. We also provide the reader with an understanding of specific techniques that have been developed in this project. Common microscopy techniques, such as AFM, SEM and TEM for instance, are briefly reviewed in Appendix A.

3.1 Cathodoluminescence

Cathodoluminescence occurs because the impingement of a high energy electron beam onto a semiconductor will result in the pumping of electrons from the valence band into the conduction band, leaving behind holes. In a direct band gap semiconductor (such as GaAs) when an electron and a hole recombine, it is possible for a photon to be emitted. This phenomenon is known as radiative recombination. In indirect semiconductors (such as undoped silicon), the energy is likely dissipated in the emission of phonons rather than in the emission of photons.

The wavelength of the photon is defined by the band gap of the material¹. Our GaAs samples emit light at a typical wavelength of 860 nm. In GaAs, dislocations and cracks acts as non-radiative recombination centers. It means that no photons will be emitted from these locations and this effect is used to determined the crack and dislocation structure under an indentation.

Cathodoluminescence imaging is mostly performed in a SEM. The necessary setup is presented in Figure 3.1. In this case, the focused beam of electrons striking the sample makes this sample emit light from the area in the vicinity of the beam. This light is then collected by an elliptical mirror (labelled (1)), transferred via an optical fiber (labelled (2)) out of the microscope, separated by a monochromator (labelled (3)) and finally detected with a photomultiplier tube (labelled (4)). By scanning the microscope beam in an X-Y pattern and measuring the light emitted at each point of the specimen, a map of the optical activity of the sample is obtained.

Using electron microscope based techniques compared to optical microscopy techniques allows to resolve features down to 10-20 nanometres. More advanced techniques with a pico or femto-second pulsed electron beams are useful for examining low-dimensional semiconductor structures, such a quantum wells or quantum dots.

The SEM employed for cathodoluminescence experiments is a Cambridge S-360 equipped with an Oxford cathodoluminescence detector, to work in the near infrared and a monochromator. It has an LaB_6 source with 1-40 kV acceleration voltage. The photomultiplier is an avalanche diode for low noise detection.

Cathodoluminescence samples require no specific preparation and the investigated area is much larger than in TEM specimens. This allows to investigate rapidly the extension of crack and dislocations under different conditions. However, the resolution of the employed cathodoluminescence setup (~ 100 nm) does not permit to gather useful information about the exact dislocation structure under the indentation. Secondary electron and cathodoluminescence images are complementary and allow to correlate pictures of both crack field and dislocations.

¹The band gap is the energy between the valence and the conduction bands. It depends on the doping type and level and also on the crystal structure

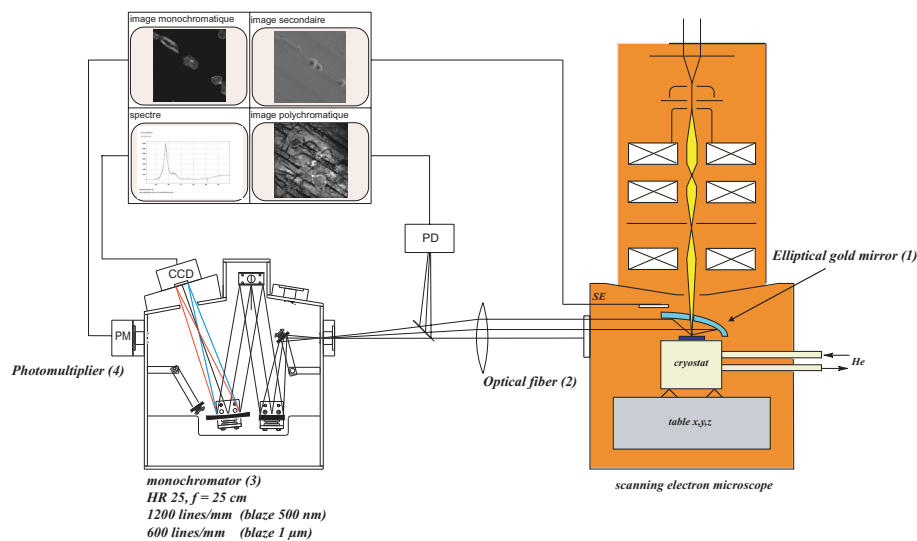


Figure 3.1: Experimental setup for cathodoluminescence investigations. (Source: J.-D. Ganière, EPFL)

3.2 Indenters

The most important parameter investigated during this work is the geometry of the indentation tool that is employed to produce cracks. If the elongated shape of wedge indenters is expected to produce a well defined half-penny crack suitable for subsequent cleavage, their finite length is also expected to introduce end-effects at their extremities. It is interesting to test various indenter geometries in order to find the best shape which minimises those end-effects. This is the reason for comparing the behaviour of GaAs for various point indenters available in our laboratory.

Indenters are generally manufactured from diamonds which are grounded to obtain the desired shape. Ideal indenters have either a sharp contact edge or a sharp contact point, defined by the geometry of the indenter envelop. In practise, however, contact edges or points are never infinitely sharp but consist of a surface with a single, respectively double radius of curvature. The edges have therefore a finite radius which varies between a few tens nanometres up to some micrometres or even more. The minimum achievable radius increases with the apex angle of the indenter.

Although diamond is an exceptionally hard material, indenter wear occurs. This phenomenon induces an evolution (generally an increase) of the indenter tip and/or edge radius with the number of indentations.

3.2.1 Wedge Indenter

Figure 3.2 shows a schematic view of the wedge indenter with a geometric description. Wedge indenters are pyramids that have an elongated contact edge (length $L = 55 \mu\text{m}$). This contact edge is expected to promote the formation of a crack of sufficient length to be used for subsequent cleavage. In addition, the elongated shape allows to consider that plane strain conditions occur in the mid-

the plane A-A of the wedge. This assumption simplifies the modelling aspects for Finite Element (FE) calculations. Since the pattern of results is expected to vary with the apex angle α , three different included angles of 60° , 90° and 120° are selected.

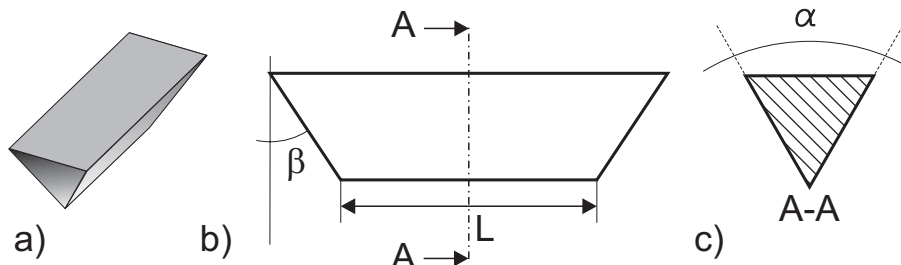


Figure 3.2: Schematic view of the wedge indenter: a) 3D view, b) lateral view and c) transversal cut A-A. Selected dimensions are $L = 55 \mu\text{m}$, $\beta = 60^\circ$ and the indenter apex angle $\alpha = 60, 90, \text{ or } 120^\circ$

For the 60° apex angle, three different indenters were used. The first one, also used for scratching and quite worn, had a radius of the contact edge of around 800 nm . The two others had their radii much smaller, in the range of 200 nm . The radii were measured with an AFM in non contact mode and in some cases, SEM pictures were made to confirm AFM measurements.

Wedge 60° , wedge 90° and wedge 120° indenters are referred to as *WE60*, *WE90* and *WE120* respectively hereafter.

3.2.2 Conical Indenters

Theoretically, the axi-symmetric shape of conical indenters suppresses stress singularities introduced by edges as for pyramidal indenters. This particularity is of great interest to explore anisotropy effects due to the crystalline structure of GaAs. However, the anisotropy of diamond makes it impossible to obtain perfectly axi-symmetric indenters and rounded edges are generally present. Such edges are much more marked on conical indenters with small included angles and evidence of this is seen in Figure 3.3.

High Resolution SEM (HRSEM) micrographs of the conical indenters having their apex angle equal to 60° and 120° are presented in Figure 3.3. The 60° conical indenter exhibits a small facet limited by two edges as shown in picture a). The tip radius of the 60° conical indenter, measured on the HRSEM micrograph, is approximately $1 \mu\text{m}$. In this latter case, the radius can not be measured with the AFM since the included angle of the indenter is too small. The tip radius of the 120° conical indenter, measured with the AFM, is approximately $2 \mu\text{m}$.

Conical 60° and conical 120° indenters are referred to as *CON60*, respectively *CON120* hereafter.

3.2.3 Pyramidal Indenters

3.2.3.1 Cube Corner

As shown in Figure 3.4, the cube corner indenter is a pyramid with a triangular base. The angle between an edge and a face (α) of the cube corner is 90° . The

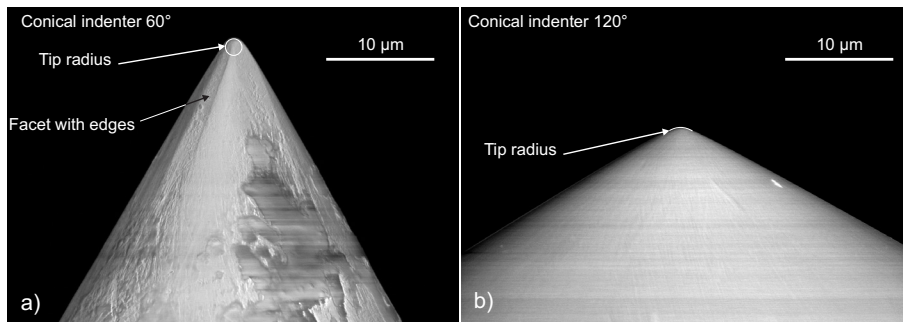


Figure 3.3: High Resolution SEM micrograph of a) a conical indenter with a 60° apex angle, showing the tip radius and manufacturing edges due to the diamond anisotropy, and b) conical indenter with apex angle equal to 120° .

three edges of the indenter associated to the small included angle makes very difficult to define a tip radius. However, based on SEM observations, the cube corner indenter is much more acute than the conical indenters.

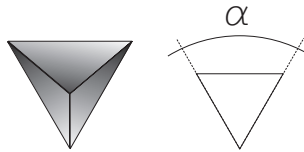


Figure 3.4: Schematic view of the cube corner indenter

The cube corner indenter is mainly used to test the failure of thin films where its sharp angle allows to generate cracks even at very low penetration depths. It has been chosen over the Berkovich one, which is more common in nanoindentation testing, since it has a much smaller included angle that facilitates imaging during in-situ SEM indentation.

The threefold symmetry of the cube corner is very different from the symmetry of the GaAs crystal. For that reason, the cube corner indenter is expected to provide results on the interaction between deformation mechanisms in GaAs and the indenter shape.

3.2.3.2 Vickers

A schematic view of the Vickers indenter is presented in Figure 3.5. The Vickers indenter is a pyramid with a square base in contrast to the cube corner indenter. It has a fourfold symmetry and the angle between the opposite faces (α) is 136° .

Vickers hardness testing machines are widely employed in materials testing. Therefore, it is commonly considered as a reference indenter in indentation fracture testing. Its widespread acceptance and the number of models that have been developed for this indenter makes it a suitable candidate to compare our results to those found in the literature.

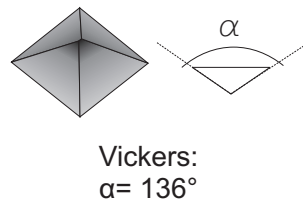


Figure 3.5: Schematic view of the Vickers indenter

3.3 Sample Preparation

3.3.1 Cross-Sectioning of Indentations

One of the goals of this work is to obtain a detailed knowledge of the subsurface damage under various indentation conditions. Such experiments can be performed through TEM investigations but at an extremely high cost and time investment. Hence, we developed two cross-sectioning techniques that take advantage of the preferential $\{110\}$ cleavage planes of GaAs to gather information about the subsurface damage caused by indentations.

The transverse cross-sectioning method consists in propagating a starter crack, obtained by scratching, across indentation sets aligned with it. The sketch in Figure 3.6 describes the different operations done in the case of wedge indentations. The cleaved surfaces are observed with an HRSEM to have a sufficient resolution.

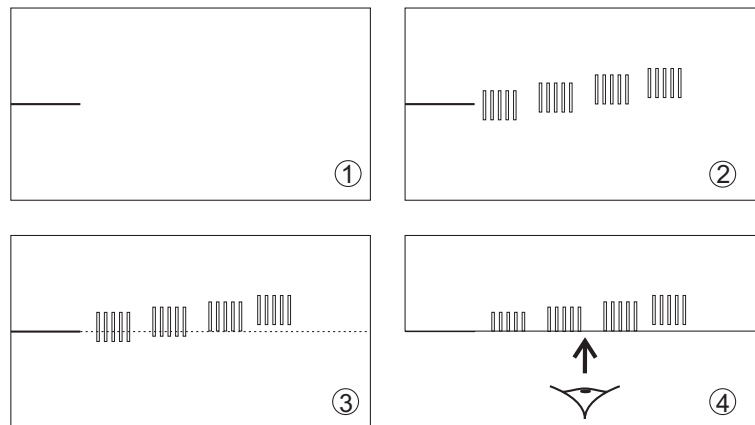


Figure 3.6: Schematic view of the transverse cross-sectioning procedure: 1), a scratch is made to generate a precursor crack. 2) several indentation sets are made with the contact edge orthogonal to the scratch track. The first set has its middle plane aligned with the scratch track, and the other sets are shifted with respect to the preceding one. 3) The sample is cleaved. 4) Observation of the cleaved surface.

In the case of WE60 indentations, the half-penny crack nucleated under indentations has generally a sufficient size to serve as a starter crack. In the *longitudinal cross-section* technique, indentations are aligned as illustrated in

Figure 3.7. The sample is then broken by using the half-penny cracks as precursors and we observe the cross-sections using either an optical microscope, an HRSEM or even an AFM.

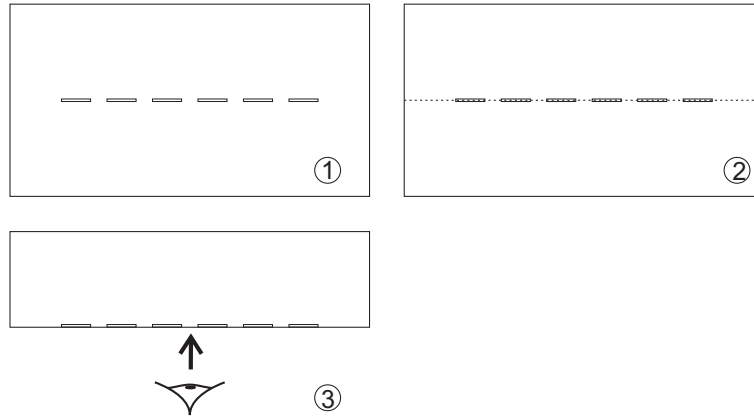


Figure 3.7: Schematic view of the longitudinal cross-sectioning procedure. 1) Indentations are made 2) the sample is cleaved through the indentations and 3) the cross-section is observed.

Figure 3.8 illustrates the different information that are collected from each technique. With the transverse cross-sectioning technique, we get the depth of the half-penny crack at the position of the cross-section, and also information about the morphology of lateral or Palmqvist cracks. In the longitudinal cross-sectioning technique, because the half-penny crack is contained in the cleavage plane, it is possible to determine the exact shape of the half-penny crack and also to measure its length and depth.

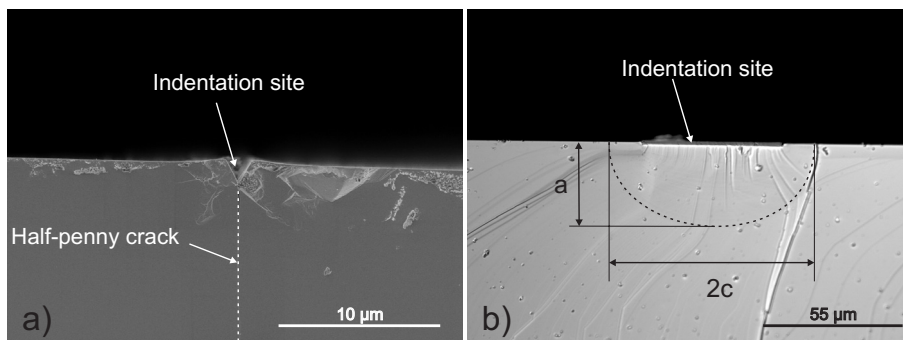


Figure 3.8: Examples showing a) a transverse cross-section and b) a longitudinal cross-section through indents.

3.3.2 Focused Ion Beam (FIB)

Focused ion beam (FIB) is a special SEM using a gallium Liquid Metal Ion Source (LMIS) instead of a focused beam of electrons to image the sample. In a Gallium LMIS, gallium metal is placed in contact with a tungsten needle and

heated. A large electric field causes ionisation and field emission of the gallium atoms. These ions are then accelerated and focused onto the sample by a set of electromagnetic lenses.

Unlike the electron microscope, the FIB is inherently destructive for the specimen. When the high-energy gallium ions strike the sample, they will sputter atoms from the surface. Gallium atoms will also be implanted into the top few nanometres of the surface thus creating an amorphous layer.

Applications of the FIB ranges from micro-machining to deposition of metal layers through Chemical Vapour Deposition (CVD) and also TEM lamella preparation.

In the specific case of TEM lamella preparation, the CVD capability is first used to deposit a sacrificial layer of platinum that protects the underlying material from sputtering or ion implantation as shown in Figure 3.9.

The sample is then milled, in order to obtain a lamella that is electron transparent (thickness typically ~ 100 nm). At the beginning of the milling operation, a relatively high emission current is used to obtain a high milling rate. When the lamella is approximately 200 nm, the emission current is decreased in order to obtain a fine polishing of the surface without ion implantation.

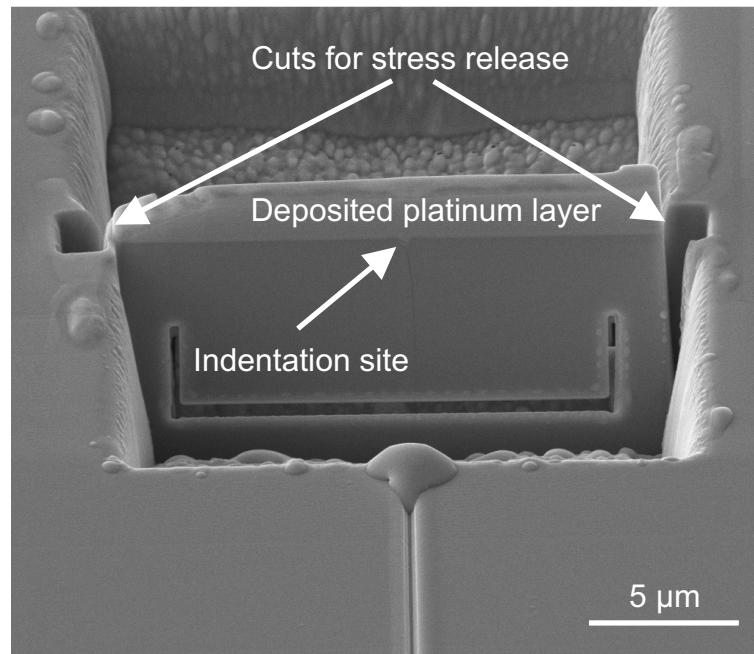


Figure 3.9: FIB micrograph of a TEM lamella during the FIB milling process.

In those cases where the lamella requires to be located at a specific place in the tested specimen, the nanometre-scale resolution of the FIB allows to cut the lamella at a precise location. This is vital, for example, in subsurface indentation damage investigations, as in our case, or in integrated circuit failure analysis.

The main drawback of FIB sample preparation is the above-mentioned surface damage and implantation as well as its cost for sample preparation (one

lamella requires about one day of preparation). A careful sample preparation usually avoids FIB induced artifacts. For instance, small cuts at the extremities of the lamella prevent the apparition of residual stresses due to ion milling.

3.4 Mechanical Testing Instruments

We performed indentation experiments using two different instruments, a commercial Nanoindenter XP from MTS corporation and an in-situ indenter specially designed to operate in a SEM.

3.4.1 Nanoindenter XP

The Nanoindenter XP is a commercial apparatus that has been developed for instrumented nanoindentation. Although it has not been specifically designed for that kind of operation, it can also be used for scratching applications.

In the Nanoindenter XP, the indenter is attached to a column positioned by a voice coil. The Z-displacement of the column is measured by a capacitance gauge with a resolution is better than 1 nm over a 2 mm range. The maximum indentation depth is 500 μm . The force is applied and measured by a voice coil actuator with a typical resolution of 50 nN over a range of 500 mN. The instrument operates under load-controlled condition. The positioning accuracy of the X-Y stage is about 1 μm .

Various indentation procedures are already implemented in the software. The most utilised procedure allows to control the maximum load, the loading rate and also the number of intermediate unload before reaching maximum load. As will be seen in Section 4.2.2.2, the procedure with intermediate unloadings allows to monitor the evolution of the crack front with the indentation load. Application-specific procedures can also be implemented in the software. As an example, we performed indentations with a cyclic loading procedure where the number of loading-unloading sequences, the maximal load, the minimum load and the loading-unloading rates are controlled. This loading program allows to do some kind of "indentation fatigue" experiments.

As it is possible to program the Nanoindenter XP so that it executes batches of experiments with various indentation conditions, it was used to perform indentations for the cross-sectioning technique.

3.4.2 In-situ SEM Indenter

The SEM indenter has been developed at the LSRO-EPFL by R. Rabe. A complete description of the system is available in his thesis [1]. The system, depicted in Figure 3.10 consists of an indentation head, and a sample holder fixed on a load cell. The latter is in turn attached to a X-Y stage.

A stack piezoactuator with a range of 20 μm actuates the indenter head on which an indenter tip is fixed. The approach of the indenter tip to the surface, is first made with the help of a manual coarse adjustment system that can be seen on the right of Figure 3.10 or by a motorised adjustment system (not shown on the figure). Accurate positioning of the sample under the tip is possible with a X-Y stage. The X-axis operates on the stick-slip principle whereas the Y-axis is

a stack piezoactuator. The main advantage of stick-slip actuators is their long range (several mm) and accurate positioning (resolution ~ 5 nm).

Recently, additional positioning systems have been developed including a Y-axis and a turning stage (also called theta stage) which both operate under the stick-slip principle. Different load cells are available with loads ranging from 500 mN up to 20 N.

During in-situ experiments, instructions are given to the instrument so that a given load level must be reached in a certain time. The system is therefore load controlled. These instructions are then converted in terms of piezo extension.

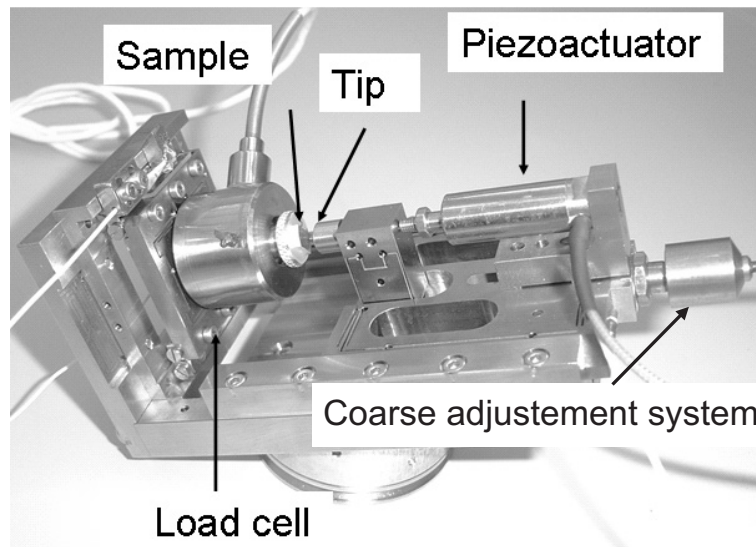


Figure 3.10: In-situ SEM microindenter setup

Bibliography

- [1] R. Rabe. *Compact test platform for in-situ nanoindentation and scratching inside a scanning electron microscope*. PhD thesis, École Polytechnique Fédérale de Lausanne, 2006.

Chapter 4

Cracks Morphologies and Cracking Sequence

4.1 Introduction

The goal of the work reported in this chapter, is to determine the influence of the indenter geometry (angle and global shape) on the crack morphologies and development.

In a first part, the results relative to the wedge indenters are presented. Cracking sequence at the surface is determined by in-situ SEM indentation and the subsurface crack field is investigated by cross-sectioning of the indents. Observations are then discussed. In the discussion, modelling aspects of the crack evolution with the indentation load are introduced.

As the wedge indenter has a finite length, it is necessary to determine the most appropriate shape that will reduce end effects and chipping-out. For that purpose, three indenter shapes (conical, cube corner and Vickers) are tested and the results are presented in a second part. For each indenter type, experimental observations concerning the indentation crack fields are presented first and observations are discussed afterwards.

Some aspects concerning slip bands will be briefly described, and they will be discussed more extensively in the next chapter. In some of the figures presented in this chapter, cracks or slip bands have been highlighted by lines to increase their visibility when the photographs are printed. The original micrographs are available in electronic format (DVD) where highlighted features are visible in their original appearance.

4.2 Wedge Indenters

4.2.1 Results

4.2.1.1 Wedge 60° Indenter

Figure 4.1 presents a series of pictures taken at different moments of the loading-unloading cycle of the wedge 60° indenter. Due to the size of the indenter, only one extremity was observed during in-situ experiments to get enough details on crack formation. In this experiment, the longer contact edge of the indenter was aligned with the [110] direction.

The cracking sequence, with reference to Figure 4.1, under a wedge 60° indenter is as follows:

1. In the early stage of the loading, surface traces of $\{111\}$ slip planes, highlighted with thin lines in Figure 4.1 a), appear on each side of the indentation outside the imprint;
2. Small Palmqvist cracks, labelled (2) in Figure 4.1, extend at the surface first. They extend preferentially along the $\langle 100 \rangle$ and $\langle 130 \rangle$ directions and propagate in $\{110\}$ planes inclined to the surface or in $\{130\}$ planes perpendicular to the surface;
3. At a given load level a half-penny crack (1) breaks through to the surface aligned with the [110] direction and included in the $(1\bar{1}0)$ plane orthogonal to the surface (Figure 4.1a)). This break-through is associated with a pop-in in the load-displacement history (Figure 4.1 f)). Palmqvist cracks (2) continue to grow;

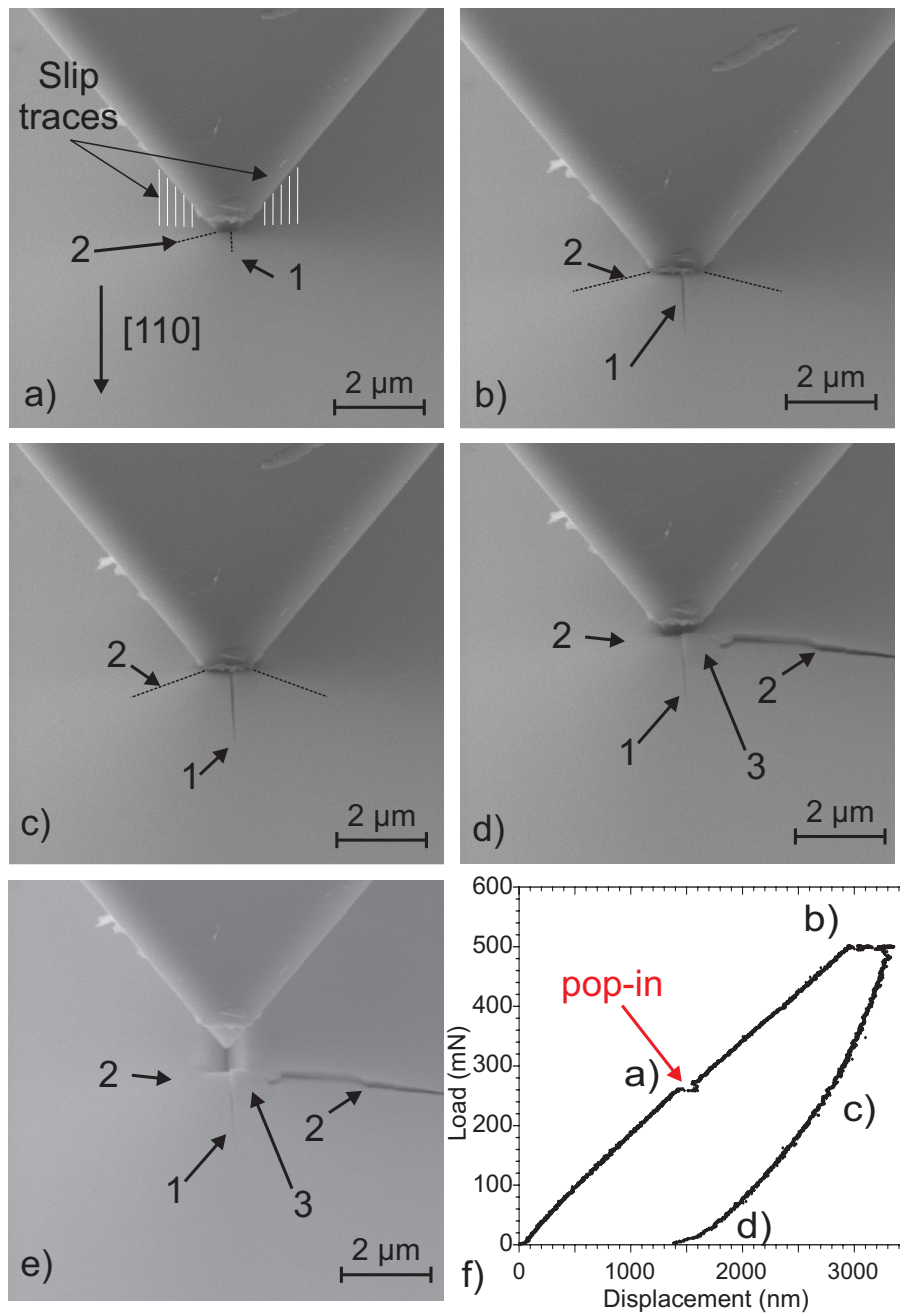


Figure 4.1: Series of micrographs of an in-situ indentation showing the cracking sequence for a wedge 60° indenter. a) half-load, shortly after the pop-in event (250 mN), b) full load (500 mN), c) half-unload (250 mN), d) full unload, e) indenter withdrawn and f) typical load-displacement curve. Arrow (1) points to the half-penny crack, arrows (2) indicate Palmqvist cracks and arrow (3) points to a chip.

4. Upon unloading, the half-penny crack (1) and the Palmqvist cracks (2) progressively close and chips (3) tend to spread-out at the very end of the unloading segment.

Chipping-out rarely occurs along the side of the wedge indenter. Most of the time, chips are confined at the extremities of the indenter and more specifically between Palmqvist cracks that extend on each side of the half-penny crack.

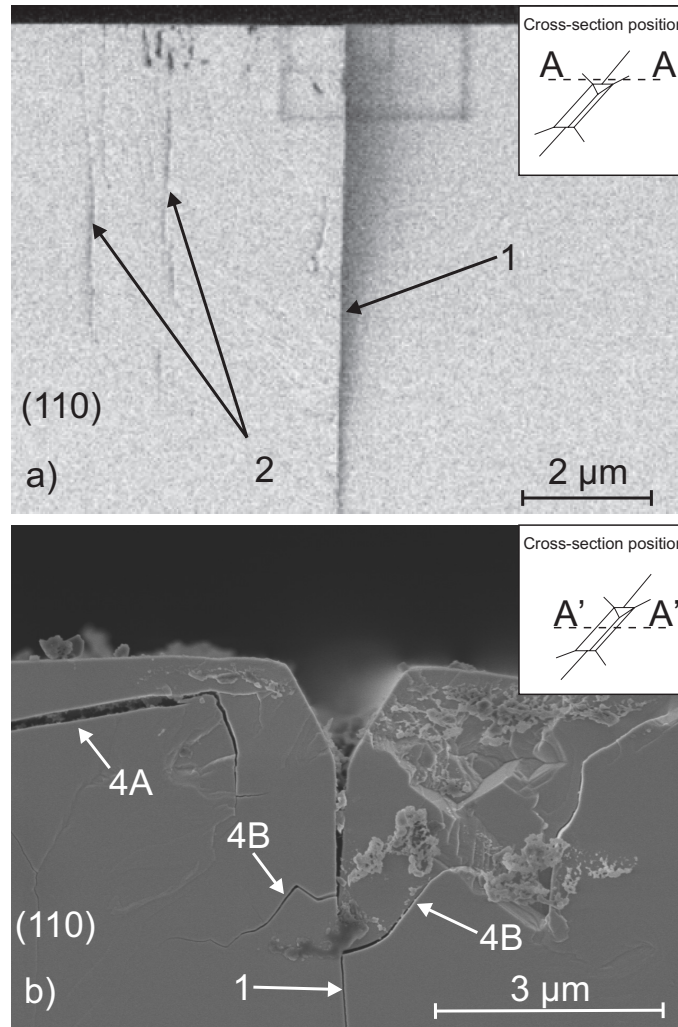


Figure 4.2: Cross-sections of wedge 60° indentations at 500 mN: a) at the extremity of the wedge, outside the residual imprint and b) in the middle of the indentation. The insets indicate the position of the cross-section with respect to the imprint

Cross-sectioning of indentations yields more information about the crack field beneath the surface. Figure 4.2 illustrates the different crack fields found a) near the end of the imprint (section A-A) and b) in the middle of the indent (section A'-A'). As can be seen, the half-penny crack (1) propagates beneath the

whole imprint. At 500 mN, the maximum depth of the crack is approximately 30 μm . In contrast, the small Palmqvist cracks (2) are shallow ones, which are observed only at the indenter extremities in Figure 4.2 a). We notice that when the cleavage plane crosses the residual imprint (as shown in Figure 4.2 b)), the cleaved surface is strongly disturbed and not in other cases. From this latter observation, we conclude that these disturbances comes from the plastic zone below the imprint. Two sets of lateral cracks (4) propagate either near the surface (4A) or more deeply in the bulk (4B).

Figure 4.3 shows the cross-section of an indentation made at 200 mN. The cross-section is located in the mid-plane A'-A' of the indentation as indicated in the inset. The load of 200 mN was chosen to illustrate the case where the maximal load is lower than the pop-in load (~ 250 mN for the used indenter).

Contrary to the case illustrated in Figure 4.2 b), no half-penny crack exists and instead, lateral cracks (4) arrange in a V-shape point toward the indent site. The angle of these cracks with the indented surface varies between 30° and around 54° corresponding to $\{111\}$ planes and the intersection point (P), when it exists, is located around 500 nm under the surface.

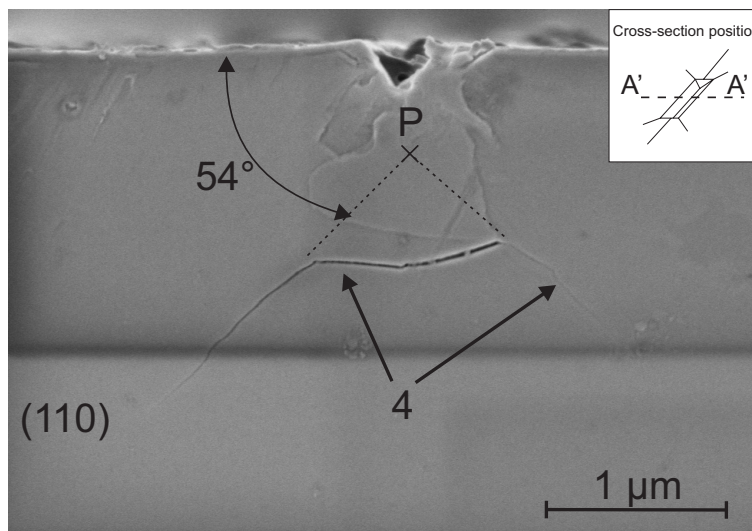


Figure 4.3: Cross-sections of wedge 60° indentation made with a maximum load of 200 mN. The inset indicates the position of the cross-section in the middle of the indentation

The longitudinal cross-section (plane B-B) of an indent with a load of 500 mN presented in Figure 4.4 a) reveals the well defined semi-elliptical shape of the half-penny crack (1) that has been high-lighted for convenience. Careful examination of the indentation extremities provides additional information about chips and lateral cracks. As an example, Figure 4.4 b) is a magnification (SEM image) of the area located near one extremity of the indentation. This last micrograph shows a chip (3) that spreads-out from the indentation. Traces of short lateral cracks (4A) are visible at the apex of the imprint or along the indentation walls (i.e. the surface in contact with the indenter). The lateral crack labelled (4B) runs under the whole indentation following a semi-elliptical

path. These cracks have been high-lighted to enhance their visibility.

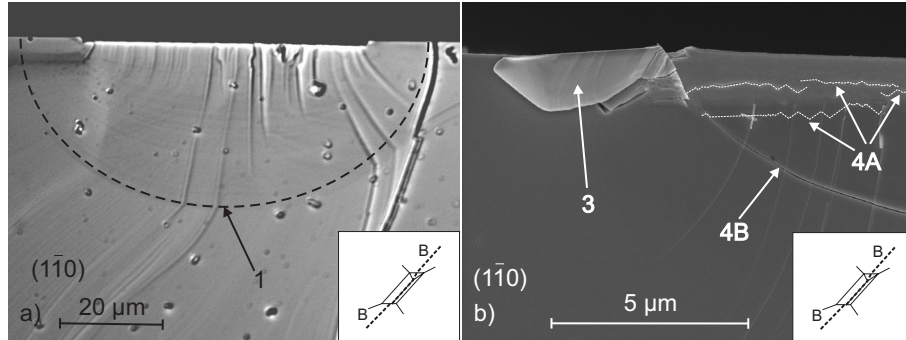


Figure 4.4: Longitudinal cross-section from a wedge 60° indentation made with a maximal load of 500 mN: a) Optical micrograph and b) SEM close-up on one extremity of the residual impression.

4.2.1.2 Wedge 120° Indenter

The rather large included angle of the wedge 120° indenter limits in-situ observations. Despite this limitation, in-situ experiments were conducted at loads up to 1.5 N to investigate the correlation between the load and the crack development. The load of 1.5 N was chosen in order to stay within the limits of the employed load cell.

Figure 4.5 shows a series of micrographs taken during such experiments and the corresponding load-displacement curve. The orientation of the wedge indenter is the same as in the wedge 60° case, i.e. the contact edge is aligned with the $[110]$ direction.

The cracking sequence at the surface is as follows:

1. Upon loading, Palmqvist cracks (2) initiates at the indenter corner.
2. During the unloading, chips are sometimes initiated at the indenter extremities.

By comparing the results between the 120° and 60° wedge indenters, we observe several differences:

- slip bands are located inside the residual imprint;
- the half-penny crack is rarely observable at the surface even at loads up to 1.5 N;
- the load-displacement curve do not exhibit the characteristic pop-in excursion;
- at comparable load (500 mN for instance), Palmqvist cracks as well as chipping-out occurrences are strongly reduced and their lengths are considerably shortened.

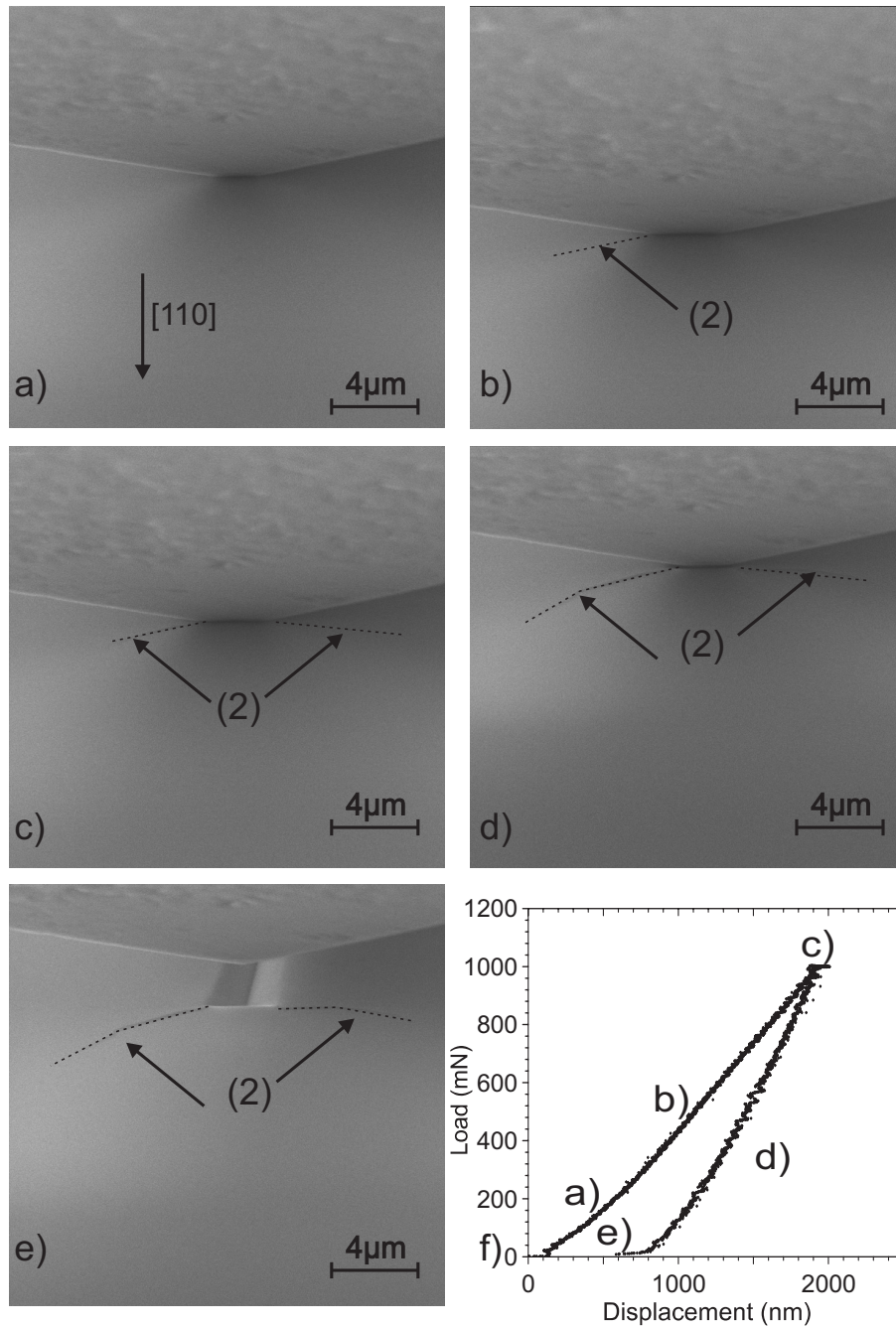


Figure 4.5: Series of micrographs of an in-situ indentation showing the cracking sequence for a wedge 120° indenter at a load of 1 N: a) half load (500 mN), b) full load (1 N), c) half unload (500 mN), d) full unload, e) indenter withdrawn and f) corresponding load-displacement curve. Arrows (2) point to Palmqvist cracks.

The examination of a cross-section taken in the middle of the indentation, and presented in Figure 4.6, shows that although no crack is observable at the surface, a network of lateral cracks (4) is present under the indentation. The pattern of lateral cracks found under 120° wedge indentations in the investigated load range (0-1.5 N) is similar to the pattern observed under 60° wedge indentations when the maximum load is less than the pop-in load (i.e. when no half-penny crack is created).

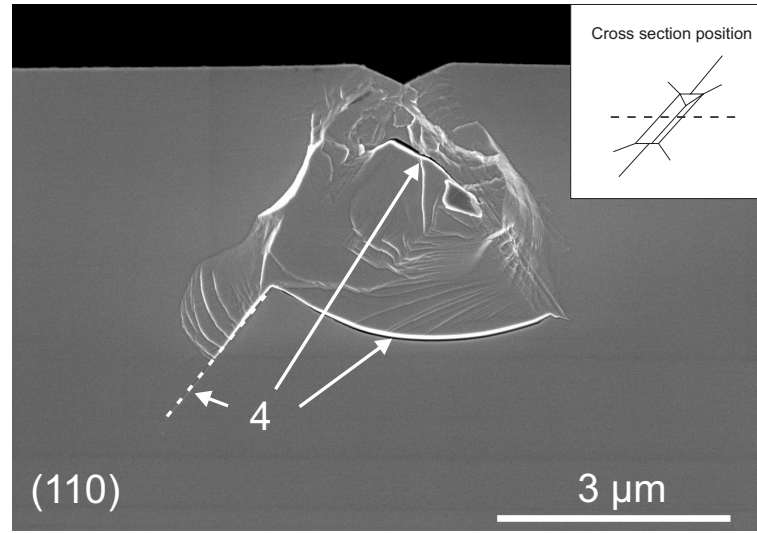


Figure 4.6: Cross-section of a wedge 120° indentation at 500 mN: the insets indicate the position of the cross-section with respect to the imprint. (110) is the cleavage plane and [110] direction points out of the sheet. Arrow (4) indicates the position of lateral cracks.

4.2.2 Discussion

4.2.2.1 Load-Displacement Curves

In-situ SEM indentations have demonstrated that, at least when the edge of the indenter is aligned with the [110] direction, the pop-in within the wedge 60° load-displacement curve is related to the formation and extension of the half-penny crack to the surface. This affirmation is supported by two other experimental observations:

- transverse cross-sections of indentations made with a maximal load smaller than the pop-in load reveal no trace of the half-penny crack as evidenced in Figure 4.3;
- the examination of longitudinal cross-sections of 60° wedge indentations shows that the half-penny crack is not a subsequent development of a median (circular) crack as observed by Lawn [1] in glasses.

In the orthogonal $[\bar{1}\bar{1}0]$ direction, pop-in is generally smaller and sometimes disappears. This point is discussed in more details in Section 5.3.1. As the

pop-in excursion is related to the sudden nucleation of the half-penny crack, it is intuitively expected that many experimental parameters (such as the wedge length, the indenter radius, the indenter angle, ...) will influence the pop-in load. Our experimental observations have demonstrated the influence of two of them: the radius of the indenter edge and the loading rate. Figure 4.7 reports on the influence of these two parameters on the pop-in load.

First, the effect of the edge radius is evidenced in Figure 4.7, where we compare the mean pop-in load of a worn and a new indenter having an edge radius of 800 and 200 nm respectively. On this graph, we see that, at a given loading rate, the pop-in load is about three times larger when the indenter radius is 800 nm compared to the one with a 200 nm radius.

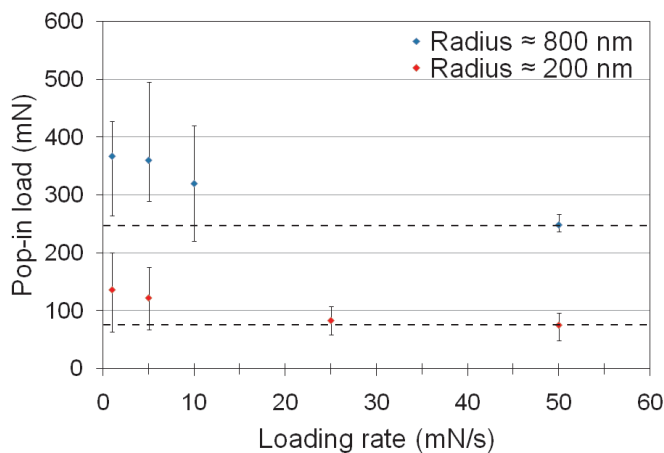


Figure 4.7: Mean load of pop-in as a function of the loading rate and the indenter radius. Error bars represent minimum and maximum values on a batch of a minimum of 10 indentations.

In order to gain some insight into this phenomenon, we performed simulations with the commercial finite element code Abaqus. Details about the simulation procedure are given in Appendix C.

We simulated 60°wedge indentations experiments with indenters that have an edge radii varying between 100 and 600 nm. In the model, GaAs is assumed to behave as an elasto-plastic solid with an orthotropic elastic stiffness matrix and a yield point of 2.54 GPa. The Von Mises criterion is chosen to determine points where yielding occurs. The maximal load is fixed at 50 mN in order to avoid too much distortion of the mesh that would have required a re-meshing procedure. We focus on the S11 component of stress (see Figure 4.8 for definition of S11) since this stress corresponds to the opening mode of the half-penny crack. Its evolution along the symmetry axis \mathcal{Z} of the indenter is plotted for various indenter radii in Figure 4.8.

In the first 100 nm below the surface, we have a numerical instability in evaluating the stress S11 for the wedge with a 100 nm radius. This instability, probably due to mesh distortion, is not found for the other indenters. In the immediate vicinity of the indenter the stress S11 is compressive. The absolute value of the compressive stress rapidly diminishes and a transition between

compressive and tensile stresses takes place at around 400 nm below the surface. Further down, the tensile stress reaches a peak value approximately 500 nm under the surface and progressively diminishes to a near zero asymptotic value. If we compare the S_{11} and the Von Mises stress distributions, we observe that the peak value of the tensile stress is reached at the boundary between the plastic and the elastic zones.

As can be seen, the edge radius strongly affects the maximum tensile stress. The ratio of the tensile stresses obtained in the two extreme cases ($R \sim 100$ and 600 nm) is approximately 2.3. We see that the drop by a factor of three in the pop-in load roughly corresponds to an increase by a factor of two in the tensile stress. These results indicate a strong interaction between the load at which the half-penny crack nucleates (i.e. the pop-in load) and the level of tensile stress that is reached below the indenter. Because the maximum tensile stress is dependent on the edge radius, we can rationalise the dependence of the pop-in load on the indenter radius.

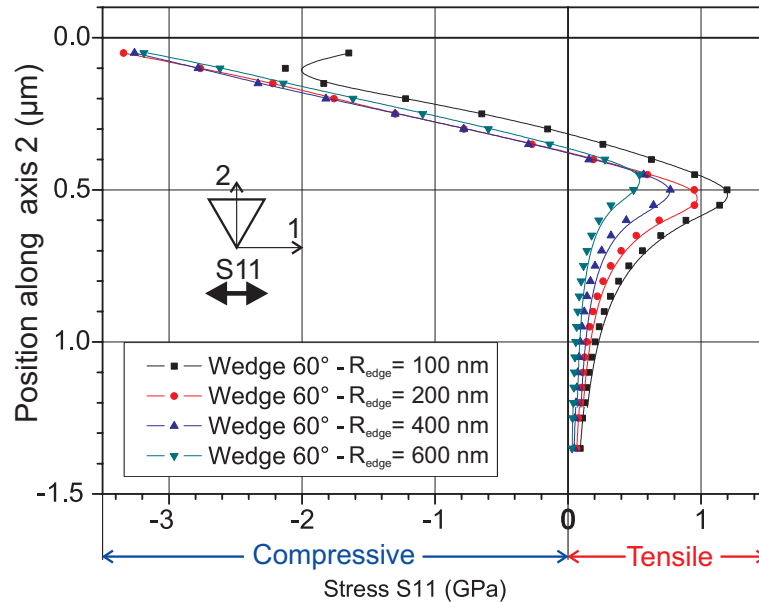


Figure 4.8: Evolution of the S_{11} stress along the symmetry axis of the indenter with the edge radii. The S_{11} stress is the opening stress component for half-penny cracks.

We remark that the tensile stress reaches its maximum value a few hundreds of nanometres below the surface. It is interesting to compare this result to observations of what we call "edge indentations" experiments. "Edge indentations" were performed to look at the formation of both the half-penny and lateral cracks. Figure 4.9 presents the scheme for such an experiment, where the indenter is slightly shifted from the wafer so that a few microns of the main edge are not in contact with the wafer. Figure 4.9 also shows three frames (numbered 139, 140 and 141) that have been extracted from a video of a 60° wedge indentation. In frame 139, no trace of crack is visible. The arrow in frame 140 points to the half-penny crack formed a few microns below the surface. Finally,

in frame 141 (more than half a second later), the half-penny crack has reached the surface.

It would be oversimplistic to directly correlate results from FE simulations and from edge indentation experiments since 1) the FE model used is not representative of the real behaviour of GaAs and 2) edge indentations present really different boundary conditions from FE simulations and also from conventional experiments. Nevertheless, these experiments show that the crack does not necessarily initiate from the surface. They also raise the question of the origin of the defects at the origin of the half-penny crack formation: are these defects preexisting in the material or are they created by the indentation?

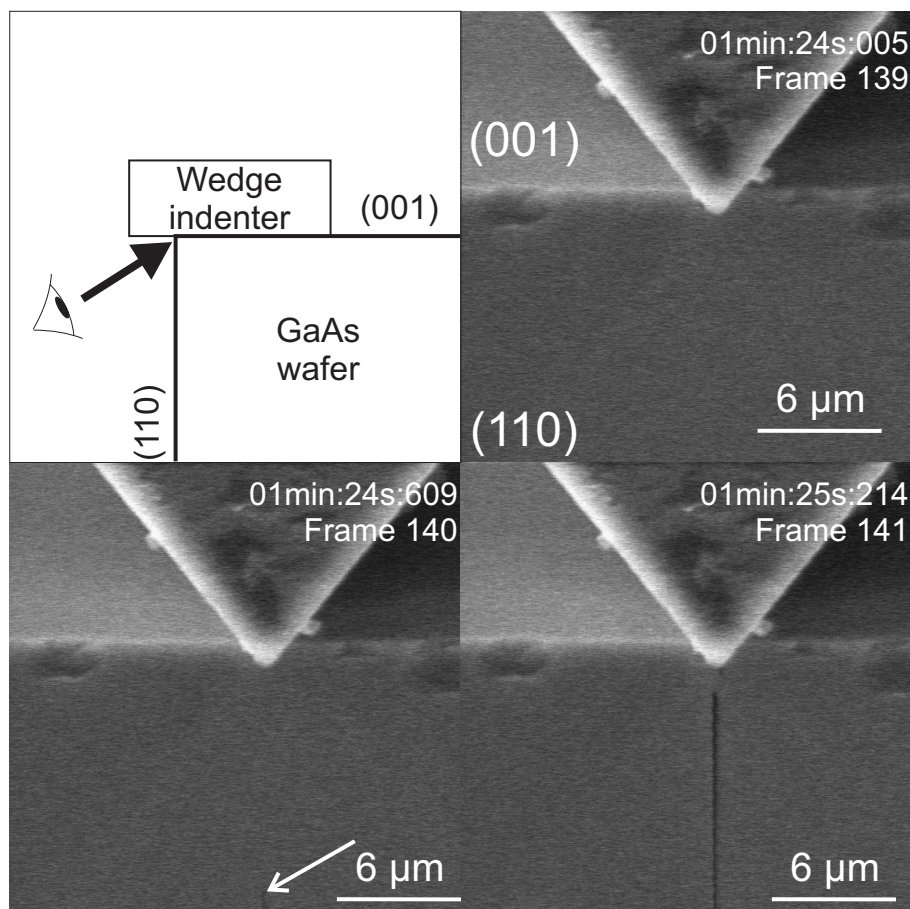


Figure 4.9: Sequence of three images extracted from an in-situ SEM indentation experiments. The indented face is (001) and the observed face is (110). This sequence shows the nucleation of the half-penny crack in the depth.

The effect of the loading rate on the pop-in load can be seen in Figure 4.7. For the two employed indenters, the loading rate varies between 1 and 50 mN/s. As the loading rate increases from 1 to 50 mN/s, the mean load of pop-in slowly decreases down to an asymptotic value of approximately 80 mN (respectively 250 mN) for an indenter radius of 200 nm (respectively 800 nm).

This tendency to behave in a more brittle manner has been already observed by Fujita *et al* [2] and Maeda *et al* [3], who investigated the Brittle to Ductile Transition (BDT) under Vickers indentation in GaAs. In their study, these authors demonstrate that the BDT is controlled by the mobility of dislocations. A similar approach by Yonenaga and Sumino [4] has shown that the Upper Yield Stress τ_{uy} , defined as the stress level necessary to nucleate dislocations, depends on both strain rate $\dot{\epsilon}$ and temperature T according to the following relation:

$$\tau = A \dot{\epsilon}^{1/n} \exp\left(\frac{U}{k_B T}\right) \quad (4.1)$$

where A and n are material constants, U is an activation energy and k_B the Boltzmann constant.

In the case of indentation of GaAs, the loading rate variation is one order of magnitude. As a first approximation, we assume that the corresponding strain rate variation is also one order of magnitude. The variation in the upper yield stress induced by a change of one order of magnitude in the strain rate is obtained from Equation 4.1 and corresponds to :

$$\frac{\Delta\tau_{uy}}{\tau_{uy}} = 10^{1/n} - 1 \quad (4.2)$$

Introducing $n = 3.6$ in Equation 4.2 (the value of n is obtained from [5]), we obtain:

$$\frac{\Delta\tau_{uy}}{\tau_{uy}} = 0.89 \quad (4.3)$$

So, a variation of one order of magnitude in the strain rate increases τ_{uy} nearly by a factor two. Based on this last result, we see that it is possible to account for the effect of an increasing strain rate in FE models by increasing the yield stress. Several simulations performed with various yield stress have shown that an increase of the yield stress affects both the hydrostatic pressure (which increases) and the plastically deformed area (i.e. the plastic zone is smaller). This result suggests that as the loading rate is increased, GaAs will have a greater tendency to behave as a brittle material as frequently observed for metals.

We now evaluate the fracture energy of GaAs for the $\langle 110 \rangle$ planes from experimental data. The principle of the energetic analysis of the load-displacement curve conducted in the following paragraph is analogous to the determination of the ERR with the compliance method presented in Section 2.4. Such analysis allows us to determine the energy released in crack formation U_s and consequently the cleavage surface energy of GaAs γ_c .

Figure 4.10 a) presents the load-displacement curves for two distinct experiments performed under similar conditions. In the first case (black curve), the first unloading occurs before the pop-in and so before the half-penny crack formation. In the second case (red curve), the first unloading occurs after the formation of the half-penny crack. The hysteresis loop in the unloading-reloading sequence indicates that a dissipative process takes place during this sequence. For the sake of clarity, these two loading cases are sketched in Figure 4.10 b).

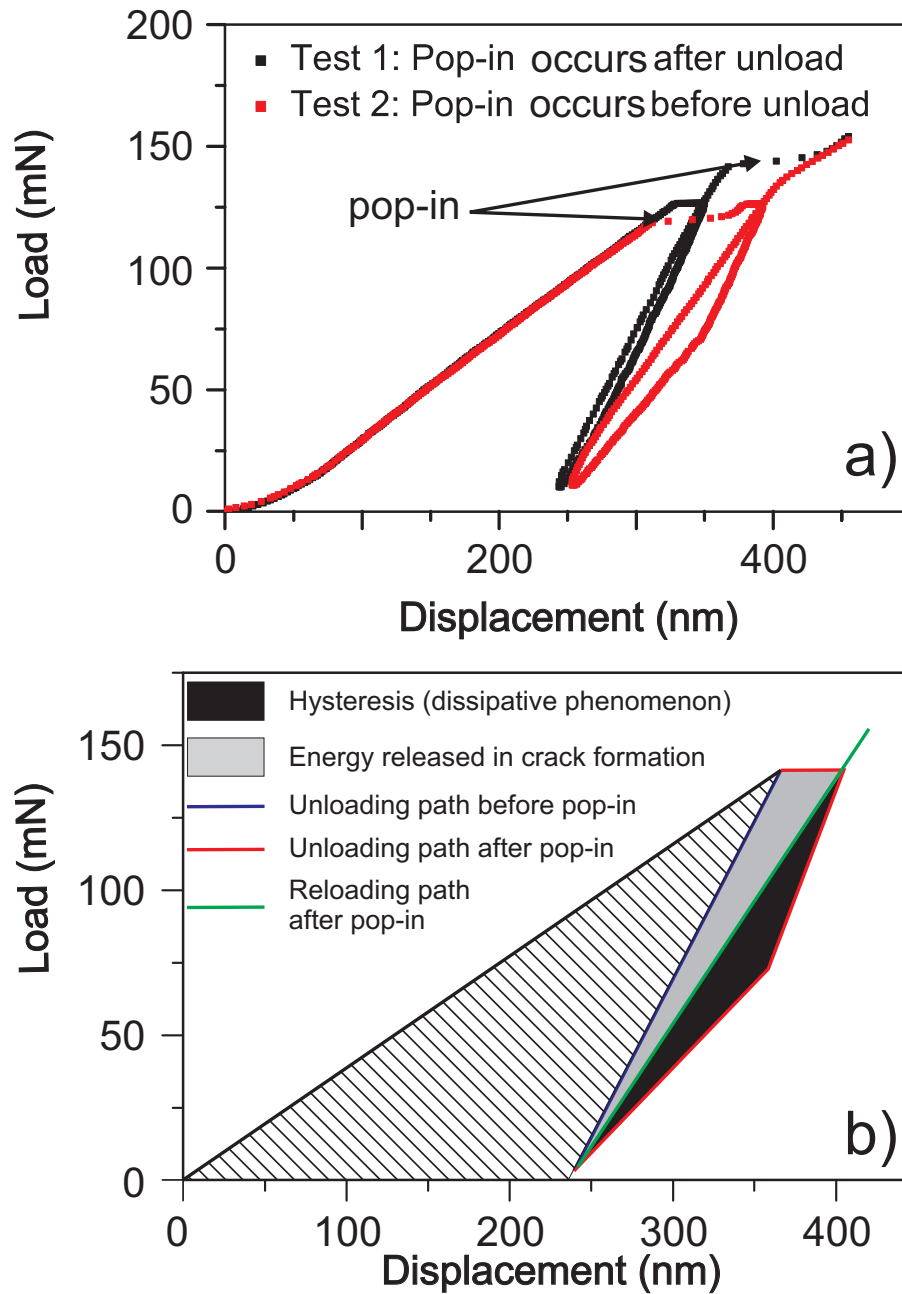


Figure 4.10: Indentation curve of two wedge 60° indentations with partial unload. The elbow in the unload part is due to half-penny crack extension to the surface.

Considering the two different states, before crack propagation, we have neither pop-in nor hysteresis in the load-displacement curve and the energy is dissipated essentially into plastic deformation (hatched area in Figure 4.10 b). After the half-penny crack has formed, the loading-unloading sequence corresponds to the black and red curves. The difference in energy between the two states (before and after crack propagation) corresponds to the area comprised between the two unloading paths (blue and red curves). This energy is separated into two terms: the first one (highlighted in black) corresponds to a dissipative phenomena (hysteresis loop). The second term (highlighted in grey) corresponds to the elastic energy released during and absorbed in the crack formation. In the present case, the energy released in crack formation U_s is about $2.7 \cdot 10^{-9} J$.

The length and depth of the crack were determined by carefully examining the longitudinal cross-section of the indentation with an AFM, and the surface S measured in this case is $1313 \mu m^2$. The cleavage surface energy is then determined according to:

$$2\gamma_c = \frac{U_s}{S} \quad (4.4)$$

and we obtain $\gamma_c = 1.03 J/m^2$ for the cleavage surface energy of GaAs.

This experimental value is somewhat larger but compares well with the ones reported by Messmer and Billelo [6] and Wasmer *et al.* [7] which are respectively $0.86 J/m^2$ and $0.69 J/m^2$ for (110) planes of GaAs. This discrepancy might be explained by the fact that the determination of the cleavage energy with this method is sensitive to errors in the measurement of the crack size, the pop-in load and length. As an example, a variation of $1 \mu m$ (typical error on the measurement) on crack length and depth results in a change of the cleavage surface energy of $\pm 0.14 J/m^2$. It would be interesting to obtain such estimations from several experiments in order to obtain a mean value and verify their reproducibility. Such experiments, however, require to find a reliable way to implement the pop-in as a trigger for the unloading which has not been implemented yet.

Figure 4.11 is the complete load-displacement curve of the first experiment presented in Figure 4.10 a). It has been performed with two intermediate unloading at 125 and 250 mN. The first unloading segment is almost straight and the pop-in excursion is only visible after reloading to a load of around 150 mN. The two subsequent unloading segments present a slope change at approximately 66 % of the maximum load. This phenomenon, also representative of a dissipative phenomenon not fully understood, is systematically and exclusively observed after the pop-in excursion and not before. For that reason, it can be interpreted as an additional indicator of the half-penny crack nucleation.

To summarise this section, we have first correlated the pop-in in the load-displacement curve with the nucleation of the half-penny crack when the indenter edge is aligned with the [110] direction. The influence of the indenter edge radius on the pop-in load has been rationalised in terms of a change in the value of the maximum tensile stress below the indenter at a given load. Simple estimates based on dislocation dynamics suggest that the dependence of the nucleation of the half-penny crack on loading rate could be attributable to changes in the upper yield stress of the crystal. The cleavage surface energy of GaAs has then been derived from the analysis of load-displacement curves and a good

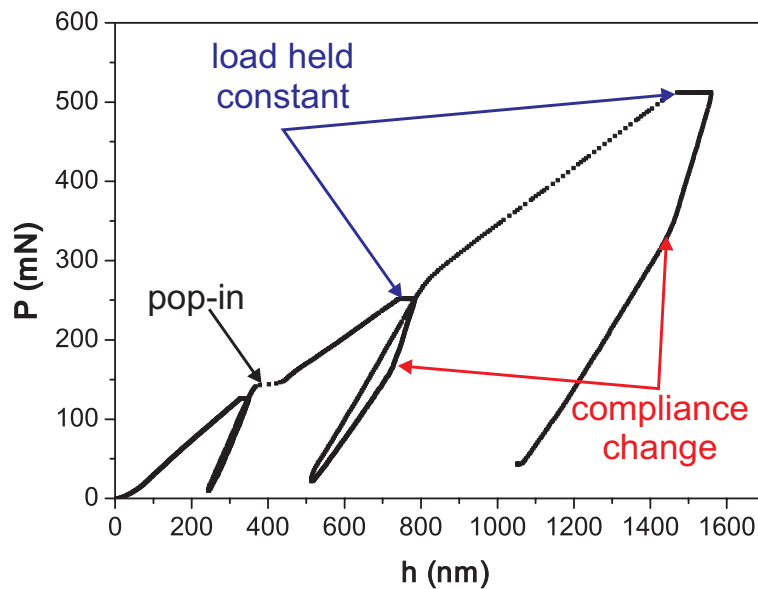


Figure 4.11: Load displacement curve of an experiment showing the unloading segment before and after nucleation of the half-penny crack. The first unloading segment is straight and occurs before pop-in whereas the two others exhibit a compliance change.

agreement has been found with values from previous studies. It has also been shown that the slope changes in the unloading part of the load-displacement curves is an indication of the half-penny crack formation. By simply looking at the load-displacement curves, we thus have two indicators to ensure that a half-penny crack has formed. These features are precious indicators that might be helpful in dicing applications as will be seen in Chapter 6.

4.2.2.2 Analysis of the Half-Penny Cracks (60° Wedge Indenter)

Wasmer *et al.* [7, 8, 9] have shown a direct relationship between the crack geometry (length and depth), and the quality of subsequently cleaved surfaces. The larger the precursor crack is, the lower the force needed to break the sample, and the better the quality of the cleaved surfaces.

In this section, we want to establish the relation between the maximum indentation load and the final half-penny crack size in 60° wedge experiments. In order to establish this relationship, we use the following methodology:

- definition of the phenomenology of the cracking process during indentation;
- definition of the model and the associated hypothesis;
- use of experimental data points within the model.

From the in-situ SEM experiments, we know that cracking sequence during a wedge indentation consists of three phases:

- during the pop-in, there is a dynamic initiation of the half-penny crack. This initiation phase consists in the creation of the half-penny crack immediately followed by its sudden propagation up to a certain size;
- then, there is a quasi-static growth of the half-penny crack as the load is progressively increased up to the maximum load;
- at last, during the unloading phase, the half-penny crack progressively close.

In order to model the half-penny crack evolution with the indentation load, we introduce some hypothesis:

1. we concentrate on the phase of quasi-static growth of the half-penny crack. In other words, we eliminate all the experimental points that are below or close to the load of pop-in (dynamic initiation);
2. we assume that the final crack size depends only on the maximum load employed;
3. we assume that there is no plasticity at the crack tip and that SIF solutions are valid;
4. we assume that the loading configuration can be simplified into the Center Loaded Half-Penny Crack configuration described in Section 2.4;
5. the fracture toughness¹ is a constant property of the material, independent of the direction.

The model used for our purpose is the weight function developed by Fett et Munz [10] and described in Section 2.4. In that model, we remind that the SIF at the surface and at the deepest point of the crack are written as follows:

$$K_{Surf} = \frac{F_T * f_1\left(\frac{a}{c}\right)}{c^{3/2}} \quad (4.5a)$$

$$K_{Depth} = \frac{F_T * f_2\left(\frac{a}{c}\right)}{c a^{1/2}} \quad (4.5b)$$

As the crack propagation is quasi-static, we might consider as a first approximation that at crack extension $K_{Surf} = K_{Depth} = K_c$. We rewrite Equations 4.5a and 4.5b in the form:

$$F_T * f_1\left(\frac{a}{c}\right) = K_{Surf} c^{3/2} = K_c c^{3/2} \text{ (at crack extension)} \quad (4.6a)$$

$$F_T * f_2\left(\frac{a}{c}\right) = K_{Depth} c a^{1/2} = K_c c a^{1/2} \text{ (at crack extension)} \quad (4.6b)$$

We then report experimental values of a , c and F_T in Equations 4.6a and 4.6b, and plot the first term of these equations versus $c^{3/2}$ and $c.a^{1/2}$ respectively. The slope of the linear fit of experimental data points gives an estimate of the indentation fracture toughness K_c of GaAs.

¹for a given crystallographic plane, {110} plane in our case

The first interesting feature of the CLHPC model concerns the monitoring of the evolution of the half-penny crack shape with the applied load. Such monitoring is achieved by looking at longitudinal cross-sections of indentations in which the load has been applied in three steps with intermediate unloading sequences. The careful examination of the subsequent longitudinal cross-section with an AFM reveals semi-elliptical marks produced at crack front arrests (i.e. at intermediate unloading). Figure 4.12 illustrates such an experiment and the associated observation. Three distinct marks are visible and show the evolution of the crack front from an elongated semi-elliptical shape at low load (125 mN), to a rounded semi-elliptical shape, close to the semi-circular geometry at 500 mN.

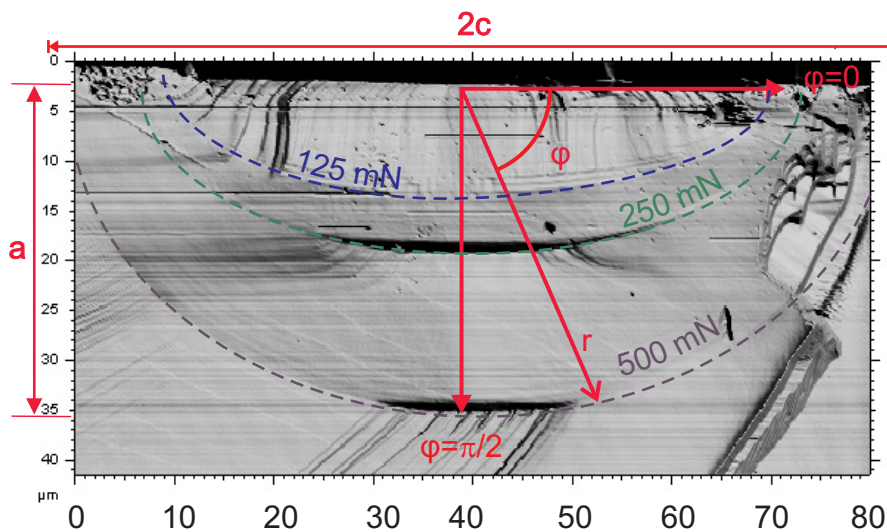


Figure 4.12: AFM micrograph of the cross-section of a wedge 60° indentation with the load applied in three steps (125/250/500 mN). Radius of the tip is 200 nm.

The weight function corresponding to the CLHPC configuration is given in Section 2.4, Equation 2.16. The evolution of the weight function along the crack front (angle φ) is plotted in Figure 4.13 for several a/c ratios. The curves corresponding to the crack front at 250 and 500 mN (a/c respectively equal to 0.5 and 0.8) are highlighted in Figure 4.13.

Two important conclusions are drawn from this graph:

1. at low a/c ratios (i.e. when the indentation load is ≤ 250 mN), the SIF is higher at the deepest point than at the surface and because of this unbalance in K , the crack tends to grow toward a semi-circular shape.
2. when the a/c ratio increases (i.e. when the a/c ratio tends to 0.8), the SIF values at the surface and in the depth become roughly equal and the crack tends to grow in a self-similar shape.

As is well known from fatigue and fracture studies in metals [11, 12], the weight function model explains well the evolution of the crack front from a semi-elliptical shape at low indentation loads toward a half-penny crack shape

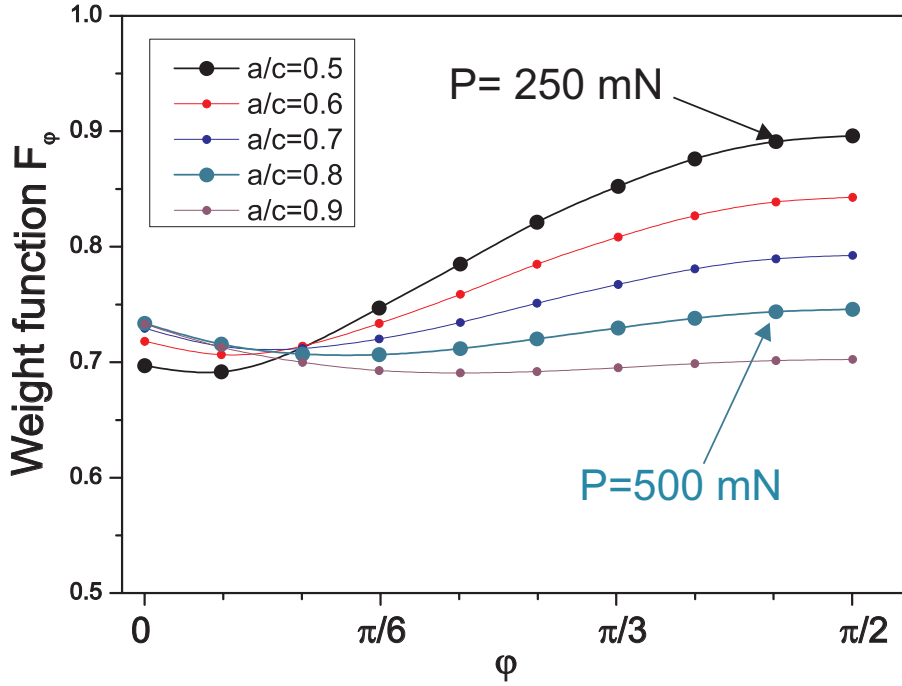


Figure 4.13: Evolution of the weight function for various a/c ratios. When $\varphi = 0$, the weight function is calculated at the surface, and when $\varphi = \pi/2$ the weight function is calculated at the deepest point of the crack.

at higher indentation loads. Our experimental observations show that the SIF solution works for single crystals as well and that the CLHPC configuration is also a good approximation of the wedge loading configuration.

We performed several batches of experiments with the maximum indentation load varied between 150 mN and 500 mN. The pop-in load in all these experiments was comprised between 80 and 120 mN². For each experiment, the crack length c and depth a were measured. The resulting data are introduced in Equations 4.6a and 4.6b, which are then plotted in Figure 4.14.

The dashed lines in Figure 4.14 represent the linear regression by the least square fit method of the experimental data points. The slope of the linear regression gives the indentation fracture toughness and we obtain $K_c = 0.38 \pm 0.04$ MPa $m^{1/2}$ (respectively $K_c = 0.44 \pm 0.05$ MPa $m^{1/2}$) at the deepest point (respectively at the surface).

The indentation fracture toughness values we determine with the help of the CLHPC model agree well with experimental values usually obtained for (110) GaAs planes [13, 14] ($0.44 - 0.49$ MPa $m^{1/2}$). This result suggest that the CLHPC configuration is a rather good approximation for the case of the wedge indentation.

The quality of the linear fit is affected by the rather important scatter in experimental data (R^2 is equal to 0.76, respectively 0.74 for K_{Depth} and K_{Surf}).

²Note that in all cases the pop-in load is well below the maximum indentation load used. This condition is necessary to exclude points that represent dynamical effects.

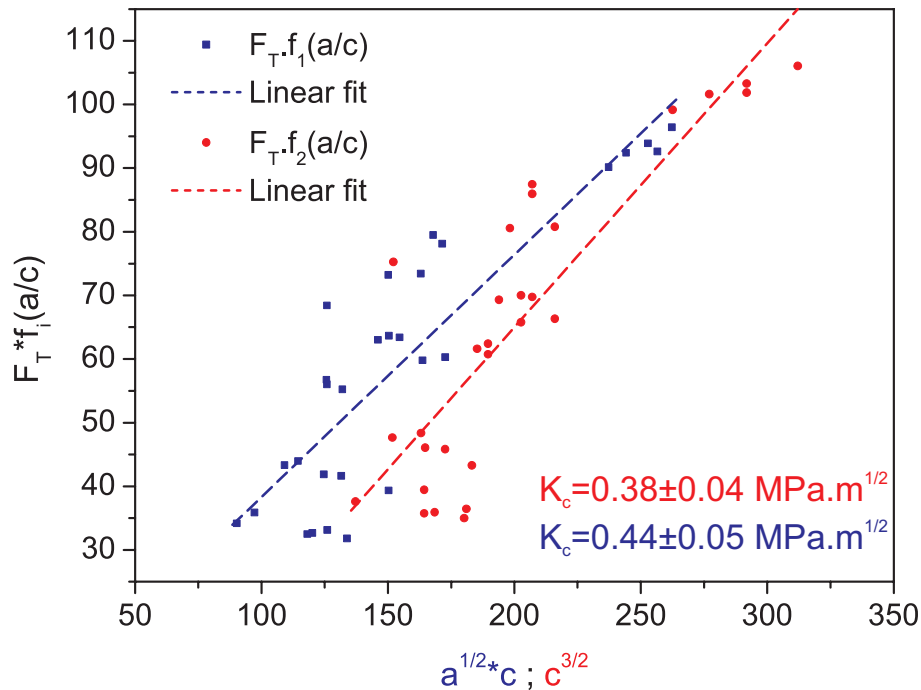


Figure 4.14: Plot of the crack length (black) and depth (red) with the indentation load.

We would like to make a last comment on the effect of the indenter apex angle. Although this parameter has not been experimentally investigated (only a 60° wedge indenter is used), it indirectly appears in the CLHPC model. Indeed, we recall that the force F_T used in the model is written:

$$F_T = \frac{P * \cot(\psi)}{2} \quad (4.7)$$

where ψ is the indenter half angle and P , the indentation load.

For a given indentation load P , Figure 4.15 plots the evolution of F_T with ψ . Obviously F_T rapidly drops as the indenter apex angle increases. Therefore, we see that acute wedge indenters significantly facilitates the propagation of the half-penny crack.

4.2.2.3 Palmqvist Cracks, Lateral Cracks and Flaking

For the sake of clarity, we recall that a crack is defined by a direction, given by the trace of the crack at the indented surface, and then by a crystallographic plane in which it propagates.

Palmqvist cracks are located at the extremities of the indentation imprint as shown in Figures 4.1 and 4.5. Palmqvist cracks are in general not straight. For that reason, the angle (measured with respect to the $[110]$ direction) is measured at the intersection of the crack with the imprint. In Figure 4.16 the

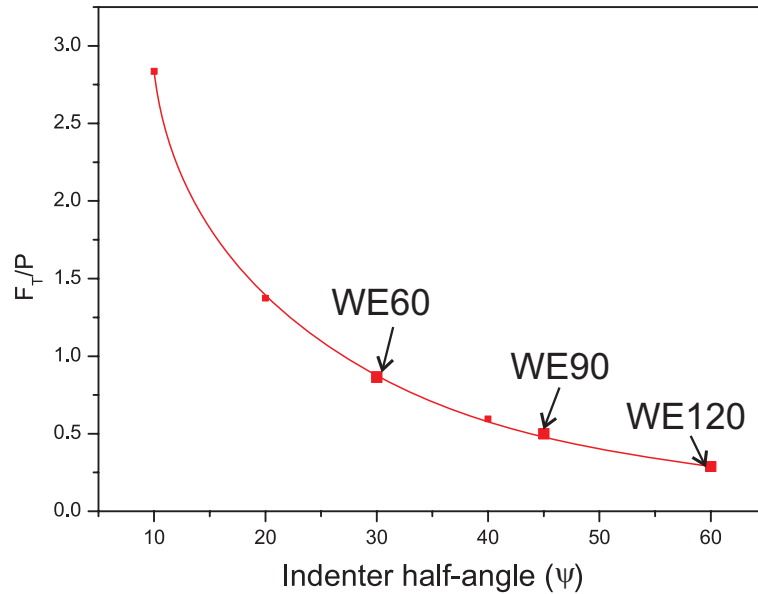


Figure 4.15: Plot showing the evolution of F_T with the half angle of the indenter (φ).

results for three batches³ of wedge experiments are shown in the form of a polar distribution (length and angle) of Palmqvist cracks with respect to the indentation site.

Palmqvist cracks are preferentially oriented along the $\langle 100 \rangle$ and $\langle 130 \rangle$ directions. Most of the time, these cracks propagate in planes which form an acute angle with the indented surface (see the Palmqvist crack on the right side of indentation Figure 4.17 a)). In some cases however, Palmqvist cracks were observed perpendicularly to the indented surface (see Figure 4.2 a)).

We also see that when the apex angle is changed from 60° to 120° or the load is reduced to 200 mN, Palmqvist cracks are rarely observed and their lengths are strongly reduced.

The analysis of the polar graph presented in Figure 4.16 shows that there is a large scatter in the lengths of Palmqvist cracks as well as in the planes in which these cracks propagate. The graph also points to the asymmetry in the pattern of cracks depending on the indenter extremity that is observed. Palmqvist cracks are less present and shorter in the polar graph on the bottom of Figure 4.16 than on the one on the top. This is especially clear when a lower maximum load (200 mN, red points) or a more obtuse indenter (120° wedge indenter, blue points) is employed. This asymmetry is due to the fact that the contact edge of the wedge is slightly inclined to the surface. Due to this inclination, one extremity of the wedge indenter contacts the surface before the other and the initial contact is rather made on a point than on a line. Palmqvist cracks initiate earlier at the first contact point and are hence longer.

After a few microns, Palmqvist cracks often bifurcate and merge with lateral

³a batch consists of 25 indentations performed in similar conditions of load, indenter geometry and indenter orientation

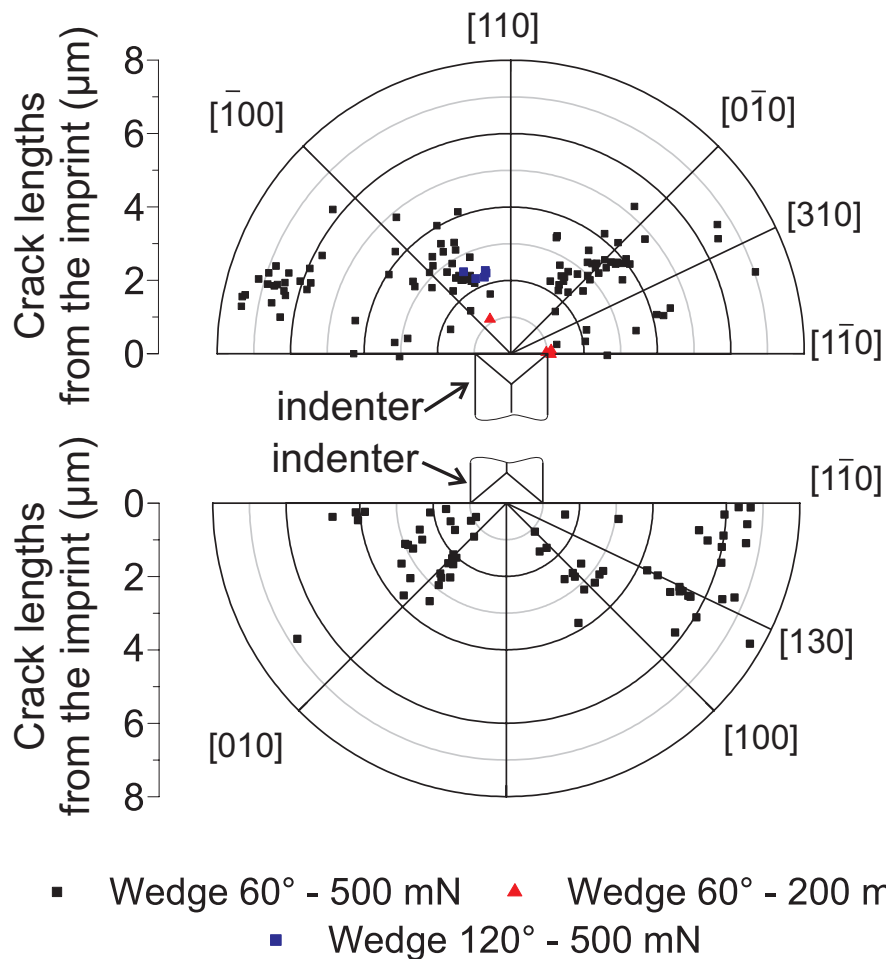


Figure 4.16: Polar plot of the distribution of the trace of Palmqvist cracks at the surface with respect to the indentation for wedge 60° at 200 and 500 mN, and wedge 120° at 500 mN. The small schematics indicates the extremity of the wedge indenter that is observed.

cracks to form a chip as seen in Figure 4.17. This chipping-out takes place in the vicinity of the imprint extremities either between two sets of Palmqvist cracks (see Figure 4.17 a)) or along the side of the indenter (see Figure 4.17 b)).

The propagation of lateral cracks is highly related to both the maximum load of the test and the indenter included angle. As lateral crack propagate below the surface, it is difficult to give the exact cracking sequence. In-situ observations have demonstrated that lateral cracks emerge at the surface during the last stage of the unloading sequence. The observation of transverse cross-sections of indentation before and after pop-in shows a significant difference in the crack field:

- when no half-penny crack is created (i.e. 60° indenter before pop-in or 120° wedge indenter), we observe lateral cracks approximately 1 μm below

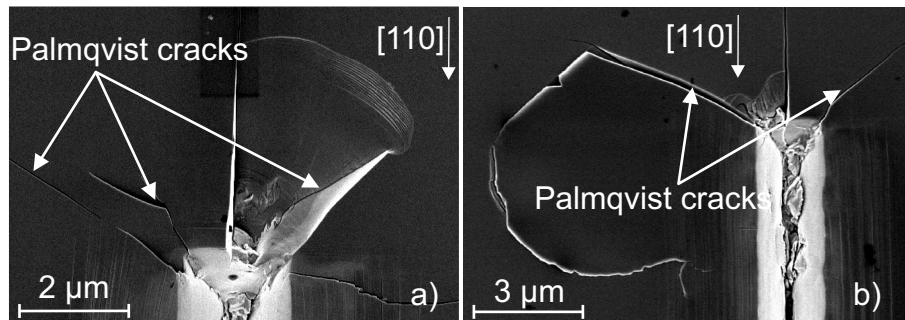


Figure 4.17: Illustration of various places where chipping out takes place with the wedge 60° indenter

the imprint. In that case, cracks arrange in a V shape that points to the surface (see Figure 4.3 for example) and are relatively short. They sometimes follow $\{111\}$ slip planes as seen in Figure 4.3 and do not emerge at the surface.

- On the contrary, if a half-penny crack has nucleated, the V shape arrangement is more rarely observed. In this latter case, lateral cracks nucleate more deeply in the material and often emerge at the surface.

The influence of the half-penny crack on the lateral crack formation suggests that lateral cracks nucleate and propagate after the half-penny crack formation. It is not sure whether this nucleation step occurs during the loading or unloading phase. However, the observation of "edge indentations" suggests that the nucleation step occurs during the loading sequence. In that case, lateral cracks propagate toward the depth during the loading sequence and during unloading they bifurcate to reach the surface. As the conditions achieved during "edge indentations" are different from the one achieved during normal indentations, due caution must be exercised when considering these results. The propagation of lateral cracks along $\{111\}$ planes might be explained by a concentration of dislocations into slip bands extending along some $\{111\}$ planes that makes it easier to propagate cracks in these planes.

The SEM micrographs in Figure 4.18 are magnified views of longitudinal cross-sections taken under 60° wedge indentations made with a 500 mN load. The careful examination of the area just beneath the imprint reveals a complicated network of lateral cracks. At low loading rate (1 mN/s, Figure 4.18 a)), we observe a single crack running under the whole indentation. In contrast, when the loading rate is increased to 100 mN/s (Figure 4.18 b)), numerous cracks are visible and the depth at which they are observed is increased to 4 μm .

In order to compare the level of damage at different loading rates, we have conducted observations on indentations performed at loading rates of 1 mN/s and 100 mN/s. For each loading rate condition, three indentations were observed. To measure the level of damage, we delimit an area of 5 μm (the maximum depth at which lateral cracks are observed) running under the whole indentation (approximately 55 μm). Then, by using an appropriate image treatment method (detailed in Appendix B) we determine the cumulated length of cracks (sum of the lengths of all cracks).

At 1 mN/sec, this cumulated length is comprised between 117 and 144 μm and traces of lateral cracks are concentrated in the imprint or in its immediate vicinity. In comparison, at 100 mN/s, the cumulated length of cracks is comprised between 424 and 571 μm (almost four times longer) and the maximal depth at which cracks are found is approximately 4 μm .

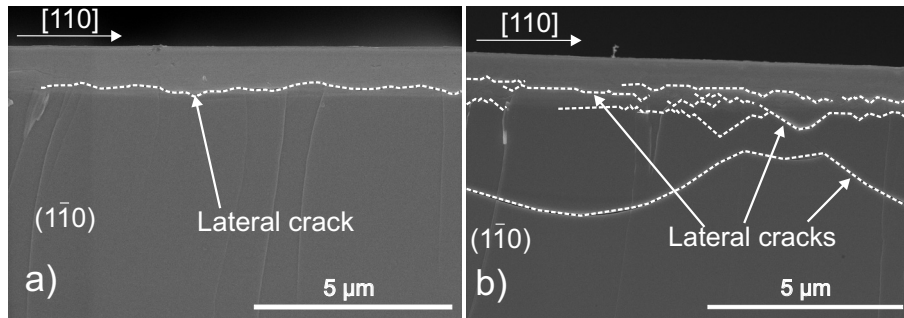


Figure 4.18: SEM micrographs of longitudinal cross-sections of wedge 60° indentations made at a) 1 mN/s and b) 100 mN/s. Maximum load 500 mN. The boundary of the imprint is delimited by the crack.

As it is the merging of Palmqvist and lateral cracks that causes chips to form, it is obvious that the depth of lateral cracks controls the amount of material removed from the indentation site through chipping-out. Therefore, in the industrial context of this study, it appears that low indentation speed (i.e. loading rate) would help decreasing the potential level of chipping-out. Our experiments have shown that up to 50 mN/s, the amount of lateral cracks increases in a limited manner (cumulated length of lateral cracks 155 μm at 50 mN/s).

4.3 Point Indenters

4.3.1 Results

In this section, it is useful to recall the definition of half-penny and Palmqvist cracks given in Section 2.3. The term of half-penny cracks refers to the cracks that propagate in the (110) and $(\bar{1}\bar{1}0)$ planes that are perpendicular to the indented (001) surface. Their traces at the surface are therefore aligned with the $[\bar{1}\bar{1}0]$ (respectively $[110]$) directions.

As will be seen in the next paragraphs, in the case of point indenters, the term of Palmqvist cracks applies to cracks that are aligned with the $\langle 100 \rangle$ directions. In addition, the planes in which these cracks propagate belong to a family of $\{110\}$ planes **that are not orthogonal** to the indented surface.

4.3.1.1 Conical 60°

Figure 4.19 shows SEM micrographs of an in-situ indentation made with a conical tip having a 60° apex angle and the corresponding load-displacement curve. The maximum load is 500 mN and the experiment is interrupted at different moments in order to take pictures. During that time, the load is held constant during approximately 60 seconds. This explains the first two plateaus

observed on the loading curve in Figure 4.19 f), the third one being related to the formation of chips (4) visible on Figure 4.19 c).

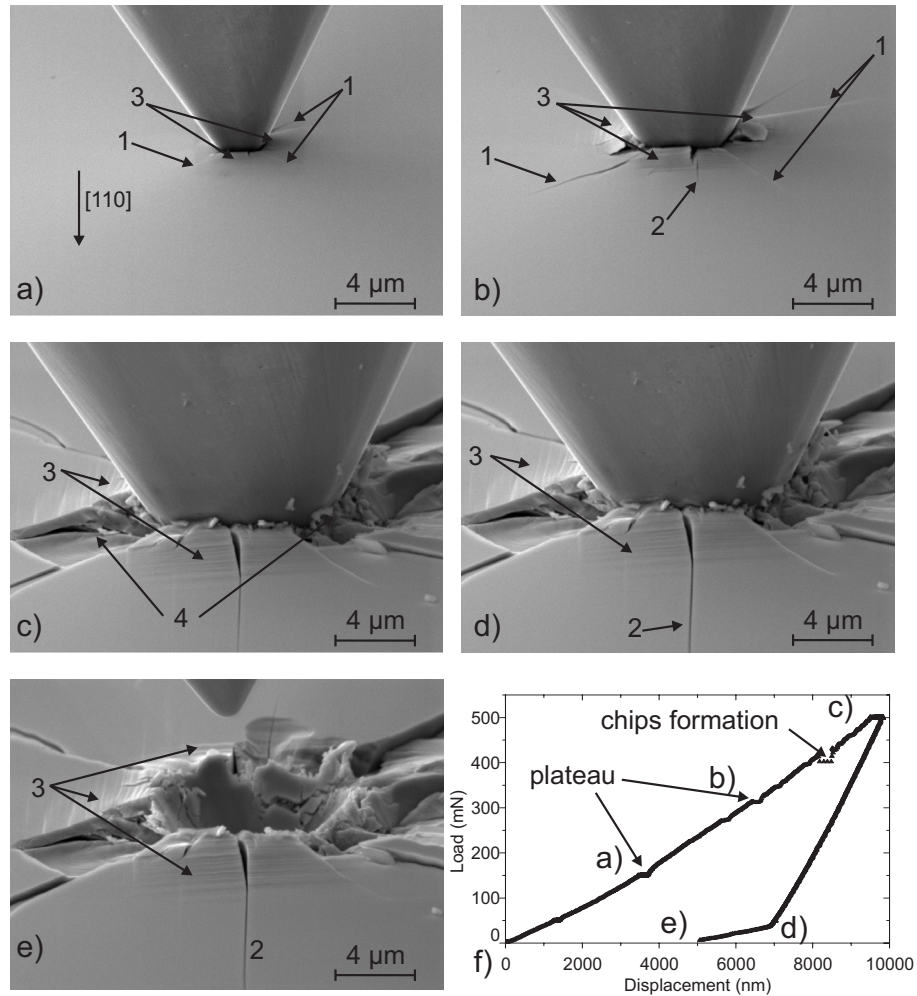


Figure 4.19: Series of micrographs of an in-situ indentation showing the cracking sequence for a conical 60° indenter. a) first plateau load (150 mN), b) half load (250 mN), c) full load (500mN), d) full unload, e) indenter withdrawn and f) corresponding load-displacement curve. Arrows (1) points to Palmqvist cracks, arrows (2) point to half-penny cracks, arrows (3) to slip lines and arrows (4) point to area in the surface where chips have broken-off.

The cracking sequence for the 60° conical indenter is as follows:

1. plastic deformation occurs first and traces of slip bands (arrows labelled (3)) are visible *outside* the indentation imprint⁴. This indenter activates four slip planes ((111), ($\bar{1}11$), ($1\bar{1}1$), ($\bar{1}\bar{1}1$));

⁴although slip traces at the surface are hardly visible in the earliest steps of in-situ SEM indentation, the observation of the residual imprints of low load indentations shows that slip traces are present before cracks.

2. a set of Palmqvist cracks (1) aligned with either $[100]$ or $[010]$ directions nucleates in the early stage of loading (Figure 4.19 a));
3. shortly after, a set of half-penny cracks (2) aligned with the $[110]$ or $[\bar{1}\bar{1}0]$ directions extend at the surface and Palmqvist cracks (1) continue to grow (Figure 4.19 b));
4. upon unload, Palmqvist cracks (1) and half-penny cracks (2) progressively close and chips (4) break through at the surface (not shown here).
5. when high loads are employed, chips also form at the end of the loading cycle (Figure 4.19 c))

Figure 4.20 illustrates the typical star-like pattern encountered with the conical 60° indenter. Palmqvist cracks (1) develop along $\langle 100 \rangle$ directions and their length is quite important. We also see that half-penny cracks of the set (2A) are asymmetric with respect to the imprint and propagate in two different $\langle 110 \rangle$ planes. Finally, only one crack of the half-penny set (2B) aligned with $[\bar{1}\bar{1}0]$ is visible.

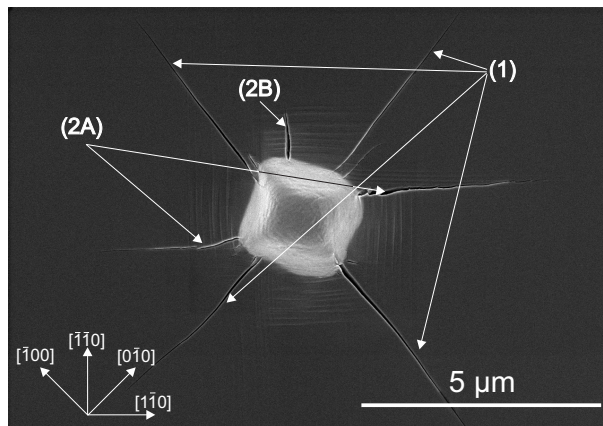


Figure 4.20: The residual imprint and crack system of a conical 60° indentation. (2A) and (2B) denote half-penny cracks propagating along $\langle 110 \rangle$ directions and (1) Palmqvist cracks extending in the $\langle 100 \rangle$ directions.

The subsequent cross-sectioning of indentations provides more information about the crack field beneath the surface. Figure 4.21 represents a cross-sectional view of two conical 60° indentations. In Figure 4.21 a), the cleavage plane crosses the indentation in its mid plane, whereas in Figure 4.21 b) it has been slightly shifted. In this experiment, a maximum load of 200 mN is applied with two intermediate unloading sequences at 50 and 100 mN in order to create crack front arrest lines. The insets indicate the position of the cuts with respect to the indentation sites.

At first, it is worthwhile to note that with this kind of indenter (and more generally with point indenters as will be seen later), the cleaved surface is heavily damaged. A comparison of Figures 4.20 and 4.21 b) demonstrates that traces of Palmqvist cracks (1) are not perpendicular to the indented surface. Instead,

they make a 45° angle with the (001) indentation plane and we conclude that Palmqvist cracks extend in the $\{101\}$ family of planes.

The different crack front arrest lines of the half-penny crack (2A) in Figure 4.21 are highlighted by thin dotted lines. The observation of river lines (RL) that extend from the second crack front arrest line suggests that mixed mode I/III is introduced [15, 16] during the cleavage step. Such result is coherent with previous observations of Ballif *et al.* where it was shown that the experimental setup used for cleavage operations introduces a strong component of mode III during the cleavage step [17]. This might explain why the RL pattern is more visible on the last crack front and not on the other one generated during the indentation step.

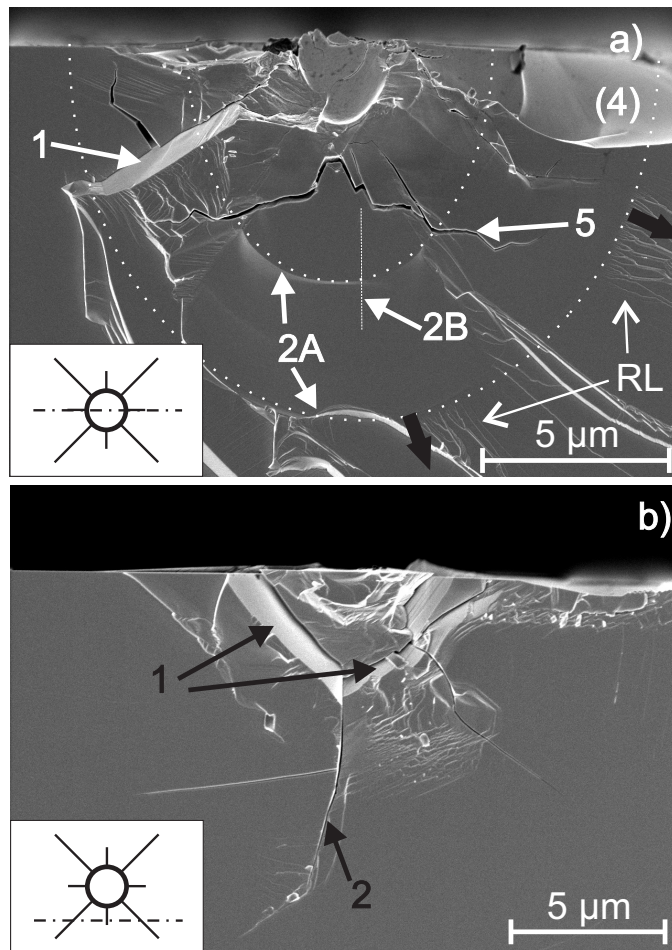


Figure 4.21: Cross-section of conical 60° indentations: a) in the middle of the residual imprint, b) outside the residual imprint. Dotted curves highlight the different arrested crack fronts. Additional features not labelled are caused by cross-sectioning.

A trace of the half-penny crack (2B), perpendicular to the cleaved surface is hardly visible (highlighted with a dashed line in Figure 4.21 a)). This half-

penny crack does not break through the imprint. The path of lateral cracks labelled (5) is complicated. Lateral cracks initiate a few hundred nanometres under the apex of the imprint. They go abruptly deeper in the material before bifurcating. After they bifurcate, lateral cracks then run nearly parallel to the indented surface. One also remarks that a chip (4) located near the surface has spread out.

4.3.1.2 Conical 120°

An in-situ indentation made with the conical indenter having a 120° apex angle is presented in Figure 4.22. The cracking sequence and the star-like pattern of cracks are identical to the conical 60° case except for chips which form only during unloading in the range of loads (0-500 mN) investigated.

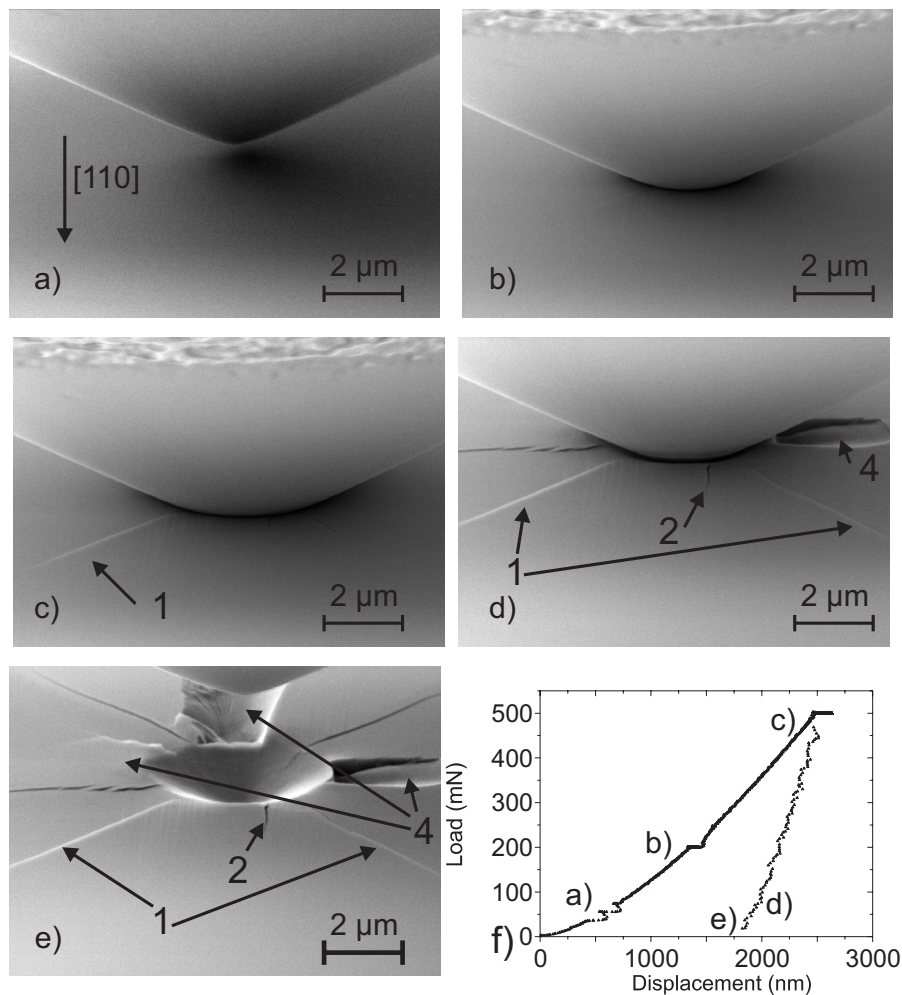


Figure 4.22: Series of micrographs of an in-situ indentation showing the cracking sequence for a conical 120° indenter. a) before indentation , b) half load (250 mN), c) full load (500mN), d) full unload, e) indenter withdrawn and f) corresponding load-displacement curve.

The cracking sequence for the cone 120° indenter is as follows:

1. GaAs is plastically deformed and traces of slip bands (not visible here) appear inside the residual imprint;
2. Palmqvist cracks (1) and half-penny cracks (2) initiate during the loading sequence (Figure 4.22 c), the half-penny crack (2) is hardly noticeable);
3. upon unloading several chips (4) spread at the surface, generally following $\langle 110 \rangle$ orientations (Figure 4.22 d) and e)).

A micrograph of the residual imprint of a 120° conical indentation is presented in Figure 4.23 a). It is seen that Palmqvist cracks (1) initiate at the crossing of slip bands. These slip bands (3) are mainly located *inside* the residual imprint. Palmqvist cracks (1) are aligned with $\langle 100 \rangle$ directions and the cross-sectioning of indentations reveals that they propagate in $\{110\}$ planes as in the case of 60° conical indentations. In the range of loads investigated, Palmqvist cracks (1) are always visible while half-penny cracks (2) (not visible here) are rarely observed. The magnified view presented in Figure 4.23 b) shows the presence of small microcracks (6) that develop along the traces of slip bands, inside the imprint. These microcracks are found in the vicinity of Palmqvist cracks (1).

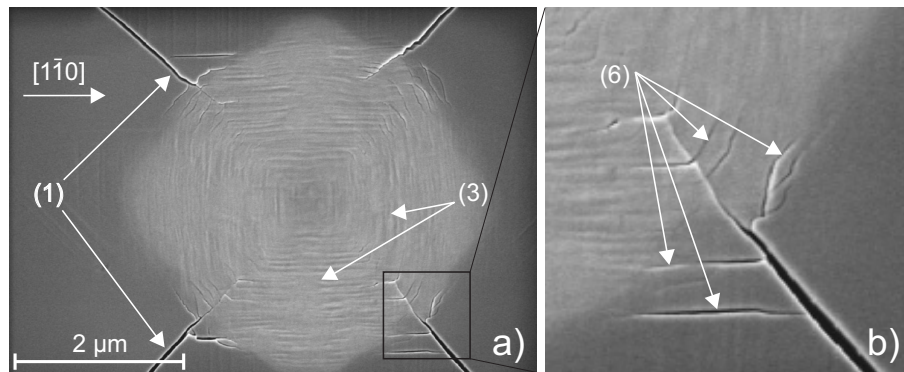


Figure 4.23: SEM micrographs showing a) the residual imprint of a conical 120° indentation with Palmqvist cracks (1) and traces of slip bands (3) inside the imprint, b) a magnified view showing crack (6) that initiate at the intersection of slip bands (3).

Observation of cross-sections of a conical 120° indentation in Figure 4.24 shows a complicated network of cracks below the surface. On the tilted view of the cross-section presented in Figure 4.24 a), we observe shallow lateral (5a) cracks and deep lateral cracks (5b). Shallow lateral cracks (5a) are located on the sides of the indent, near the surface whereas deep lateral cracks (5b) meet approximately 2 μm below the apex of the imprint (as for the 60° conical indenter).

The magnified view in Figure 4.24 b) shows the area near the apex of the imprint. The intersection of a half-penny crack (2) (propagating in a $(1\bar{1}0)$ plane) with the cleavage plane is highlighted with a dotted line and the network of deep lateral cracks (5b) is enhanced on this view.

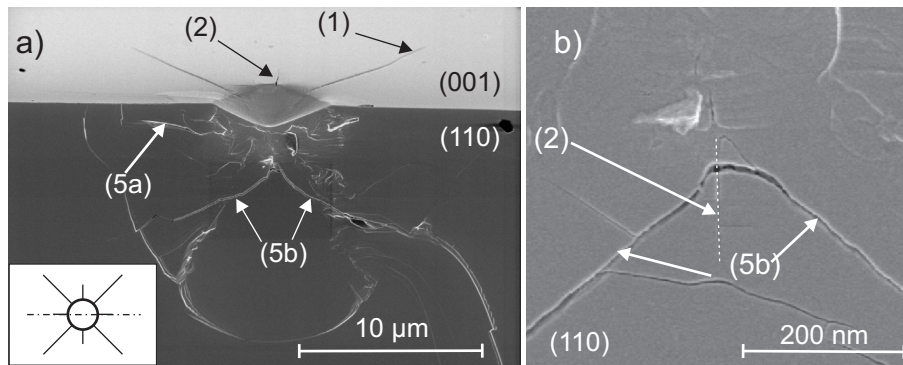


Figure 4.24: Cross-section of a conical 120° indentation. a) tilted view showing the indented (001) and cleaved (110) surfaces. Palmqvist cracks (1) and a half-penny crack (2) are visible on the top of the picture whereas the intersection of shallow (5a) and deep (5b) lateral cracks with the (110) cleavage plane are visible. b) Magnification of the area near the apex of the imprint.

4.3.1.3 Cube Corner

Figure 4.25 shows an in-situ indentation with a cube corner indenter. During the experiments, the edge (A) of the indenter is aligned with the $[110]$ direction (see Figure 4.25 a)).

The typical cracking sequence is as follows:

1. during loading, Palmqvist cracks (1B) and (1C) and a half-penny crack (2A) initiate in the immediate vicinity of the corners of the indenter. The intersection of the half-penny crack (2A) with the indented surface is aligned with the $[110]$ direction while Palmqvist cracks (1B) and (1C) are almost aligned with the edges of the indenter;
2. a second set of half-penny cracks (2B) initiate later in the middle of the faces at the intersection of slip bands (3). At the surface, these cracks follow a $[1\bar{1}0]$ direction and they extend in the (110) plane perpendicular to the indented surface;
3. depending on the maximum load used, shallow lateral cracks extend to the surface during loading or upon unloading. The intersection of lateral cracks with Palmqvist cracks (1B) and (1C) forms a chip (4).

When the maximal load is around 500 mN, as in the experiment presented in Figure 4.25, chipping-out occurs during the loading phase. Experiments performed with lower maximal loads (around 100 mN) do not exhibit the same behaviour. In fact, in the latter case, chipping-out is only observed during the unloading portion of the cycle.

Figure 4.26 represents two cross-sections of cube corner indents made at 50 mN. A schematic showing the indenter orientation and the position of the cleavage plane is given in the insets. In Figure 4.26 a), the $(1\bar{1}0)$ cleavage plane goes through the middle of the indentation. The half-penny crack (2A) propagates in the $(1\bar{1}0)$ plane and has been highlighted by a dashed curve. The

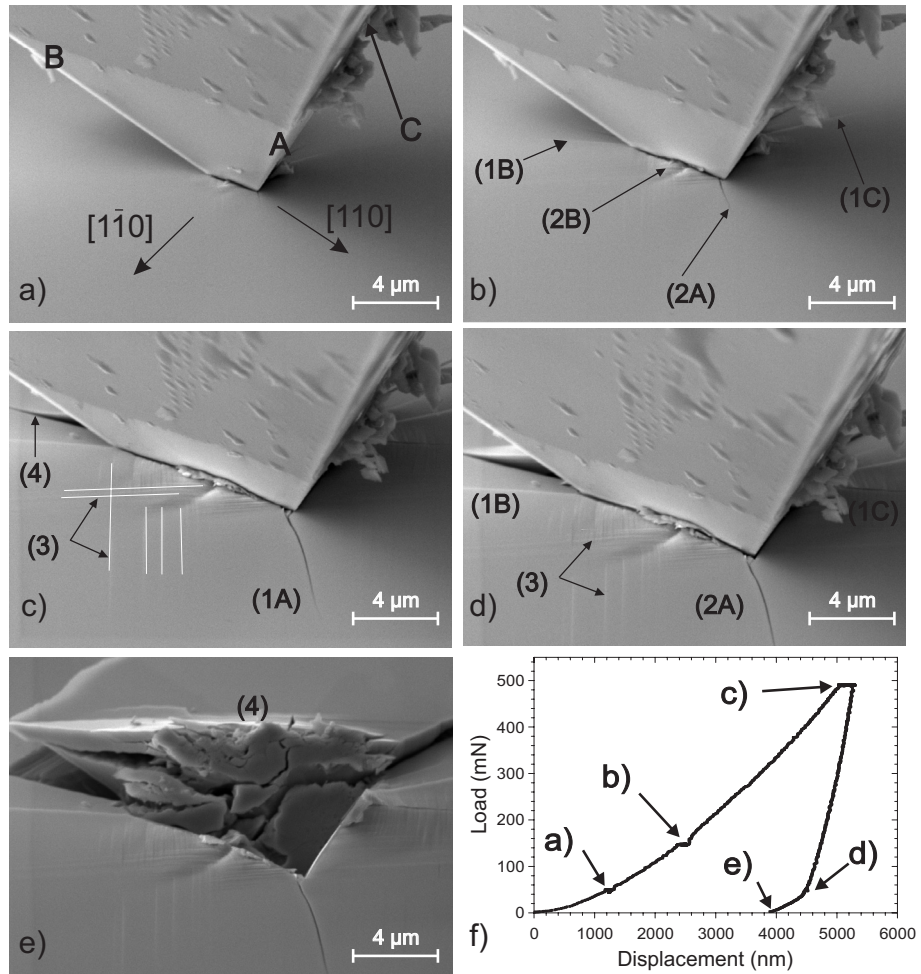


Figure 4.25: Cracking sequence under a cube corner indentation. The edge A is aligned with the $[110]$ direction. a) first hold (50 mN), b) second hold (150 mN), c) full load (500 mN), d) full unload, e) indenter withdrawn and f) the corresponding load-displacement curve.

intersection of half-penny crack (2B) with the cleavage plane is highlighted by a dashed line.

Shallow lateral cracks have emerged at the surface and their intersections with Palmqvist cracks of set (1B) and (1C) have created chips which are responsible for the large material removal near arrow (1C). Two lateral cracks (5) (highlighted by dotted lines) are also visible at the apex of the indentation.

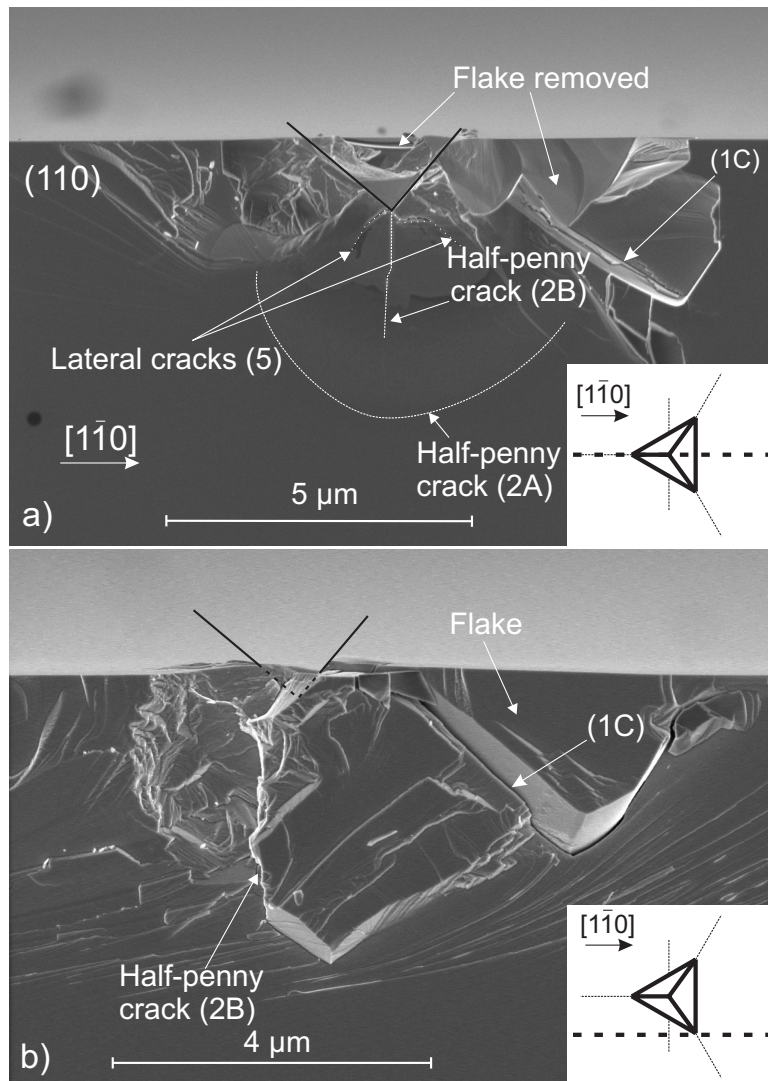


Figure 4.26: Indentations made with a cube corner indenter at 50 mN: a) cleavage plane goes through the indentation and b) cleavage plane outside the residual imprint

In Figure 4.26 b), the cleavage plane is shifted with respect to the indentation as indicated by the inset. This micrograph illustrates the fact that Palmqvist cracks (1B) and (1C) initiate at the corners of the imprint and propagate in a $\{110\}$ family of planes inclined at 45° with the indented surface. It is also clear

from this picture that the merging of Palmqvist and lateral or shallow lateral cracks is the major mechanism of chip formation.

As for conical indenters, cracks initiating along directions different from $[110]$ and $[\bar{1}\bar{1}0]$ extend in planes inclined to the surface. In contrast, cracks initiating along $[110]$ or $[\bar{1}\bar{1}0]$ are generally perpendicular to the surface. Chipping-out takes place at quite low loads and becomes rapidly important as the maximal load is increased. Chips always form first along the face opposite the edge aligned with $[110]$ (or $[\bar{1}\bar{1}0]$).

4.3.1.4 Vickers Indenter

Due to its very large included angle (136°) which prevents direct observations, in-situ SEM indentations have not been performed with the Vickers indenter. Hence, all experiments presented here are performed only with the Nanoindenter XP. The Vickers geometry with its fourfold symmetry allows to test another configuration of pyramidal indenter with obtuse included angle. Furthermore, the results obtained with this indenter are easily comparable with the extensive data from numerous articles on indentation cracking.

Two types of experiments are performed with the edges of the indenter aligned either with the $\langle 100 \rangle$ or the $\langle 110 \rangle$ directions. In the first configuration, edges of the indenter are not aligned with preferential cleavage planes whereas in the second one, they are. The comparison of the two configurations allows us to determine the role of the crystal asymmetry on the cracking process.

Figure 4.27 illustrates the case where the edges of the indenter are aligned with the $\langle 100 \rangle$ directions. The applied indentation load in this case is 250 mN.

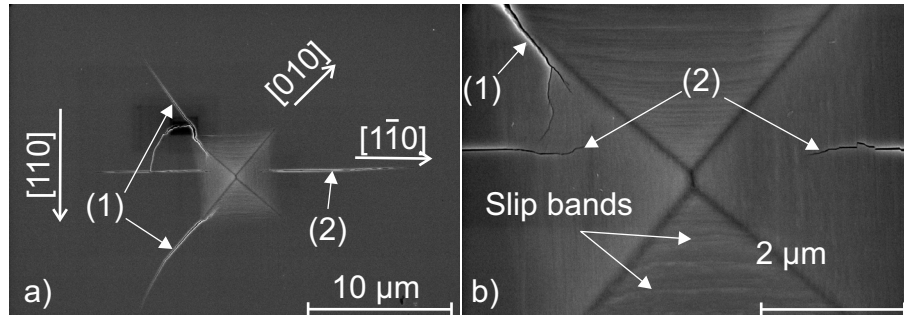


Figure 4.27: SEM micrograph of a 250 mN Vickers indentation with the edge of the indenter aligned with $\langle 100 \rangle$ directions. a) overview of the indentation showing half-penny crack (2) propagating along $[\bar{1}\bar{1}0]$ and Palmqvist cracks (1) propagating along $\langle 100 \rangle$ directions, b) close-up on the imprint showing slip bands and cracks nucleation sites.

As seen in Figure 4.27 a), Palmqvist cracks (1) intersect the surface along $\langle 100 \rangle$ directions and the nucleation sites of these cracks are in the near vicinity of the edges and at the intersection of slip planes. Cross-sectioning of indentations reveals that they propagate in $\{110\}$ planes inclined at 45° with the indented face. A well developed crack (2) intersects the surface along the $[\bar{1}\bar{1}0]$ direction while no intersection of cracks with the indented face is visible in the orthogonal direction ($[110]$). The observation of cross-sections shows that cracks

(2) are of half-penny type and propagates in the $(\bar{1}\bar{1}0)$ plane orthogonal to the indented surface.

Micrograph 4.27 b) is a magnified view of the residual imprint showing the traces of slip bands located inside. These traces are aligned with the sides of the indenter and are traces of $\{111\}$ slip planes. Some steps are visible on the edges of the half-penny crack (2) as they cross slip lines. It is also clearly visible on this micrograph that the half-penny crack (2) does not break through the whole residual imprint.

Figure 4.28 focuses on the typical crack field found when indentations are performed with the edges aligned with the $\langle 110 \rangle$ directions.

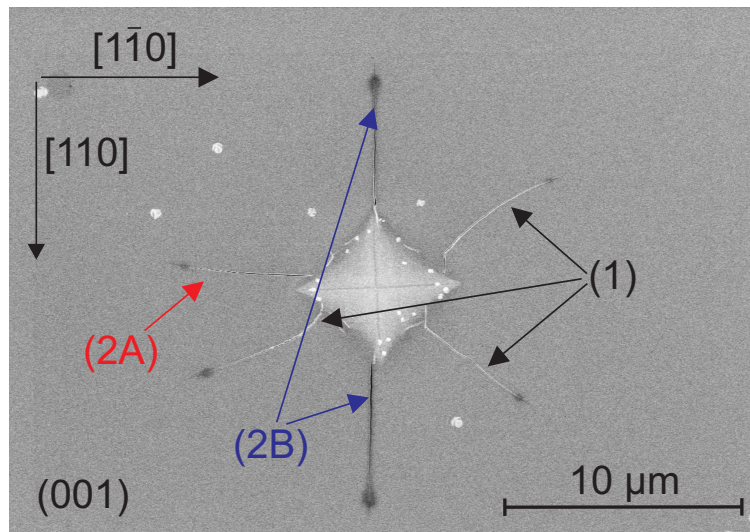


Figure 4.28: SEM micrograph of a 250 mN Vickers indentation with the edges of the indenter aligned with the $\langle 110 \rangle$ directions. Palmqvist cracks nucleate from the sides of the imprint in the vicinity of the corners.

Surprisingly, in this configuration, the preferential sites for crack nucleation are located in the middle of the faces. Here, the term "preferential site for crack nucleation" refers to the probability to observe a crack occurrence at this location. This notion is analysed in more details in Section 4.3.2.2. Thus, cracks (1) intersect the indented surface along the $\langle 100 \rangle$ directions. Subsequent observation of cross-sections shows that they are Palmqvist cracks propagating in $\{110\}$ planes inclined at 45° with the surface. Traces of the intersection of half-penny cracks (2A) and (2B) are visible along $\langle 110 \rangle$ directions aligned with the edges of the indenter.

The cross-sectional view (cleavage plane (110)) of a Vickers indentation is presented in Figure 4.29. The inset is a tilted view of the indentation showing the cleavage plane and the indented surface.

In this figure, we see that the (110) crack (2A) contained in the cleavage plane exhibits the half-penny geometry. Part of the half-penny crack front is not visible due to the deviation of the cleavage plane in the central zone beneath the indenter. On the left side of the figure, a second crack front is underlined with a yellow line. This crack front exactly corresponds to the definition of the

radial system⁵ described by Lawn *et al.* [1]. We also observe that the $(\bar{1}\bar{1}0)$ crack (labelled (2B)) intersects the cleavage plane. It is worth noting that this crack is not visible at the indented surface (see inset) but intersects the cleaved surface. These latter observations suggest that the two possible mechanisms of half-penny crack formation depicted by Cook and Pharr [18] can take place under the Vickers indentation of GaAs.

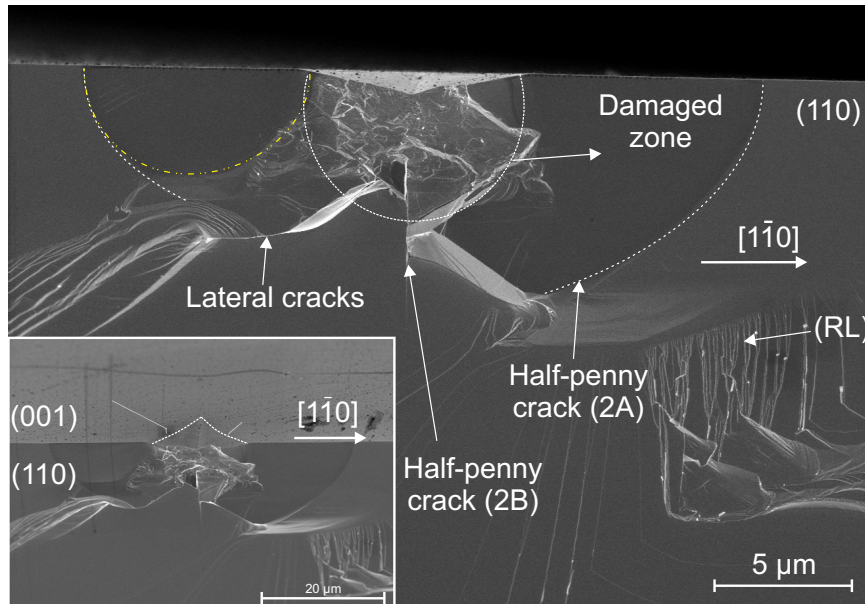


Figure 4.29: SEM Micrograph of the cross-section of a Vickers indentation showing the subsurface crack field. The inset in the bottom left corner is a tilted view of the same indentation that shows the position of the cleavage plane with respect to the imprint.

4.3.1.5 Summary

The different cracking patterns that have been encountered for the various indenter geometries are summarised in Figure 4.30. The typical crack fields found around a) a wedge, b) a cube corner, c) a Vickers and d) conical indenters are contrasted. In the schematic views, bold lines represent the residual impression, thin black lines represent half-penny cracks propagating in $\{110\}$ planes perpendicular to the surface, red lines represent Palmqvist cracks and thin black lines represent the different configurations of chips that have been observed.

Palmqvist cracks, are characterised by their intersection with the indented surface along $\langle 100 \rangle$ directions. These cracks propagate mainly in a family of $\{110\}$ planes inclined at 45° to the surface. Material removal by the chipping process is mainly due to the intersection of these cracks with either shallow or deep lateral cracks.

⁵In the literature, radial cracks are shallow semi-elliptical cracks that extend near the corner of the indenter (see Cook and Pharr [18] for details)

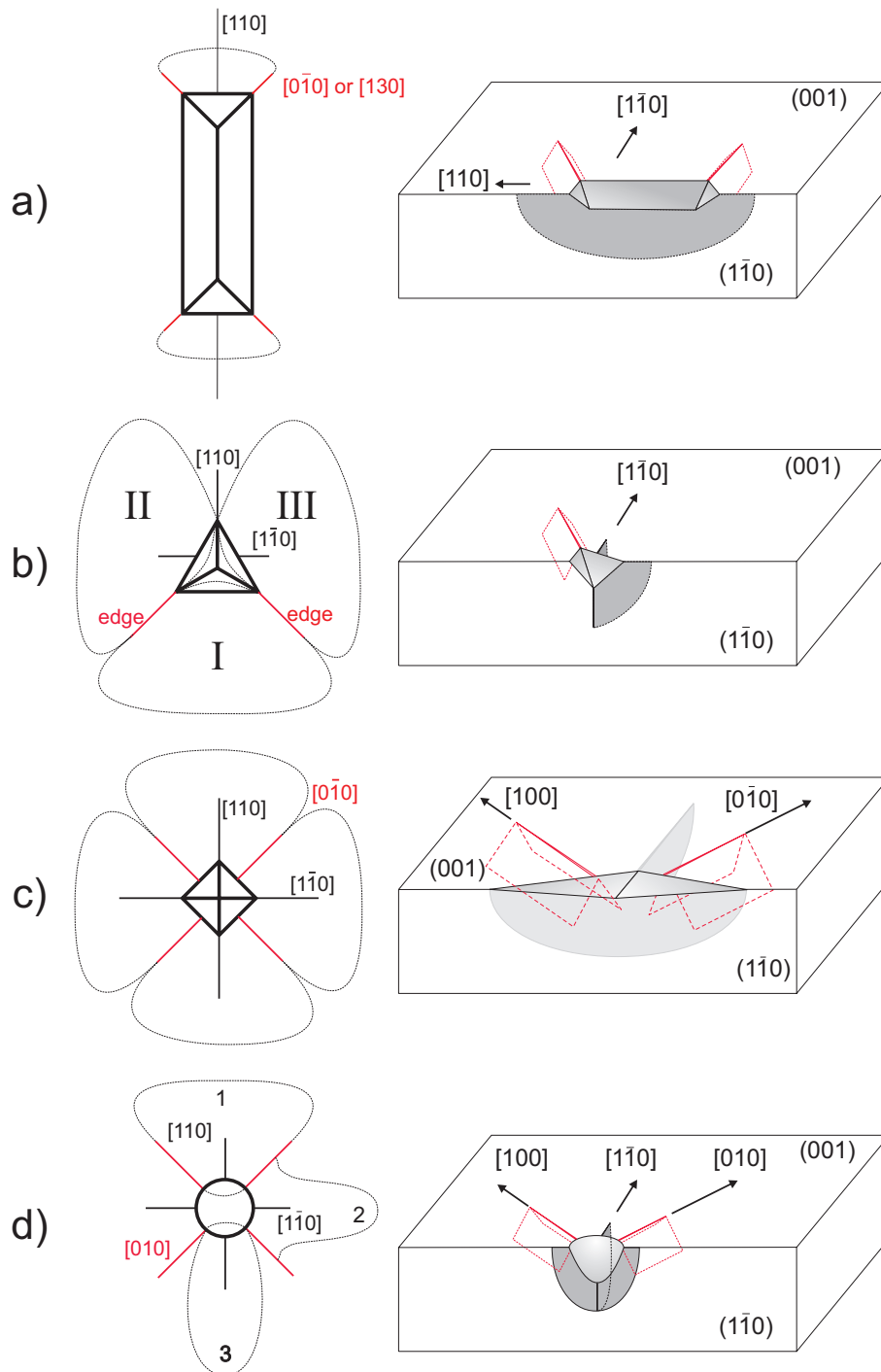


Figure 4.30: Schematic views of the cracking patterns found under a) wedge , b) cube corner, c) Vickers and d) conical indenters.

4.3.2 Discussion

We have seen in the discussion of Section 4.2.2.3 that the extremities of the wedge are preferential sites for chipping-out. It is therefore necessary to determine the best "end geometry" that will minimise the end-effects responsible for chip formation and promote the propagation of the half-penny crack.

In the following discussion, we will first focus on features that are visible in the load-displacement curves of indentations performed with point indenters. Then effects of the indenter geometry on Palmqvist cracks extension as well as on the chipping pattern is then analysed. In a third step, we will turn our attention to the effect of the indenter geometry on $\langle 110 \rangle$ cracks (half-penny) propagation. From the elements given in the discussion, we will be able to determine the shape that will best address the problem of wedge termination to minimise chip formation.

4.3.2.1 Load-Displacement Curves

Plateaus are visible on the load-displacement curves of all indenters, and the source of these plateaus is twofolds:

1. a displacement when the load is held constant for a certain time (typically to take an SEM picture or at the end of the loading cycle);
2. a sudden displacement due to material removal (chips spreading out at the surface).

In the first case, the nature of the plateau is easily determined by careful examination of the time-displacement curve as illustrated in Figure 4.31 a). This curve is extracted from the experimental data of an in-situ SEM indentation made with the conical 60° indenter (also presented in Section 4.3.1.1). Arrows labelled (1) point to time intervals where the load is kept constant during approximately 60 seconds, whereas the arrow (2) points to the chipping-out event shown in Figure 4.19.

In some experiments, we have noted that as the loading time is increased, the displacement rate decreases. In other words, if the load is held constant for 15 seconds we have a displacement rate of about 10 nm/s whereas if the load is held constant for 500 seconds, the displacement rate tends to the values of electronic drift of the apparatus (approximately 0.2 nm/s in the case of the Nanoindenter XP). The examination of the plot in Figure 4.31 b) shows that most of the displacement occurs in the first twenty seconds where the load is kept constant.

Two possible phenomena might be at the origin of this time dependent behaviour. Creep is the first phenomenon. It has already been observed for GaAs by Syed-Asif and Pethica [19]. In their study, they have demonstrated that creep takes place as soon as dislocations are created. As a large amount of dislocations is generated in our indentation experiments (see Chapter 5 for details), creep could be responsible of this time dependent behaviour.

The second phenomenon that could be at the origin of the plateau is slow crack growth. Slow crack growth is a well known effect in the case of Vickers indentation of soda-lime glass. It has been observed by numerous authors [1, 20]

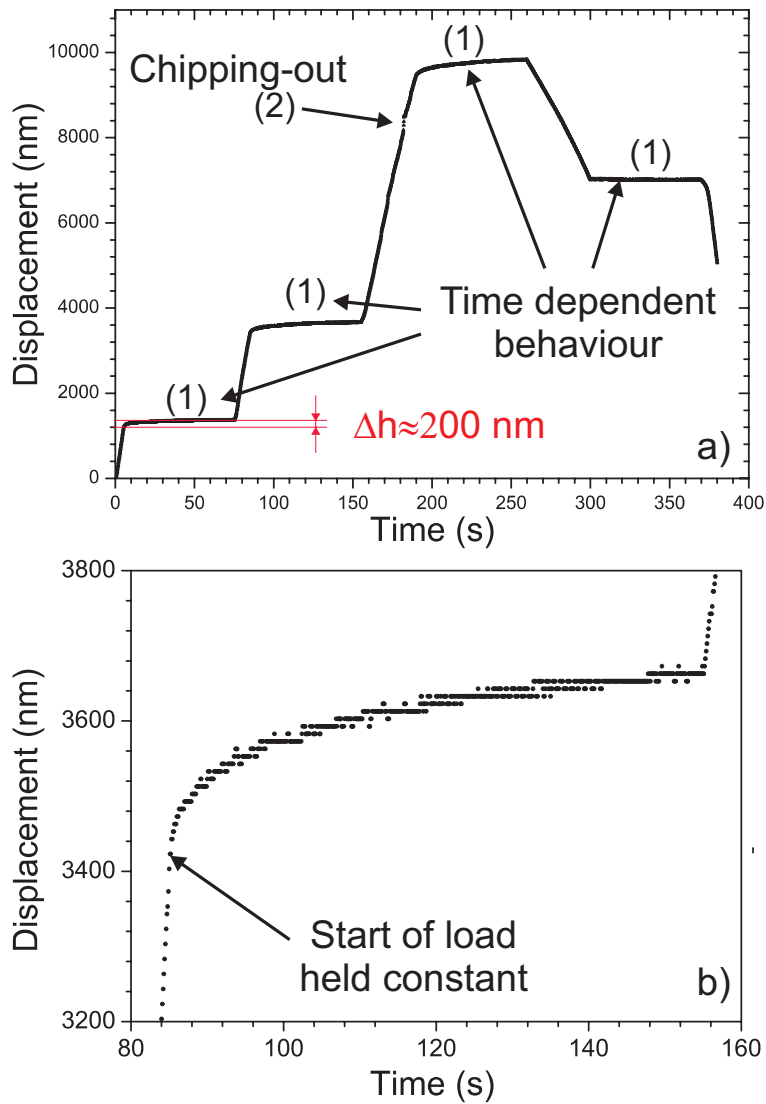


Figure 4.31: Displacement as a function of indentation time for the conical 60° experiment presented in Section 4.3.1.1. a) Arrows labelled (1) point to plateaus due to the load held constant for around 70 s, and arrow (2) points to the sudden displacement due to chips formation. The graph in b) is a detailed view of the second plateau showing that most of the displacement occurs in the first 20 seconds.

and is generally attributed to the stress corrosion of glass⁶. Environmentally assisted slow crack growth has already been observed in GaAs by White *et al.* [21].

To conclude with this point, a time dependent behaviour is defined by a time characteristic, i.e. the time necessary for the phenomenon to take place. In the case of creep and slow crack growth, these times are not known and further experimental work is needed to clarify which mechanism dominates. This was beyond the scope of this work which concentrates on crack nucleation and propagation.

In the case of chips spreading out at the surface (arrow 2 in Figure 4.31 a)), the nature of the pop-in excursion can only be determined by direct observation during the experiment. The interest of in-situ testing is thus demonstrated since it allows to precisely relate a feature of the load-displacement curve to a specific event such as crack extension, chipping-out and even formation of slip bands as already observed in the case of bulk metallic glasses [22].

4.3.2.2 Cracking Patterns Around Point Indenters

The variety of cracking patterns found under point indenters is illustrated in Figure 4.30. The crack formation around a point indentation is a reproducible phenomenon but on a statistical basis. This notion is best illustrated by the graph in Figure 4.32 which gives the probability to find a crack for a given direction around a Vickers indentation. On this graph the crack distribution is reported as a function of the crystallographic direction observed.

The method to obtain this graph is as follows:

1. 16 Vickers indentations are made with defined conditions which are: edge aligned with $\langle 110 \rangle$ directions and an applied load of 500 mN;
2. for each indentation, the crack orientations are measured;
3. for each direction the percentage of cracked specimens (in a specific direction: the number of specimens that present a crack in that direction divided by the total number of indentations) is established.

Looking at the graph, the first striking feature is that we find fewer half-penny cracks propagating along $\langle 110 \rangle$ directions (black columns) than Palmqvist cracks propagating in the $\langle 100 \rangle$ directions. Secondly, there are slightly fewer half-penny cracks that propagate along $\langle 110 \rangle$ than those that propagate along the orthogonal $\langle \bar{1}\bar{1}0 \rangle$ direction. The measurement of the length of half-penny cracks gives similar results, i.e. cracks along $\langle 110 \rangle$ are slightly shorter than cracks in the $\langle \bar{1}\bar{1}0 \rangle$ direction.

Two sets of experiments performed under similar conditions (but with two different Vickers indenters) give identical results. These results disagree with the observations of Warren *et al* [23], who reported that no cracks were present along [110] but are in line with those of Margevicius *et al* [14] who noted a different crack length depending on the $\langle 110 \rangle$ direction observed. The discrepancy of our observations with the results of Warren *et al* might be accounted for by the high temperature (350°C) at which they conducted their experiments.

⁶Stress corrosion in Soda-Lime Silica glass occurs under the combined action of residual stresses on the one hand and moisture contained in the air on the other hand.

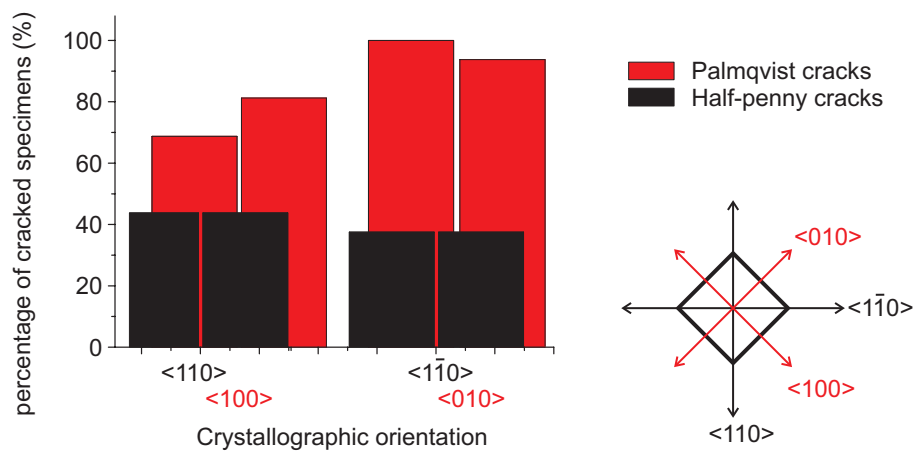


Figure 4.32: Bar graph showing the repartition of cracks as a function of the crystallographic directions (Vickers indenter). The applied load is 500 mN and edges of the indenter are aligned with $\langle 110 \rangle$ directions.

If we compare chipping patterns (see Figure 4.30), we see that under Vickers and conical indentations the crack distribution around the indent follows a fourfold symmetry. Independently of the indenter shape, chips form between the Palmqvist cracks. In the case of the Vickers indenter, the morphology of the chips is quite constant. They follow more or less the shape of a maltese cross as seen in Figure 4.30 c). In the case of conical indentation, variations in the morphology of chips exist. In fact, three different chipping patterns are found as illustrated in Figure 4.30 d). The distribution of Palmqvist cracks around cube corner indentations follows the threefold symmetry of the indenter. During cube corner indentation, we observed that chipping out occurs preferentially along the face of the indenter that is "aligned" with a $\langle 110 \rangle$ direction. This observation concerns the chip labelled I in Figure 4.30 b).

In the context of the study, it was expected that the lack of edges on conical indenters should help reducing Palmqvist cracks and chips formation. As can be seen, our expectations were not confirmed and chipping-out with conical indenters is not reduced when compared to pyramidal ones. The length of Palmqvist cracks and their number is strongly dependent on the apex angle of the indenter. At a given load level, conical 60° and cube corner (acute indenters) generate much more chips than conical 120° and Vickers indenters. With these two acute indenters, the level of damage around indentations becomes rapidly important when compared to obtuse indenters. Hence, it might be necessary to limit the apex angle of the wedge termination in order to reduce chips formation.

4.3.2.3 Prediction of Crack Growth

In experiments performed with the wedge indenter, our interest was focused on half-penny cracks since it is the more pertinent crack system for dicing applications. When we investigated point indenters, the goal was slightly different since we wanted to compare the different shapes and determine the one that promotes half-penny crack growth and, at the same time, minimises particles formation.

In this case, we have to focus on the half-penny cracks that propagate in $\langle 110 \rangle$ directions and also on Palmqvist cracks propagating along $\langle 100 \rangle$ directions.

Let us first investigate the dependence of the size of the half-penny cracks on the indentation load. In order to use the CLHPC model described in Section 2.4, we need to collect data relative to the length and depth of these cracks. However, as we have seen in the result section (Section 4.3), the cross-section surfaces under point indentations are generally damaged, and it is difficult to measure accurately crack depths. For that reason, we turn our attention to the indentation fracture model of Antsis *et al.* [24] (see Section 2.4) which gives the relation between the crack size at the surface (c) and the indentation load (P) according to:

$$c^{3/2} = \Lambda * P \quad (4.8)$$

where Λ is a constant dependent on material properties and indenter geometry.

It is worth noting that in this part of the work, only conical and Vickers indenters were investigated since the cracking patterns of these three indenters are very similar and it is therefore easier to compare them. Experimental values of crack lengths ($c^{3/2}$) for Vickers, 60° and 120° conical indenters are plotted versus the load in Figure 4.33. On this graph, Λ is the slope of the least square fit of experimental points.

Looking at the curves, we first note that independently of the direction, the linear fit of experimental data points is very good for all indenters. This is confirmed by the coefficient of regression (R^2) being greater than 0.95 which quantifies the correlation of the crack length parameter $c^{3/2}$ with the indentation load P .

Looking at the graph, it is easily seen that at a given load level and for all three indenters, the cracks that propagate in the $\langle 110 \rangle$ directions are longer than the cracks that propagate in the orthogonal $\langle 1\bar{1}0 \rangle$ direction. This is expressed by the larger coefficient Λ that is found for $\langle 110 \rangle$ cracks (~ 0.19 for Vickers and 120° conical and ~ 0.25 for 60° conical) when compared to $\langle 1\bar{1}0 \rangle$ cracks (~ 0.15 for Vickers, ~ 0.05 for 120° conical indenters and ~ 0.07 for 60° conical indenter). Recalling that the plane of a crack is orthogonal to its direction (i.e. (110) is orthogonal to $[110]$), this means that it is more difficult to propagate cracks in the (110) plane than in the $(1\bar{1}0)$ one.

This result agrees with the observations of Margevicius and Gumbsch [14], Koubaiti *et al.* [25] and Yasutake *et al.* [26]. In particular, Margevicius and Gumbsch, which estimated K_c by measuring the lengths of cracks stemming from Vickers indentations, found that the fracture toughness of $\{110\}$ planes ($K_c = 0.98 \text{ MPa}\sqrt{m}$) was nearly twice larger than the one of $\{1\bar{1}0\}$ planes ($K_c = 0.53 \text{ MPa}\sqrt{m}$).

The comparison of conical indenters on the one hand, and the Vickers indenter on the other hand shows that (110) cracks are much more easier to propagate with the pyramidal Vickers indenter than with conical indenters. Namely, there is only a slight difference between $\Lambda_{\langle 1\bar{1}0 \rangle}$ and $\Lambda_{\langle 110 \rangle}$ for the Vickers indenter while there is nearly a factor three between $\Lambda_{\langle 1\bar{1}0 \rangle}$ and $\Lambda_{\langle 110 \rangle}$ for conical indenters. This latter result suggests that the edges of the Vickers indenters induce stress concentrations that allow to compensate for the different toughness of $\{110\}$ and $\{1\bar{1}0\}$ planes. In contrast, in the case of conical indenters where the geometrical defects of the nominally conical surface are not sufficiently sharp to

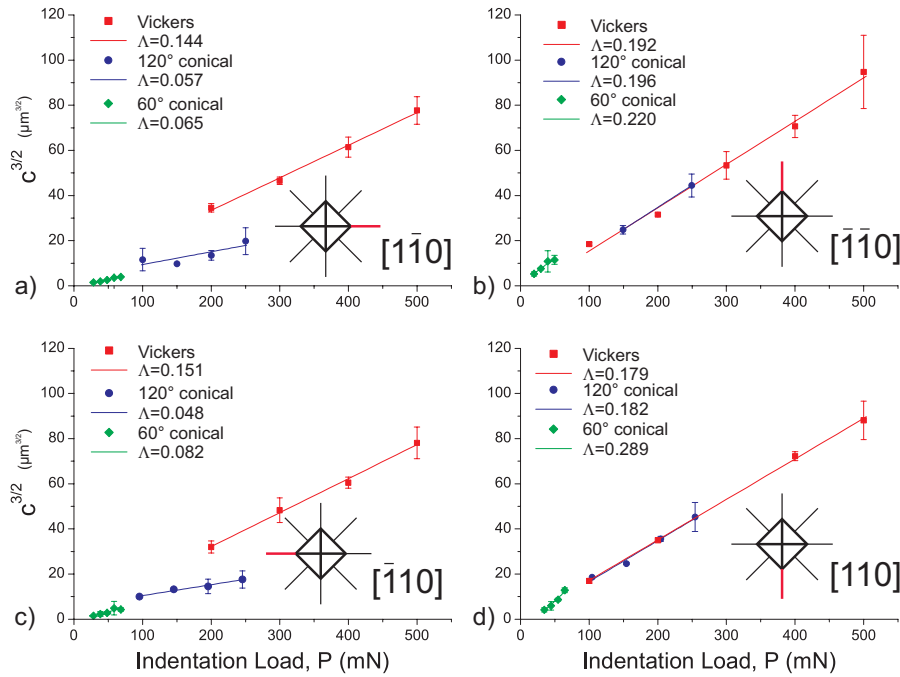


Figure 4.33: Evolution of the crack size $c^{3/2}$ with the indentation load for Vickers, 60° conical and 120° conical indenters. a) cracks aligned with $[1\bar{1}0]$, b) cracks aligned with $[\bar{1}\bar{1}0]$, c) cracks aligned with $[\bar{1}10]$, d) cracks aligned with $[110]$.

act as stress concentrators, $\{110\}$ cracks are much more difficult to propagate. Thus, the comparison of conical and pyramidal indenters is of high interest since it shows that the presence of edges is a critical parameter that helps promoting half-penny cracks.

The investigation of Palmqvist cracks ($\langle 100 \rangle$ directions) is of interest since this system is related to the formation of chips during unloading. For the four $\langle 100 \rangle$ directions, the results are shown in Figure 4.34 which compares the evolution of cracks sizes with the indentation load for Vickers, 60° and 120° conical indenters.

In the semi-empirical indentation fracture models the $P \propto c^{3/2}$ relation holds only if limited chipping-out takes place during indentations. For Vickers indentations, observations correlate the change in the rate of crack growth (here the rate of crack growth is defined as $\Delta c / \Delta P$) above 300 mN with the higher tendency for chipping-out that occurs above this load. That is the reason why the fit of experimental data points is only made for loads lower than 300 mN. In that case, R^2 becomes larger than 0.90 and the predictions from the model are fairly good. In the case of conical indenters, the chipping-out tendency is less marked in the load ranges investigated (10 to 60 mN for 60° conical indenter and 100-250 mN for the 120° conical indenter) and this observation explains the excellent correlation between P and $c^{3/2}$ ($R^2 \sim 0.99$).

For a given load level, the crack extension for the 60° conical indenter will be larger than for the 120° conical and Vickers indenters. Generally speaking, the asymmetry of Palmqvist cracks is less pronounced than the asymmetry of

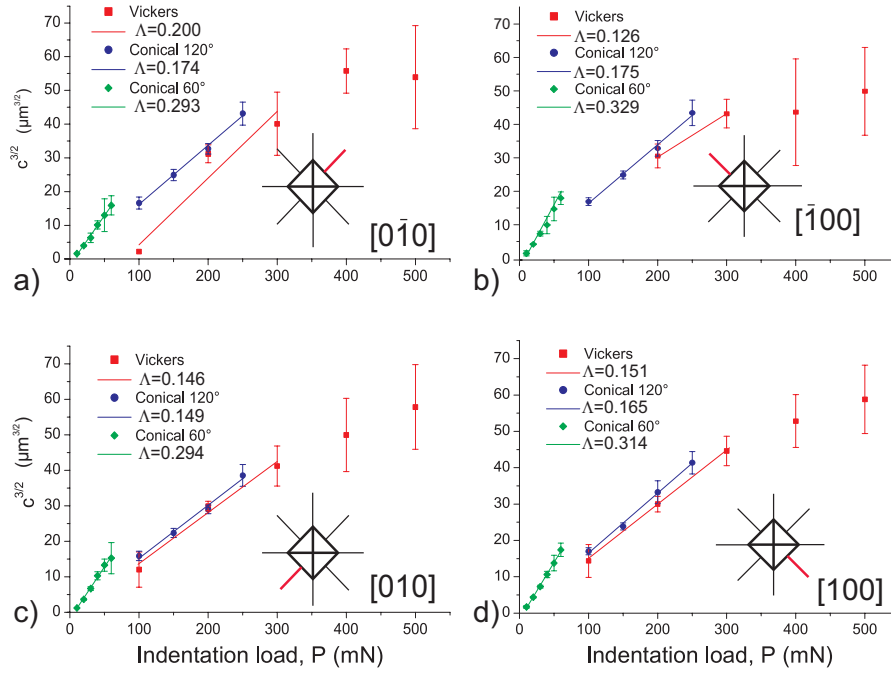


Figure 4.34: Evolution of the crack size $c^{3/2}$ with the indentation load for Vickers, 60° conical and 120° conical indenters. a) cracks aligned with $[0\bar{1}0]$, b) cracks aligned with $[\bar{1}00]$, c) cracks aligned with $[010]$, d) cracks aligned with $[100]$.

half-penny ones. Indeed, the coefficient Λ is quite independent of the observed $\langle 100 \rangle$ direction that is observed.

Table 4.1 summarises the values of the Λ coefficients relative to the different crack systems for each of the investigated indenters. The ratios $\Lambda_{[110]}/\Lambda_{\langle 100 \rangle}$ and $\Lambda_{[1\bar{1}0]}/\Lambda_{\langle 100 \rangle}$ reported in the two columns on the right side of the table are used as indicators of the "efficiency" of the indenter for the dicing process. A high ratio means that for a given load, Palmqvist cracks that propagate along $\langle 100 \rangle$ directions (unsuitable for dicing), will be less developed than half-penny cracks that propagate along the $\langle 110 \rangle$ directions. The higher the ratio is, the more suitable the indenter shape for dicing is. Therefore, from the table, we see that obtuse indenters (Vickers and 120° conical) obtain the best results. Namely, at a given load level, Palmqvist crack extension is much more limited under such indenters when compared to acute indenters. In addition, we see that it is preferable to use the pyramidal shape rather than the conical one, since the stress concentration that takes place at the edges of a pyramidal indenter enhances the formation of half-penny cracks along the $\langle 1\bar{1}0 \rangle$ directions.

Some experiments conducted with conical indenters have shown that when the loading rate is decreased, the formation of chips can be reduced. It is also important to note that when acute point indenters are used (60° conical and cube corner for instance) the indentation load must be kept relatively low (\sim less than 100 mN) in order to avoid large damage. This latter observation is of critical importance in the dicing process since low indentation rate can help prevent chip extension during the process.

	$\Lambda_{[110]}$	$\Lambda_{[\bar{1}\bar{1}0]}$	$\Lambda_{\langle 100 \rangle}$	$\Lambda_{[110]}/\Lambda_{\langle 100 \rangle}$	$\Lambda_{[\bar{1}\bar{1}0]}/\Lambda_{\langle 100 \rangle}$
Vickers	0.184	0.147	0.155	1.187	0.943
120° conical	0.189	0.052	0.165	1.145	0.315
60° conical	0.254	0.073	0.307	0.827	0.237

Table 4.1: Coefficients Λ for the different crack systems.

4.4 Conclusions

The effect of the different parameters that have been investigated during this work are summarised in Table 4.2.

In this chapter, it has been shown that acute wedge indenters enhance the formation and the propagation of a well-defined half-penny crack aligned with the main edge of the indenter. The extension of the half-penny crack with the indentation load can be estimated accurately with the help of the experimentally calibrated Center Loaded Half-Penny Crack (CLHPC) model. The fracture toughness values determined with this model were in the range of values usually found in the literature.

In-situ experiments have demonstrated that, during wedge indentations, the nucleation of the half-penny crack is correlated to the pop-in excursion in the load-displacement history. The load at which the half-penny crack initiates is affected by both indenter radius and loading rate. In other words, the pop-in load decreases with decreasing indenter radius and with increasing loading rate. Simulations of indentations in a homogeneous elasto-plastic solid indicate that when the radius of the edge of the wedge indenter is increased, the maximum value of the tensile stress present below the wedge indenter strongly decreases. We have also provided evidence that the effect of the loading rate on the half-penny crack initiation can be explained by the influence of the strain rate on the yield stress that in turn influences the global stress field below the indenter.

A slope change in the unloading part of the load-displacement curve also indicates that the half-penny crack has formed. The origin of the hysteresis effect in the unloading-reloading sequence is not yet well understood. The energetic analysis of the load-displacement curve allows us to estimate the cleavage surface energy of GaAs. In the present case, the value of the cleavage energy ($1.03J/m^2$) is close to the values determined by previous authors ($0.89J/m^2$).

The pop-in as well as the the slope change are two interesting features in the context of dicing applications. During the dicing process, it is of critical importance to ensure that a half-penny crack has formed. In that view, the pop-in and the slope change are simple ways to know whether the half-penny crack has nucleated or not. In addition, by following the evolution of the pop-in load, we have a convenient way to monitor the wear of the indenter. Indeed, the wear of indenters generally leads to an increase of the indenter radius, and we have shown that this results in an increase of the load at which pop-in occurs.

Different indenter geometries have been tested to determine the best suited shape to terminate the wedge indenter. For all tested indenters (Vickers, cube corner, conical), half-penny cracks are aligned with $\langle 110 \rangle$ directions and prop-

Parameter	Effect when the parameter is increased (not valid for the shape)
Angle (α)	<ul style="list-style-type: none"> - Initiation load of the half-penny crack increases (wedge) - Smaller extension of the half-penny crack at a given indentation load - Palmqvist cracks occurrences and lengths are decreased
Radius (R)	<ul style="list-style-type: none"> - Maximum tensile stress decreases - Pop-in load increases (wedge) - No modification of the final half-penny size ($R < 1\mu m$)
Shape	<ul style="list-style-type: none"> - Formation of a well defined half-penny crack with the wedge indenter - Strong asymmetry of cracking patterns with conical indenters - Threefold symmetry of cracking patterns for cube corner indenter - Twofold symmetry for Vickers and conical indenters
P \dot{P} ($\dot{\epsilon}$)	<ul style="list-style-type: none"> - Size of all crack systems increases - $P \propto c^{3/2}$ (point indenters) - $K_c c^{3/2} = f_i \left(\frac{a}{c}\right) F_T$ (wedge indenter) - Increase of the upper yield stress (τ_{uy}) - Pop-in load is decreased (wedge) - Number of lateral cracks is increased - Chips can form during the loading sequence (acute point indenters)

Table 4.2: Summary of the results obtained in Chapter 4 about crack morphologies.

agate in $\{110\}$ planes orthogonal to the indented surface. Palmqvist cracks developing along $\langle 100 \rangle$ directions are generally inclined to the surface and follow a star-like pattern at the surface.

We have seen that under point indenters, the evolution of the crack lengths with the applied indentation load follows the $P \propto c^{3/2}$ relationship for both $\langle 110 \rangle$ and $\langle 100 \rangle$ cracks. However, our observations indicate that the range of load to be investigated must be carefully chosen in order to avoid pronounced chipping-out which are not taken into account in this model.

Concerning half-penny cracks that propagate in $\{110\}$ planes, the asymmetric cracking behaviour of GaAs already reported in the literature has been confirmed. The comparison of conical indenters with a Vickers indenter (pyramidal), has shown that the lack of edge enlarges this asymmetric cracking behaviour. By comparing the propagation of both $\langle 110 \rangle$ cracks (suitable for crack precursor creation) and $\langle 100 \rangle$ cracks (responsible for chips formation), we have seen that obtuse apex angles are more adapted to terminate the wedge as they limit Palmqvist crack extension more efficiently than acute ones. Furthermore, it is possible to take advantage of the particular shape of the cube corner indenter to terminate the wedge. Namely, the threefold symmetry of this indenter limits the number of Palmqvist occurrences and hence the possibilities of chips formation. As we can see in Figure 4.35, two different configurations of the cube corner indenter could be employed to terminate a wedge. The first configuration is already employed on the wedge indenters used during this study. In this case, chips form generally within the limit of Palmqvist cracks, in the continuity of the wedge. The second one, similar to the bow of a ship, should help promoting the extension of the half-penny crack. In this latter case, the special cracking behaviour observed in cube corner indentations has two advantages. Firstly, the edge of the cube corner shape is in the alignment of the main edge of the wedge and this will help to promote the propagation of the half-penny crack. Secondly, chips II and III generally spread-out more rarely than chip I (see Figure 4.30 b)) and this might help to reduce chipping-out.

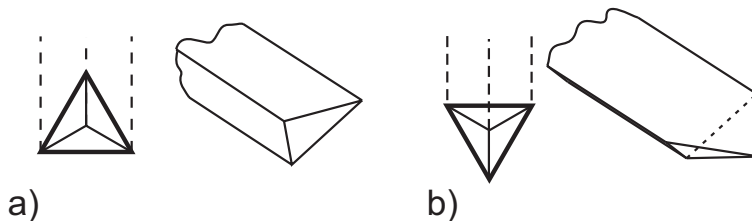


Figure 4.35: a) face first configuration for the cube corner tip and b) edge first configuration.

The edge first configuration combined with a rather large apex angle should be an appropriate solution for dicing operations of GaAs. However, this has to be verified by further experimental work combined with FE simulations.

In the next chapters, we will investigate other aspects related to the indentation cracking in GaAs. The purpose of Chapter 5 is to clarify the interactions that exist between the deformation mechanisms and the formation of cracks and particularly the mechanisms that concern the half-penny crack formation. In

Chapter 6, we will study a practical case where the wedge indentation is used to separate commercial laser structures.

Bibliography

- [1] B.R. Lawn, A.G. Evans, and D.B. Marshall. Elastic/plastic indentation damage in ceramics: the median/radial crack system. *Jour. Amer. Ceram. Soc.*, 63(9-10):574–581, 1980.
- [2] S. Fujita, K. Maeda, and S. Hyodo. Dislocation mobility-controlled cracking in GaAs caused by constant-rate indentation. *Philosophical Magazine A*, 65(1):131–147, 1992.
- [3] K. Maeda, H. Nishioka, N. Narita, and S. Fujita. Brittle-to-ductile transition studied by constant-rate indentation cracking. *Materials Science and Engineering*, A176:121–126, 1994.
- [4] I. Yonenaga and K. Sumino. Mechanical properties and dislocations dynamics of III-V compound semiconductors. *Physic State Solid A*, 131:663–672, 1992.
- [5] E.A. Stach, T. Freeman, A.M. Minor, D.K Owen, J. Cumings, M.A. Wall, T. Chraska, R. Hull, Jr Morris, J.W., A. Zettl, and U. Dahmen. Development of a nanoindenter for in-situ transmission microscopy. *Microscopy and Microanalysis*, 7:507–517, 2001.
- [6] C. Messmer and J.C. Bilello. The surface energy of Si, GaAs and GaP. *Journal of Applied Physics*, 52(7):4623–4629, 1981.
- [7] K. Wasmer, C. Ballif, R. Gassilloud, C. Pouvreau, R. Rabe, J. Michler, J.-M. Breguet, J.-M. Solletti, A. Karimi, and D. Schulz. Cleavage fracture of brittle semiconductors from the nanometer to the centimeter scale. *Advanced Engineering Materials*, 7:309–317, 2005.
- [8] K. Wasmer, C. Ballif, C. Pouvreau, D. Schulz, and J. Michler. Dicing of gallium-arsenide high performance laser diodes for industrial applications: Part i: Scratching operation. *J. Mater. Process. Tech.*, 2007.
- [9] K. Wasmer, C. Ballif, C. Pouvreau, D. Schulz, and J. Michler. Dicing of gallium-arsenide high performance laser diodes for industrial applications: Part ii: Cleavage operation. *J. Mater. Process. Tech.*, 2007.
- [10] T. Fett and D. Munz. *Stress Intensity Factors and Weight Functions*. Advances in Fracture series. Southampton UK, 1997.
- [11] I.S. Raju and J.C. Jr Newman. Stress intensity factors for a wide range of semi-elliptical surface cracks in finite thickness plates. *Engineering Fracture Mechanics*, 11:817–829, 1979.
- [12] J.C. Jr Newman and I.S. Raju. An empirical stress intensity factor equation for the surface crack. *Engineering Fracture Mechanics*, 15(1-2):185–192, 1981.
- [13] G. Michot and A. and George. Fracture toughness of pure and In doped GaAs. *Scripta Metallurgica*, 22:1043–1048, 1988.

- [14] R. W. Margevicius and P. Gumbsch. Influence of crack propagation direction on $\{110\}$ fracture toughness of gallium arsenide. *Philosophical Magazine A*, 78:567–581, 1998.
- [15] D. Hull. Interpretation of river lines patterns on indentation generated fracture surfaces and comments on the fractal characteristics described by djordevic et al. *Journal of Materials Science Letters*, 15:651–653, 1996.
- [16] D. Hull. The effect of mixed mode i/iii on crack evolution in brittle solids. *International Journal of Fracture*, 70(1):59–79, 1994.
- [17] Wasmer K., C. Ballif, C. Pouvreau, and J.-M. Solletti. Project n° 6025.2 final report. Technical report, CTI, March 2005. CTI internal report.
- [18] R. F. Cook and G. M. Pharr. Direct observation and analysis of indentation cracking in glasses and ceramics. *J. Am. Ceram. Soc.*, 73(4):787–817, 1990.
- [19] S.A Syed Asif and J. B. Pethica. Nanoindentation creep of single-crystal tungsten and gallium arsenide. *Philosophical Magazine A*, 76(6):1105–1118, 1997.
- [20] J. Salomonson, Z. Kaiyang, and D. Rowcliffe. Decay of residual stress at indentation cracks during slow crack growth in soda-lime glass. *Acta Materialia*, 44:543–546, 1996.
- [21] G.S. White, S.W. Freiman, and A.M. Wilson. Indentation determination of crack growth parameters in gallium arsenide. *Journal of the American Ceramic Society*, 74(2):419–421, 1991.
- [22] B. Moser, J. Kuebler, H. Meinhard, W. Muster, and J. Michler. Observation of instabilities during plastic deformation by in-situ sem indentation experiments. *Advanced Engineering Materials*, 7(5):388–391, 2005.
- [23] P.D Warren, P. Pirouz, and S.G. Roberts. Simultaneous observation of α and β -dislocation movement and their effect on the fracture behaviour of GaAs. *Philosophical Magazine A*, 50(5):23–28, 1984.
- [24] G.R Antsis, P. Chantikul, B.R. Lawn, and D. B. Marshall. A critical evaluation of indentation techniques for measuring fracture toughness: I, direct crack length measurements. *Jour. Amer. Ceram. Soc.*, 64(9):533–538, 1981.
- [25] S. Koubaiti, C. Levade, and G. Vanderschaeve. Vickers indentation on the $\{001\}$ GaAs under illumination and in darkness. *Philosophical Magazine A*, 80:83–104, 2000.
- [26] K. Yasutake, Y. Konishi, K. Adachi, K. Yosh, M. Umeno, and H. Kawabe. Fracture of GaAs wafers. *Japanese Journal of Applied Physics*, 27:2238, 1988.

Chapter 5

Deformation Mechanisms and Crack Initiation

5.1 Introduction

In the previous chapter, we have turned our attention to the morphology of crack fields around indentations and also to several parameters that influence crack propagation. In the course of Chapter 4, we have also dealt with some aspects of deformation of GaAs and the initiation of cracks.

The purpose of the present chapter is to understand the interaction between the plastic deformation mechanisms and the initiation of the different crack systems. The results section is divided in two parts. In the first part, the case of the wedge indenter and more specifically the mechanism of half-penny crack nucleation is treated with the help of cathodoluminescence and transmission electron microscopy (TEM). The second part, dedicated to point indenters, presents surface observations of residual imprints. This second part is mostly based on surface observations with both High Resolution SEM (HRSEM) and Atomic Force Microscopy (AFM).

5.2 Results

5.2.1 The Case of Wedge Indenters

Two distinct parameters having a particular influence on crack initiation have been identified. Firstly, the predominant role of the indenter apex angle in the cracking process was identified during the first phase of experimental observations. Secondly, the effect of crystal orientation on crack formation and the possible interaction with the dislocation structure was reported by several authors in the literature review (see Section 2.2 for details). Therefore, the results presented in this section are divided into two subsections addressing these two aspects.

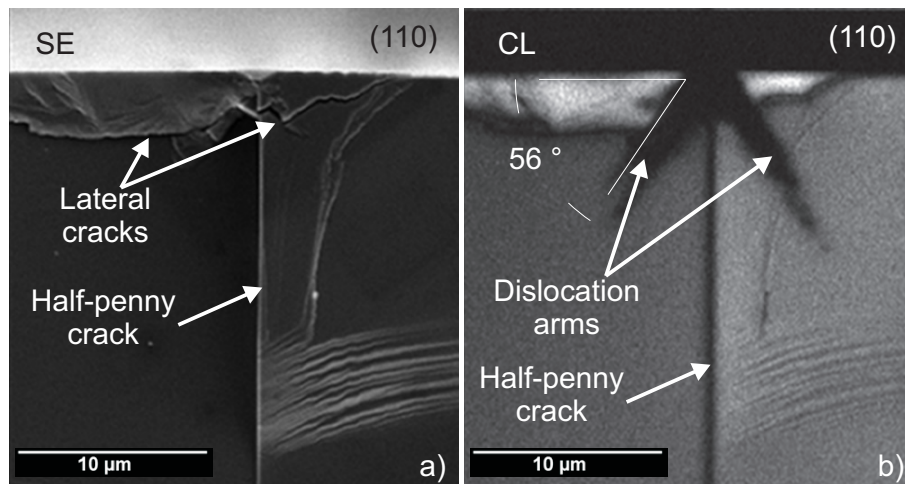


Figure 5.1: SEM micrographs of a 60° wedge indentation. a) SE mode showing lateral and half-penny cracks, b) CL mode showing both cracks and dislocation arms extending on each side of the half-penny crack.

5.2.1.1 Effect of the Apex Angle

The cathodoluminescence mode (CL) of the SEM allows us to gather information that are different from the Secondary Electron (SE) mode. Figure 5.1 illustrates this difference. In the SE image in Figure 5.1 a), we clearly identify lateral and half-penny cracks. We note that lateral cracks have reached the surface to form chips. In contrast, the CL image in Figure 5.1 b) shows an additional contrast due to dislocations that propagate in $\{111\}$ slip planes while exhibiting lateral and half-penny cracks. The presence of dislocations is supported by the fact that the angle between the dark contrast band and the surface is approximately 54° which corresponds to the angle between $\{111\}$ slip planes and the (001) face (54.74°). We also note that surface features are less visible in this imaging mode.

Figure 5.2 compares the evolution of the crack field and the dislocation field at various indentation loads for both 60° and 120° wedge indenters on a (001) face. The micrographs presented in this figure have been made on several indentations performed at loads ranging from 50 to 400 mN on a (001) face.

In Figure 5.2 a), the dislocation arms extend in diverging $\{111\}$ planes and grow progressively as the indentation load is increased even after the half-penny crack nucleation. The half-penny crack appears at 150 mN and then grows deeper as the load increases. Some lateral cracks are visible when the load reaches 300 mN (right side of the indentation).

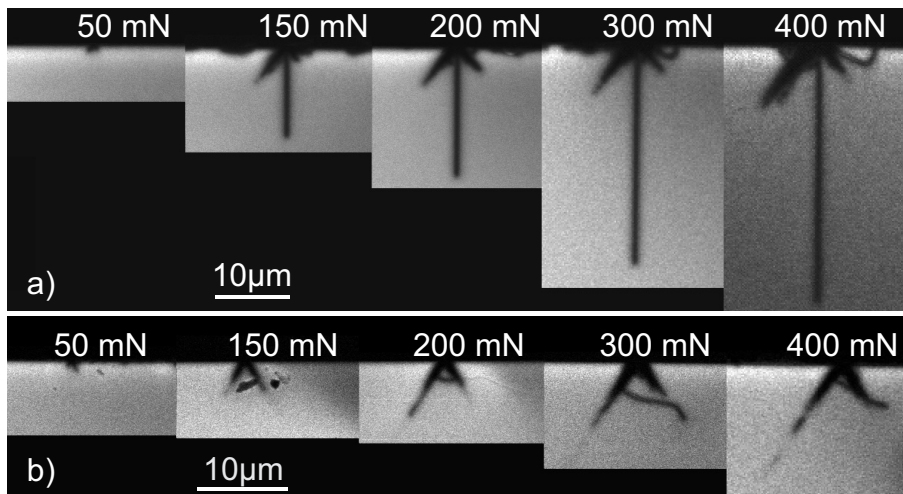


Figure 5.2: Series of CL micrographs comparing the evolution of crack and dislocation fields for a) a wedge 60° indenter, and b) a wedge 120° indenter.

Figure 5.2 b) shows the cross-sections of wedge 120° indentations. In contrast to the 60° wedge case, and although the figure exhibits an apparent diverging pattern¹, dislocation arms extend in converging $\{111\}$ planes. The convergent structure, revealed by a TEM analysis, will be shown later. In addition, no

¹we talk about a diverging pattern of slip planes when the locus where slip bands intersect (imaginary in this case) is located outside the bulk. In the converging case, the locus where slip bands intersect is located below the imprint. A schematic is presented in Table 5.1 on page 103.

half-penny crack is visible and lateral cracks intersect $\{111\}$ planes and initiate crack along these planes as already observed in Section 4.2.2.3.

Our CL observations confirm the strong interaction that exists between the angle of the wedge, the deformation and the cracking process. However, although we have confirmed that the two wedge angles promote two distinct behaviours, CL observations do not allow a clear understanding of the interaction between deformation and crack initiation, and further investigation is required.

Figure 5.3 a) is a TEM micrograph of a wedge 60° indentation. The maximum load was 200 mN and the loading rate was 5 mN/s. The plane of the lamella is (110) and the edge of the indenter was aligned with the $[110]$ direction. For further discussion, we subdivide the TEM lamella into different areas.

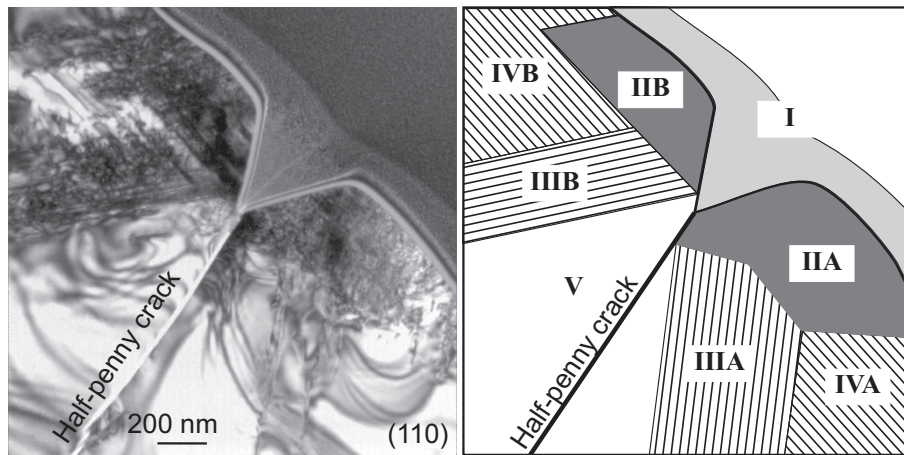


Figure 5.3: TEM micrograph and simplified schematic view of a Wedge 60° indentation made at 200 mN. The edge of the indenter is aligned with the $[110]$ direction.

The layer of deposited platinum is labelled I on the schematic view presented in Figure 5.3 b). Between this platinum layer and the indented surface, there is an amorphous layer of GaAs that is a few nanometres thick. This layer is due to the fact that the platinum layer was deposited with the ion beam source and not with the electron beam thus damaging the GaAs surface over a few nanometres. Area II (A and B) is located in the immediate vicinity of the imprint. It does not extend much further than the residual imprint and its lateral extension corresponds to the pile-up dimension measured at the surface. This zone undergoes the highest deformation and contains a large amount of disordered dislocations. In this area, diverging, converging and also horizontal portions of dislocations are observed but no characteristic pattern really emerges. In zone III (A and B), dislocations arrange in a diverging pattern following (111) (area IIIB) and $(\bar{1}\bar{1}\bar{1})$ (area IIIA) slip planes. Area IV (A and B) is located on both side of areas II. It mainly contains dislocations running parallel to the surface. These dislocations are found up to a few microns away from the imprint. Zone V is nearly free of dislocations. It is located immediately beneath the apex of the imprint and is delimited by the $(1\bar{1}\bar{1})$ and $(\bar{1}11)$ planes.

The half-penny crack separates this area into two portions.

Looking at the different Selected Area Diffraction Patterns (SAED) on Figure 5.4 taken at various places on the lamella, the lack of double spots indicates that no micro-twinning occurred in this case [1].

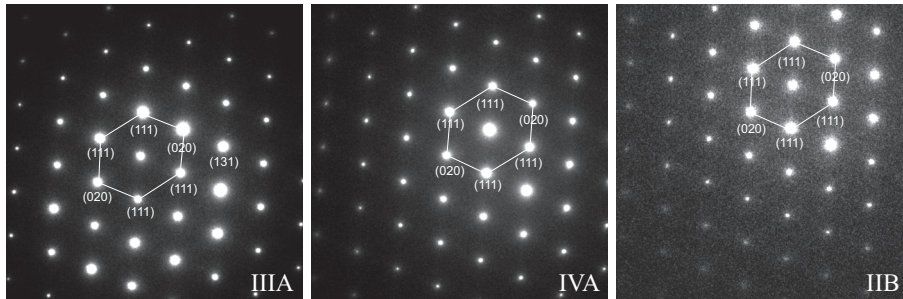


Figure 5.4: Series of SAED patterns taken at different locations under a wedge 60° indentation. The zone axis is $[110]$.

Figure 5.5 is a TEM micrograph of an indentation made with the wedge 120° indenter performed under conditions similar to those for the 60° wedge indentation. The plane of the lamella is (110) with the indenter edge aligned with the $[110]$ direction.

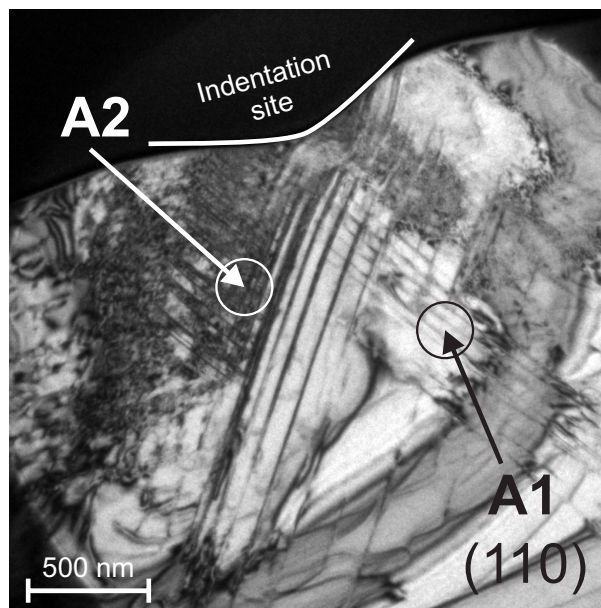


Figure 5.5: TEM micrograph of an indentation Wedge 120° with the main edge aligned with the $[110]$ direction. The plane of the lamella is (110) . The maximum load used is 200 mN and the loading rate is 5 mN/s.

As for the wedge 60° indenter, a highly deformed zone is present in the vicinity of the indenter. Slip bands are curved in this area due to the high density

of dislocations that produce interaction forces [2]. Segments of dislocations running parallel to the surface are also found in the far field of the indentation site. A Burger's vector analysis using the $\vec{g} \times \vec{b} = 0$ method conducted on the horizontal dislocations reveals that they are segments of dislocations with Burger's vector lying along a $\langle 110 \rangle$ direction. Contrary to the 60° wedge indentation, the slip bands converge to intersect below the apex of the imprint and no half-penny crack is present.

HRTEM micrographs taken in the areas A1 and A2 are presented in Figures 5.6 and 5.7 respectively. SAED patterns taken in these areas are also presented in these figures. In Figure 5.6, the pattern of diffracted beams is rounded since the beam was slightly misaligned with the $[110]$ zone axis. The double spots reveal the presence of microtwins. The $(\bar{1}\bar{1}1)$ twinning planes are indicated by dashed lines on the HRTEM images.

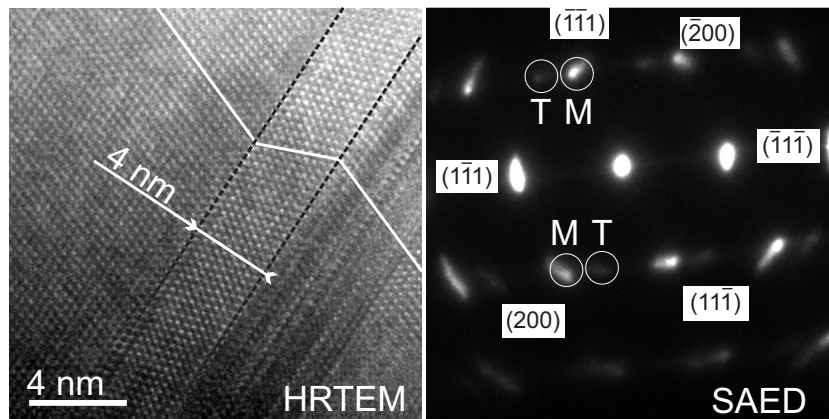


Figure 5.6: a) HRTEM and b) SAED pattern of area A1 in Figure 5.5 (zone axis $[110]$). The two $(\bar{1}\bar{1}1)$ micro-twinning planes have been highlighted (dashed lines) on the HRTEM picture. Double spots indicate microtwins (M is for Matrix and T is for Twin).

In Figure 5.7, two twinning planes are found: $(\bar{1}\bar{1}1)$ and $(\bar{1}\bar{1}\bar{1})$. The corresponding HRTEM image, although taken in the same area shows only one twinning plane.

From the two precedent experiments, we already see that two distinct dislocation structures are found. In order to understand the transition between the two structures, we performed experiments with a 90° wedge indenter.

Figure 5.8 presents the results obtained with a 90° wedge indenter on a (001) face. The maximum load, the load rate and the orientation of the indenter are identical to the 60° and 120° wedge indentations presented above.

On the TEM bright field micrograph presented in Figure 5.8 a), the deposited platinum layer (1) has been thinned during the polishing process. Horizontal segments of dislocations (2) are observed far from the indentation site. Just below the imprint, an array of converging dislocations (3) is present. As for wedge 60° and wedge 120° , a zone of high dislocations density (4) is found on each side of the indenter. The bright field micrograph in Figure 5.8 b) is a magnified view of the area just below the imprint. The angle between slip

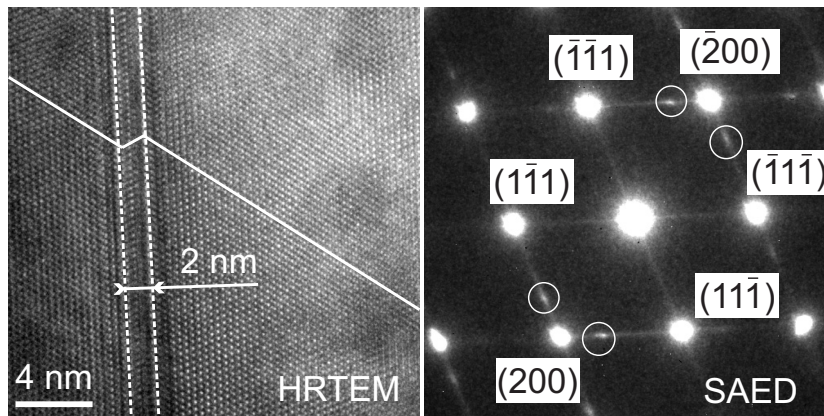


Figure 5.7: a) HRTEM and b) SAED pattern of area A2 in Figure 5.5 (zone axis $\langle 120 \rangle$). The double spot (highlighted by white circles) indicate microtwinning. $(\bar{1}\bar{1}1)$ and $(1\bar{1}\bar{1})$ are the two twinning planes.

planes is about 71° which confirms the $\{111\}$ nature of slip planes. A few double spots are visible on the corresponding diffraction patterns (see inset in Figure 5.8 a)) that confirm the presence of microtwins.

Looking at Figure 5.8 b), we concentrate on the appearance of slip bands under the indentation. The width of these slip bands is similar to the width of the ones encountered under 120° indentations which are in fact microtwins. This observation suggests that the nature of the slip bands below 90° and 120° indentations is the same and hence that microtwinning is the main deformation mechanism that takes place under 90° wedge indentations.

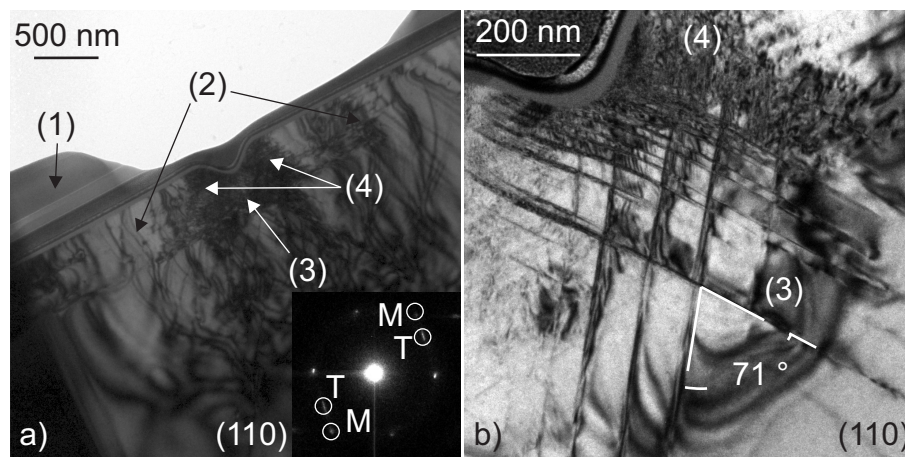


Figure 5.8: Bright Field TEM micrographs of wedge 90° indentations made on a (001) face with edge aligned with the $[110]$ direction. The plane of the lamella is (110). Maximal load, 200 mN and loading rate 5 mN/s. The inset is an SAED pattern showing the double spots structure.

5.2.1.2 Effect of Crystal Orientation

In the literature, several authors reported an asymmetric cracking behaviour around Vickers indentations. In particular, Warren *et al.* [3] have put forward the lack of half-penny cracks along the $[110]$ direction (i.e. $(1\bar{1}0)$ plane) while Margevicius [4] reported that indentation cracks propagating along $[1\bar{1}0]$ (i.e. (110) plane) were considerably shorter than in the orthogonal direction. In both cases, this difference was attributed to the mobility of the dislocations moving along these two $\langle 110 \rangle$ directions. Several authors have also reported distinct types of dislocations depending on the $\langle 110 \rangle$ direction. Taking advantage of the elongated edge of the wedge indenter it is possible to activate only one of the $\langle 110 \rangle$ directions at a time. Consequently, the effect of orientation can be explored separately.

The case of the 60° wedge indenter aligned with the $[110]$ direction has already been presented in Figure 5.3. In contrast, Figure 5.9 a) presents the results of an indentation performed under identical conditions apart from the orientation of the main edge which is, in this case, $[1\bar{1}0]$.

The main characteristics of the $[1\bar{1}0]$ wedge 60° indentation (diverging slip planes, area of high dislocation density, half-penny crack, horizontal segments of dislocations, ...) are present for this wedge orientation as well. The main differences with the $[110]$ indentations are the presence of additional cracks labelled *Cr1* and *Cr2* and also the presence of microtwins. It is interesting to note that crack *Cr1* initiates from the imprint and propagates in a (111) plane. The micrograph presented on Figure 5.9 b) is a magnified view of area *AI* that shows four converging microtwins intersecting at a diverging one.

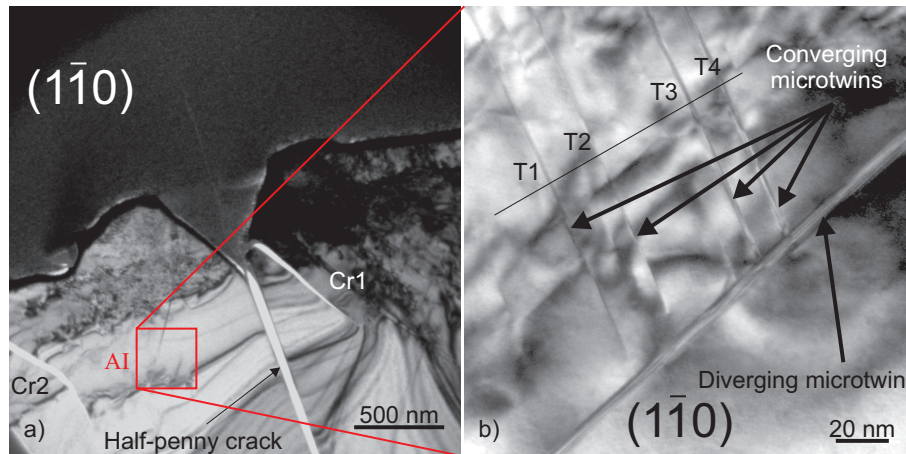


Figure 5.9: a) TEM micrograph of a wedge 60° indentation. The main edge is aligned with the $[1\bar{1}0]$ direction. b) is a magnified view of area *AI* in a) showing convergent microtwins that stop on a divergent one. The maximum load used is 200 mN and the loading rate is 5 mN/s.

The micrograph presented in Figure 5.10 a)) is a HRTEM image of the microtwin labelled *T1* in Figure 5.9 b) which clearly shows the microtwin structure. For convenience, the $\{111\}$ mirror planes have been high-lighted by dashed lines, and the Matrix and Twin are indicated respectively by the *M* and *T* la-

bels. The presence of microtwins is confirmed by the SAED pattern in Figure 5.10 b)) where the typical double spots (M and T arrows) are visible. Contrary to the $[110]$ indentation, microtwins are present at different places on the lamella.

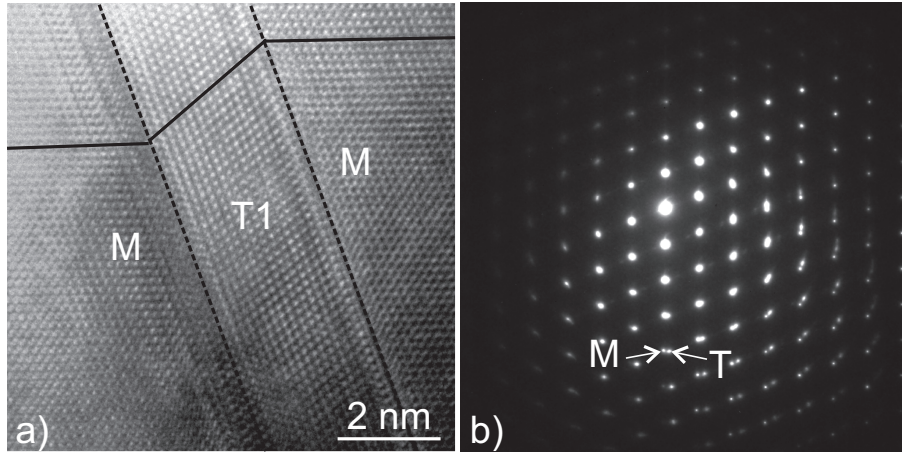


Figure 5.10: a) HRTEM and b) SAED pattern (zone axis $[\bar{1}\bar{1}0]$) of the area AI in Figure 5.9. A microtwin is clearly visible in figure a) with the two microtwinning planes highlighted by the black dashed lines. In the SAED pattern M indicates the spot due to the Matrix and T the one due to the Twin.

In order to gain a further understanding of the effect of crystal orientation on the deformation mechanisms, we conducted a series of experiments on the (110) face of a wafer. The difference between the (001) and (110) faces is depicted in the schematic in Figure 5.11.

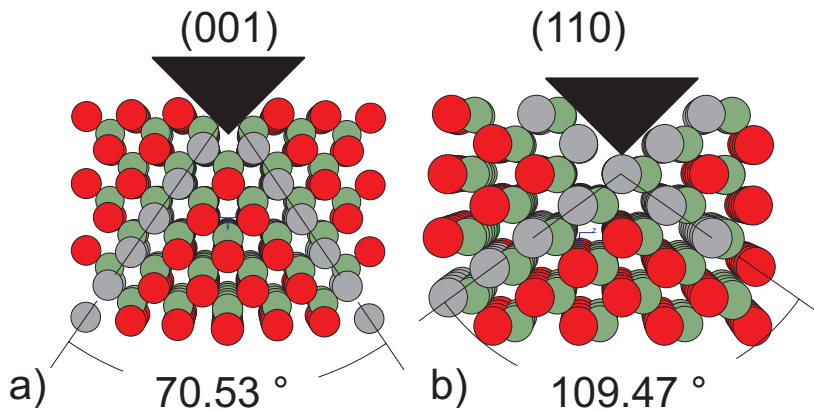


Figure 5.11: Schematic view illustrating the possible slip band structures that can be found under an indentation as seen in a $\{110\}$ plane: a) the indented surface is (001) and the angle between two $\{111\}$ planes is 70.53° , b) the indented surface is (110) and the angle between two $\{111\}$ planes is 109.47°

The main difference concerns the angle between the $\{111\}$ planes which is 70.53° when we perform indentations a (001) face and 109.47° on a (110) face

(angle is measured in a $\{110\}$ plane in both cases). When indenting with the 90° wedge indenter, which has an intermediate apex angle ($70.53^\circ < 90^\circ < 109.47^\circ$), on either a (001) or a (110) face, we expect a different behaviour to take place.

Figure 5.12 a) shows an overview of the area beneath the apex of the imprint (the position of the imprint is drawn on the figure) and the schematic view in Figure 5.12 b) summarises the dislocation structure for the wedge 90° indenter aligned with the $[1\bar{1}0]$ direction on a (110) face. This figure should be compared with Figure 5.8.

We first observe that the strongly strained area is mainly located beneath the apex of the imprint (dotted line on micrograph 5.12 b)). Secondly, both diverging and converging slip planes are activated. The diverging slip bands extend from the walls of the imprint while the converging ones extend from the free surface on both sides of the imprint. We see that although the apex angle is smaller than the angle between $\{111\}$ planes, the convergent slip bands structures is predominant and cross below the imprint.

Finally, a few segment of dislocations perpendicular to the (110) indented surface are visible (arrow A2). These dislocations are similar to those found by some authors on the Vickers indentation of the (011) face [5, 6]. None of the SAED patterns taken on this lamella exhibit double spots suggesting that deformation occurs mainly by the propagation of perfect and/or partial dislocations.

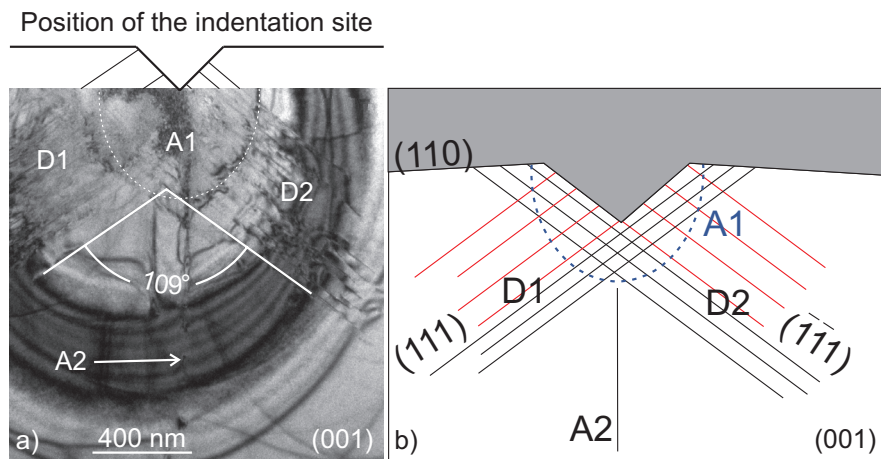


Figure 5.12: a) Bright Field TEM micrographs of wedge 90° indentations made on a (110) face with edge aligned with the $[1\bar{1}0]$ direction, b) schematic view of the structure beneath a wedge 90° indentation on a (110) face. Red lines in area D1 and D2 illustrate diverging dislocations and black lines converging ones.

The different observations presented in this section have been summarised in Table 5.1.

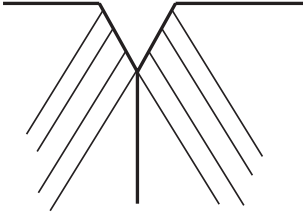
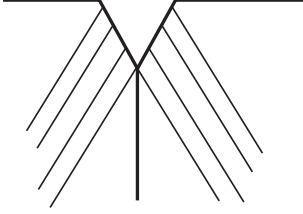
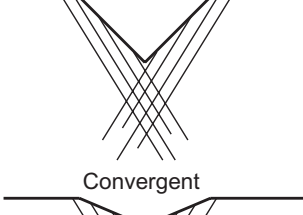
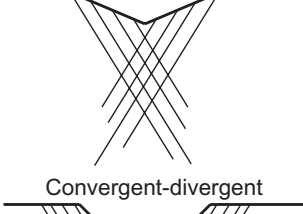
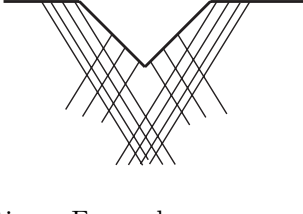
Indenter	Face	Orientation	Micro-twinning (Yes/No)	Main activated slip planes (convergent/divergent)
				Divergent
Wedge 60°	(001)	[110]	No	
				Divergent
Wedge 60°	(001)	[$\bar{1}\bar{1}0$]	Yes	
				Convergent
Wedge 120°	(001)	[110]	Yes	
				Convergent
Wedge 90°	(001)	[110]	Yes	
				Convergent-divergent
Wedge 90°	(110)	[$\bar{1}\bar{1}0$]	No	

Table 5.1: Summary of the results obtained from TEM observations. For each case, the maximum load used is 200 mN and the loading rate is 5 mN/s.

5.2.2 The Case of Point Indenters

5.2.2.1 Conical Indenters

HRSEM micrographs of 60° and 120° conical indentations are compared in Figure 5.13. A comparison of the two residual imprints shows the different distribution of the slip traces with respect to the imprint. In the case of 60° conical indentation (Figure 5.13 a)), slip traces are visible inside² and outside. On the contrary, in the 120° conical case (Figure 5.13 b)), the slip traces are visible mainly inside the imprint. The careful examination of Figure 5.13 b), shows that the Palmqvist cracks, which propagate along $\langle 100 \rangle$ directions, initiate at the crossing of slip traces.

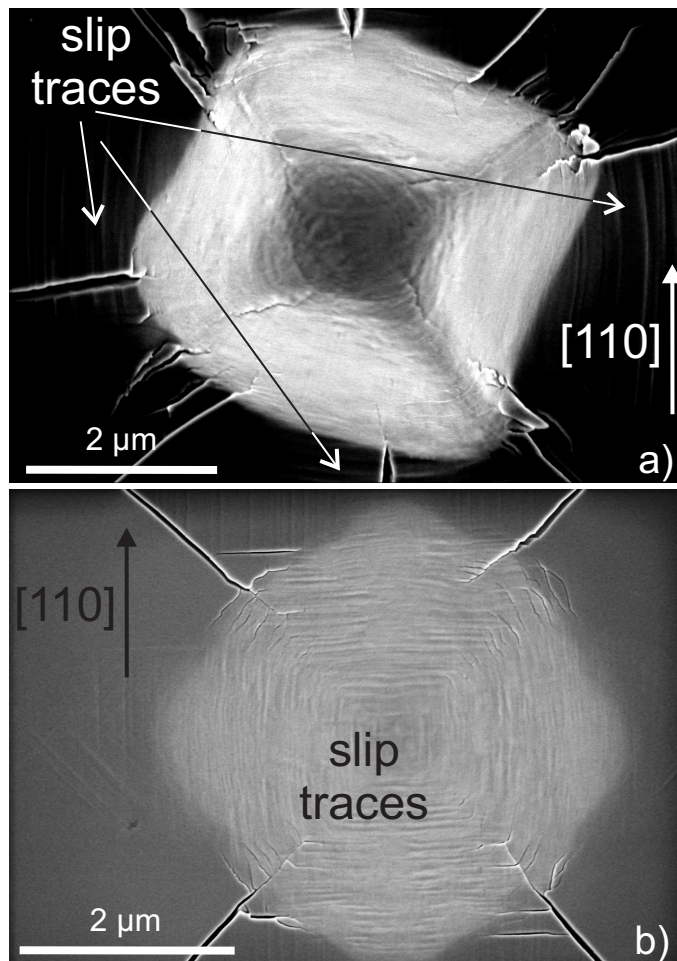


Figure 5.13: Comparison of slip traces at the surface under a) conical 60° (maximal load of 60 mN) and b) conical 120° (maximal load 200 mN) indenters. Note the location of slip traces outside the imprint in the conical 60° case and inside the imprint in the conical 120° case.

²in the present case the high deformation inside the imprint does not allow to see slip traces, however at much lower loads, slip traces are also visible inside

Figure 5.14 a) shows an AFM scan of a conical 60° indentation made with a 25 mN indentation load. Four Palmqvist cracks extend in the $\langle 100 \rangle$ directions. The material piles-up (see arrows labelled pile-up in the figure) on each side of the indentation between the Palmqvist cracks. We also notice that no traces of half-penny cracks are visible at the surface.

The white line A-B in Figure 5.14 a) indicates the position of the cross-profile presented in Figure 5.14 b). On this profile, the position of the surface before indentation is schematised by the black line and the high-lighted area (red) corresponds to the material that has piled-up. It is clearly visible on this profile that only a small part of the indentation volume (i.e. the material that has been deformed) is accounted for by the piling-up of the material. The amount of pile-up progressively vanishes as one approaches Palmqvist cracks.

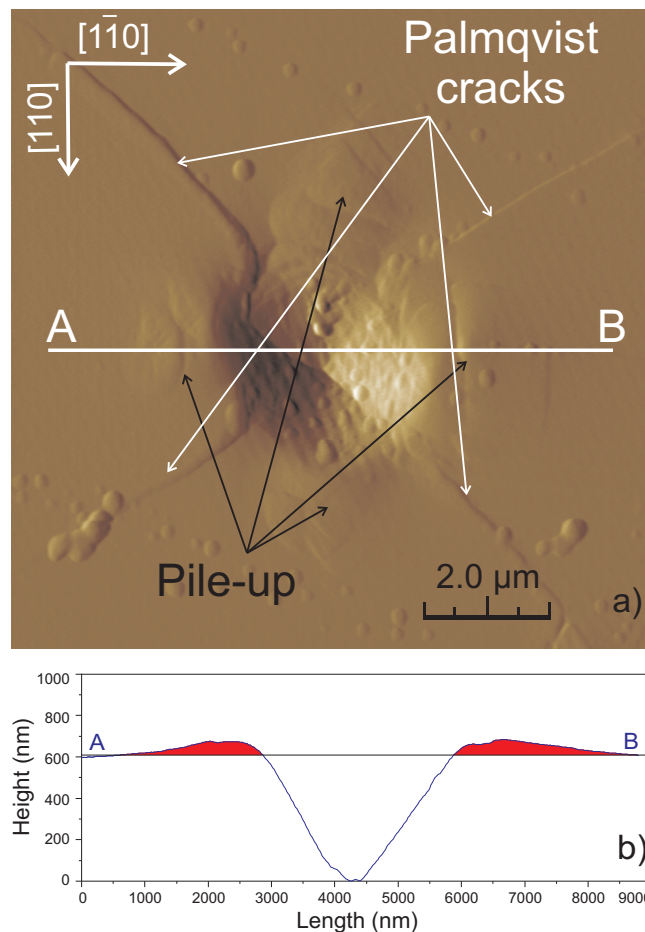


Figure 5.14: a) An AFM view of a conical 60° indentation made with a 25 mN maximal load and b) the cross-profile corresponding to the line A-B in a).

5.2.2.2 Pyramidal Indenters

Figure 5.15 a) is an AFM scan of a cube corner indentation made at a load of 50 mN. Two Palmqvist cracks develop from two of the edges of the indentation and the trace of a half-penny crack is hardly visible in the middle of the face, opposite the edge labelled E_1 .

If we look at the faces that are not aligned with the $[\bar{1}\bar{1}0]$ direction, we remark the presence of two sets of slip lines approximately orthogonal, that emanate from the faces (the slip lines have been high-lighted by thin black lines for convenience). Along the face which is aligned with the $[\bar{1}\bar{1}0]$ direction only one set of slip lines, parallel to the edge, is observed.

The piling-up of the material follows the threefold symmetry of the indenter. As for the 60° conical indentation, materials ridging develops along the sides of the imprint and gradually decreases as one approaches from the corners of the imprint. The cross-profile presented in Figure 5.15 b) illustrates well this last point since almost no pile up is found at point A' (near the edge) while it is maximum at point B' (middle of the opposite face).

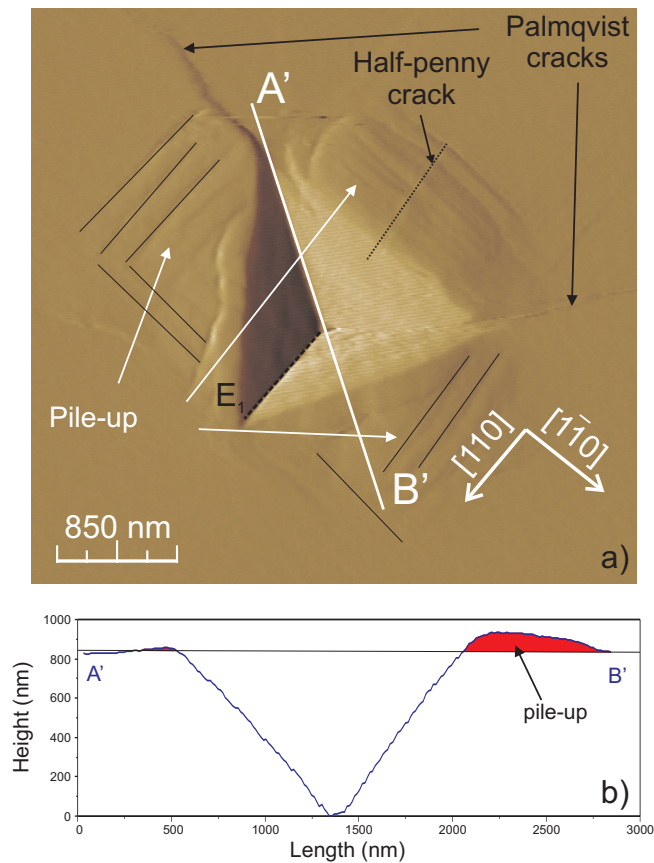


Figure 5.15: AFM micrograph of a cube corner indentation made at 50 mN on a (001) face. The edge labelled E_1 is aligned with the $[\bar{1}\bar{1}0]$ direction.

Figure 5.16 a) shows a Vickers indentation, made with a load of 250 mN. As

for the conical and cube corner cases, the Palmqvist cracks in $\langle 100 \rangle$ directions are clearly visible. No half-penny crack is observed on this indentation.

The white line A''-B'' indicates the position of the cross-profile presented in Figure 5.16 b). As can be seen, very little pile-up is observed around the indentation. The cross-profile of this Vickers indentation is very similar to the cross-profiles of materials that are more sensitive to strain hardening [7].

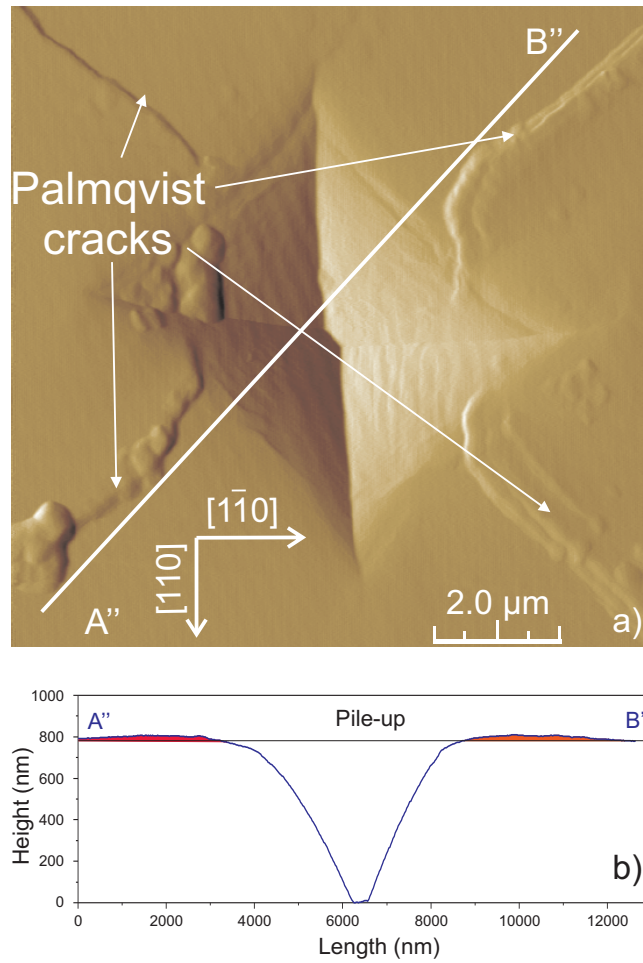


Figure 5.16: AFM view of a Vickers indentation made at 250 mN.

The slip patterns that have been observed around the four investigated indenters (60° and 120° conical, cube corner and Vickers) are summarised schematically in Figure 5.17

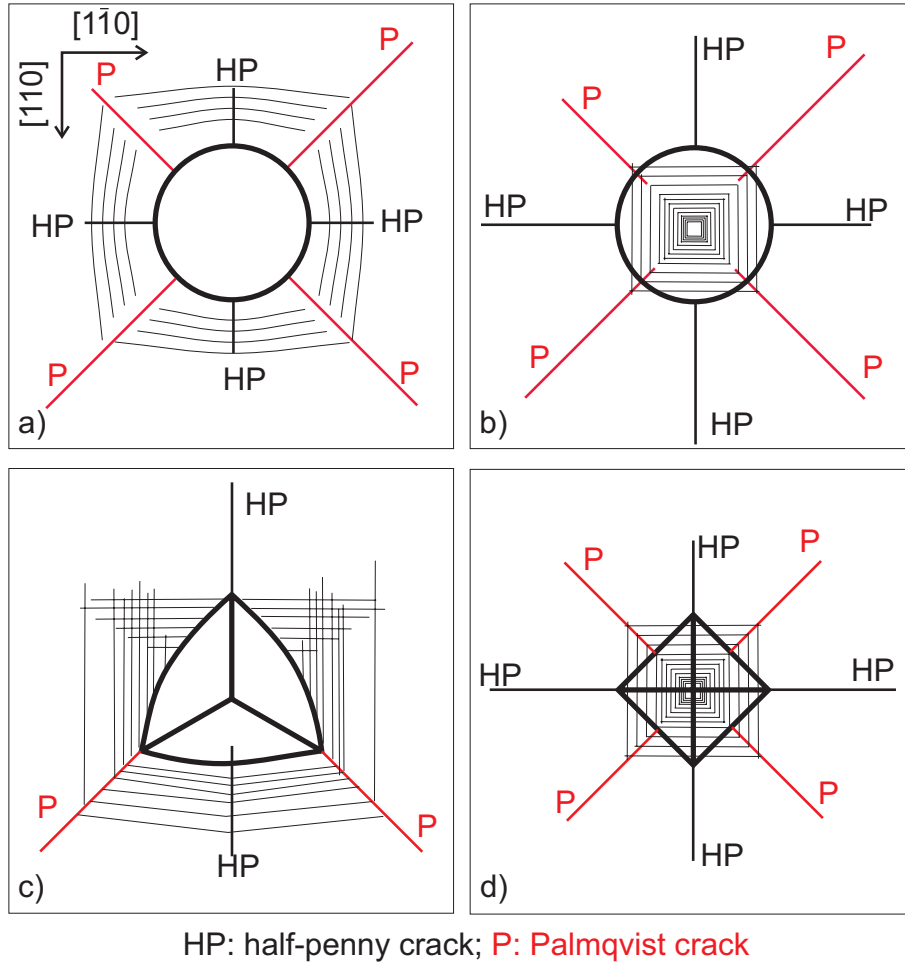


Figure 5.17: The schematic represents idealised views of the surface traces of slip bands and crack fields around a) conical 60°, b) conical 120°, c) cube corner and d) Vickers indentations. The red lines represent Palmqvist cracks, the black lines (bold) represent the half-penny cracks and thin black lines represent the traces of slip bands at the surface.

5.3 Discussion

5.3.1 Deformation by Perfect Dislocations or Micro-twinning

In the literature review, we have seen that the load [8], the strain rate [9], the temperature [10, 11], the dopant level [12] and the anisotropy of the crystal clearly influences the deformation process. Depending on the material and ex-

perimental conditions, microtwinning is reported either in the $[110]$ or in the $[\bar{1}\bar{1}0]$ direction (see [13] for a review).

The first result of our observations on wedge indentations is that the apex angle of the indenter plays a crucial role in the microtwinning process. Namely, if we concentrate on the observations of indentations made along the $[110]$ orientation, we see that 90° and 120° wedge indenters favour the formation of microtwins whereas the 60° wedge indenter favours the formation of perfect dislocations. Furthermore, the comparison of the SAED patterns taken under 90° and 120° wedge indentations reveals that double spots are more difficult to observe in the first case. This last observation suggests that the apex angle of the indenter also influences the number of microtwins that are formed. As a result, we conclude that, at least in the $[110]$ direction, as the apex angle is decreased, there is a transition from a deformation that occurs mainly by microtwinning toward a deformation that occurs mainly by the nucleation and propagation of perfect dislocations.

The second important result is that there is an opposite influence between the role of the apex angle and the role of the orientation. In the case of Vickers indentations, Levade and Vanderschaeve [14] or Koubaiti *et al.* [15], have observed microtwins in the $[110]$ direction³ and perfect dislocations in the orthogonal $[\bar{1}\bar{1}0]$ arm. The presence of microtwins along the $[110]$ direction in the case of 90° and 120° wedge indenters is in line with the observations of these authors. Nevertheless, observations of 60° wedge indentations are contradictory with the observations of Levade *et al.* and Koubaitai *et al.* since with the 60° wedge indenter microtwins form in the $[\bar{1}\bar{1}0]$ direction and not in the orthogonal $[110]$ direction. Keeping in mind that the apex angle of the 60° wedge indenter is significantly different from the apex angle of the Vickers indenter (136°), the opposite influence between the role of these two parameters becomes obvious.

To tentatively explain the influence of the apex angle of the indenter on the twinning process, we have to answer three essential questions:

- Firstly, what is the process at the origin of the formation of microtwins?
- Secondly, what is modified in the process when the indenter apex angle is changed from 60° to 120° ?
- Finally, how do these modifications affect the twinning process?

The answer to the first question is found in the literature. Following the reviewing work of Vanderschaeve [16] on the mechanical twinning in semiconductors, it is suggested that the formation of twins is most likely due to the uncorrelated motion of partial dislocations caused by the different mobilities of two partial dislocations with different character (i.e. α or β). We also mention that, according to some authors [9, 14, 16], microtwins form at or close to the surface.

The answer to the second question is quite obvious. The most evident modification induced by a change of the indenter apex angle is the distribution of the stress field. In particular, we expect that as the indenter apex angle is increased from 60° to 120° , the hydrostatic part of the stress will be increased.

³the results of these authors have been chosen among other results since in their studies, Vickers indentations were performed in similar conditions of temperature and doping type

The third and last question is the more difficult to answer. It is well known that, in the case of uniaxial compression tests, an intense confining pressure changes the macroscopic behaviour of GaAs from a brittle (without pressure) to a ductile behaviour [16, 17], generally accompanied by the formation of twins [18]. However, in the case of wedge indentation, it remains still unclear how the modification of the stress distribution influences the mobilities of partial dislocations and hence, the formation of microtwins.

It appears that further experimental work is required to clearly understand the relation between the apex angle of the indenter and the formation of microtwins. In particular, it would be interesting to complement the results with TEM observations of 90° and 120° wedge indentations along the $[1\bar{1}0]$ directions.

We want to emphasise that whether the deformation process is made through the creation and propagation of twins or perfect dislocation does not affect the final length of the half-penny crack (**crack propagation**). Indeed, measurement of the final half-penny crack length, carried out in both $[110]$ and $[1\bar{1}0]$ directions, have shown that it is independent of the orientation of the indenter edge at identical loads. However, the deformation process has a clear influence on the half-penny **crack initiation** process.

This is particularly visible when comparing the load-displacement curves of two 60° wedge experiments as in Figure 5.18. On this graph, we make three observations:

- at a given load level, the penetration of the indenter is more important along the $[1\bar{1}0]$ direction than in the orthogonal $[110]$ direction;
- there is no pop-in excursion in the case of the $[1\bar{1}0]$ indentations;
- the unloading curves have similar slopes independently of the observed $\langle 110 \rangle$ direction.

Considering the first 250 nm of the loading sequence⁴, the first observation means that indentations performed along the $[1\bar{1}0]$ direction exhibits more plastic deformation than those performed in the $[110]$ direction. If we correlate this result to TEM observations, we see that the difference in plasticity can be associated with the formation of microtwins. We also remark that the direction in which we find microtwins is associated with the tougher direction (i.e. the direction in which cracks are usually shorter when indenting with point indenters).

The lack of pop-in extension along $[1\bar{1}0]$ might be explained either by the formation of microtwins as already observed by Wang *et al.* [19] or by the small inclination of the wedge indenter with respect to the indented surface. With the first hypothesis, the elastic strain energy stored in the crystal is smaller for partial dislocations than for perfect ones [2]. As previously seen, microtwins are generated by a succession of partial dislocations trailing stacking faults [2, 14, 16]. Consequently, the amount of elastic strain energy available to be released in crack initiation is reduced when indenting along $[110]$. Since the pop-in length is directly related to the energy released in crack formation (see the energetic analysis conducted in Section 4.2.2.1), it becomes obvious that smaller

⁴in this part of the loading sequence, plastic deformation is the main process that takes place under indentation

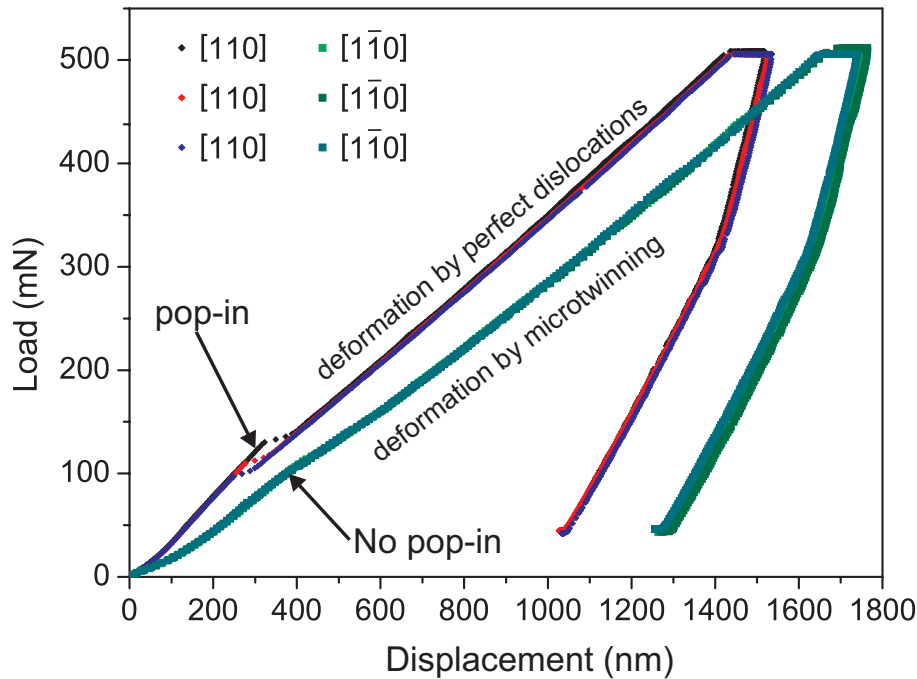


Figure 5.18: Comparison of 60° wedge indentation curves along $[110]$ and $[\bar{1}\bar{1}0]$ directions. Note the absence of pop-in in the $[\bar{1}\bar{1}0]$ curves.

or even no pop-in excursion are found along the $[\bar{1}\bar{1}0]$ direction. With the second hypothesis, the differences in the load-displacement curves would be explained by the fact that when the indenter is turned by 90° , the small inclination of the indenter edge with respect to the indented surface is changed. It is reasonable to assume that in this case the contact conditions between the indenter and the surface are sufficiently modified to explain the change in load-displacement histories.

5.3.2 Arrangement of Dislocations around Indentations

The dislocation structure found under wedge indentation presents some similarities with the one found under Vickers indentation by several authors. First, the zone in the immediate vicinity of the imprint is strongly strained and presents a very high density of dislocations. Then, the horizontal segments of dislocations having their Burger's vector parallel to the surface (\vec{b}_1 in Figure 5.19) are found away from the indentation site. These horizontal segments are similar to the "rosette arms" often seen in the literature and described in details by Levade and Vanderschaeve [14]. Finally, dislocations beneath the indentation have their Burger's vector inclined to the surface (\vec{b}_2 in Figure 5.19) and propagate in $\{111\}$ planes forming a V-shape configuration being either diverging (the locus where slip bands intersect is out of the material up to the imprint) or converging (the locus where slip bands intersect is under the imprint in the material). The two dislocation configurations are similar to those predicted by Roberts [20] and already observed by Le Bourhis [13] and Levade and Vanderschaeve [14]. A

schematic of the two configurations is presented in Figure 5.19.

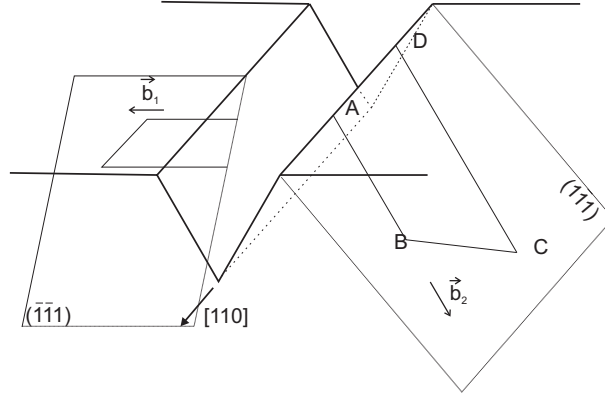


Figure 5.19: Schematic view of the Burger's vector configurations. \vec{b}_1 Burger's vector $\langle 101 \rangle$ parallel to the surface, \vec{b}_2 Burger's vector inclined to the surface in either $\langle 110 \rangle$ (perfect dislocation) or $\langle 121 \rangle$ (partial dislocation) configurations.

The most important aspect concerning the half-penny crack initiation is the convergent or divergent slip systems that are activated when changing the indenter geometry. If we first consider the half-penny crack initiation in (001) indentations, a comparison of the three indenters (60° , 90° and 120°) shows that in the 60° case, the half-penny crack is initiated very early (below 200 mN as shown in TEM experiments), in the 90° wedge case, the half-penny crack initiation is delayed to around 400-500 mN and in 120° wedge experiments, the half-penny crack does not initiate (or very rarely) even at loads up to 1.5 N. If we turn now to the comparison of the dislocation patterns, we observe a predominant diverging pattern in the case of the 60° wedge experiments, and a convergent pattern predominant in the 90° and 120° wedge cases. These observations establish that the activation of diverging slip systems favours the nucleation of a half-penny crack under wedge indentations. In contrast, the activation of slip systems that converge under the wedge indentation act as mechanism of stress relaxation and also as a plastic shielding process that delays the half-penny crack nucleation.

After the first experiments conducted with 60° and 120° wedge indenters, it was initially postulated that there is a discrete transition between the diverging and the converging patterns when the apex angle of the indenter overcomes a critical value of approximately 70° which corresponds to the angle between $\{111\}$ slip planes. This postulate was based on the fact that it is not possible for a dislocation to move on a converging plane when the apex angle of the indenter is smaller than 70° since it would have to intersect the indenter (see Figure 5.11). However, our experiment with the 90° indenter on a (110) face demonstrates that it is not the case since in that case we observe a mixed converging-diverging pattern instead of a diverging one. Hence, this last point suggests that the converging structure becomes progressively predominant as the apex angle is increased and that dislocation nucleation takes place preferentially at the free surface.

Previous authors stated that median cracks initiate at the pile-up of dislo-

cation below spherical [21, 22, 23, 24] or Vickers indentations [13, 25, 26, 27]. Our observations shows that it is not always the case. Indeed, we have seen that under 60° wedge indentations the half-penny crack initiate in a dislocation free area, whereas under 90° or 120° wedge indentations, we have a converging pattern of dislocations that leads to a dislocation pile-up and associated with a delayed initiation of the half-penny crack.

In our attempt to explain the mechanism of the half-penny initiation, several issues have been explored, including FE simulations or modelling with the help of the slip line field [28]. We expected to find a large difference in the stress fields and particularly concerning the tensile stress below the indenter. This was however not the case, and none of these issues has given satisfactory results to explain the formation of the half-penny crack. Although it is clear that an intense tensile stress exists below the indenter, the origin of the defect from which the half-penny crack is nucleated is still uncertain and necessitates further experimental work.

5.3.3 The Role of the Indenter Shape in the Macroscopic Deformation

Two main results have been outlined by the observations related to point indentations:

- the piling-up behaviour depends strongly of the indenter geometry (shape, apex angle);
- the intersection of different slip systems and the indenter edges are preferential sites for Palmqvist crack initiation.

Let us first consider the piling-up behaviour of GaAs. The deformation of material around indentations is not uniform and follows the symmetry of the indenter. In addition, the material displacement upward vanishes as one approaches the corner of the indentations or Palmqvist cracks. The observation of AFM cross-profiles relative to the various indentations clearly shows that the material pile-up around indentations does not account for the totality of the material displaced during the process. The question of the deformation by a volume conservative process is therefore raised.

Piling-up or sinking-in are commonly observed effects in the indentation of metals and ceramics. The transition from a piling-up to a sinking-in behaviour is commonly attributed to two causes: the indenter apex angle and the ability of the material to strain-harden. The effect of the indenter apex angle has been evidenced by several authors in the case of indentation of metals by wedge [29, 30, 31], conical [32], and pyramidal indenters [33, 34]. On the other hand, the work of Dugdale [29], Hill [35] on the wedge indentation of metals and the work of Alcalà *et al.* [7] on Vickers and spherical indentation of metals and ceramics has clearly demonstrated that as the strain-hardening exponent of the material is increased, the sinking-in behaviour is promoted.

In the specific case of GaAs, we have evidenced that the apex angle influences the piling-up behaviour. In the light of our observations, we also believe that the apex angle of the indenter could promote a strain-hardening effect. Namely, our investigations of the dislocation structure below 120° wedge indentations have evidenced two effects:

- firstly, the preferential activation of convergent slip systems under obtuse indenters favours the interaction between dislocations under the indenter and hence, strain-hardening;
- secondly, microtwins are generally found under obtuse indenters. These microtwins are strong barriers to the motion of dislocations and are widely accepted as a major source of work-hardening in crystalline materials [2].

Le Bourhis and Bradby [13, 22, 23, 24] have shown both that Vickers and spherical indenters⁵ induce a convergent structure below the indentations. The converging structure found under these indenters could also induce a possible strain hardening. To clarify this point, it would be interesting to compare the mechanical properties of GaAs that has been previously indented by different indenters. The testing of mechanical properties could be done with the help of instrumented nanoindentation.

The plastic deformation of GaAs takes place by the formation of slip bands⁶ under the surface. At the surface, the formation of slip bands is characterised by small steps as seen in Figure 5.20.

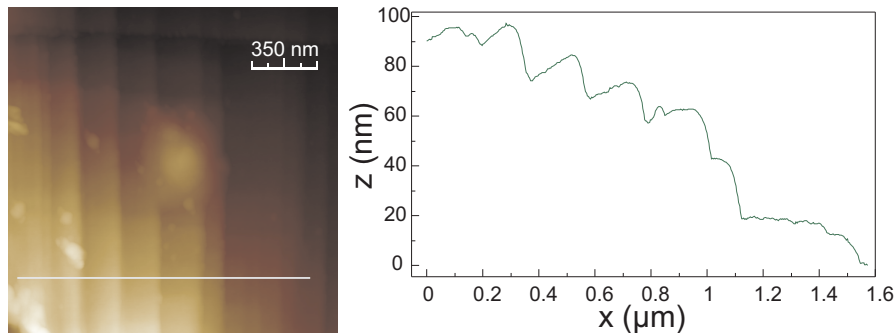


Figure 5.20: AFM scan near a 60° wedge indentation. The main edge of the indenter is oriented along a $\langle 100 \rangle$ direction. A cross-profile is extracted from the right side of the indentation to show the steps due to slip bands at the surface.

When compared to wedge indentations, point indenters induce two main changes:

- as can be seen in Figure 5.17 four slip systems are activated instead of two;
- the concentration of the load on a point rather than on a line increases the stress levels and hence the number of dislocations that are nucleated and propagated.

The activation of intersecting slip systems combined with the high number of dislocations that propagate in these latter contribute to the formation of new

⁵in view of the radius of the spherical indenter employed in these study ($4.3 \mu\text{m}$), we can consider that the indenter is obtuse

⁶the term "slip bands" refers to the arrangement of dislocations into bands, not to their nature (perfect, partial or twins)

sites for Palmqvist crack nucleation as evidenced by the examination of Figures 4.28 and 5.13 b). These two figures clearly outline the relation between the intersection of slip traces at the surface and the nucleation of Palmqvist cracks under respectively Vickers and 120° conical indentations.

In the case of pyramidal indenters with well-defined edges, we have so identified two major sites for Palmqvist crack nucleation:

- the interaction of dislocations that propagate in intersecting $\{111\}$ slip planes.
- the edges of the indenter that act as stress concentrators;

The case of the Vickers indenters clearly illustrates the first case since Palmqvist cracks are often seen to initiate from the faces of the indenter at the crossing of slip planes. On the contrary, in the case of cube corner indentations, edges remain the main sites for Palmqvist crack initiation even if Palmqvist cracks are sometimes observed to initiate from the faces. Figure 5.21 illustrates this latter point. In this figure, the initiation sites caused by intersecting slip planes are indicated by arrows (S). Palmqvist cracks initiate at the intersection of the $(\bar{1}11)$ and $(1\bar{1}1)$ slip planes on the right side of the indentation or $(\bar{1}11)$ and $(11\bar{1})$ on the left side of the indentation.

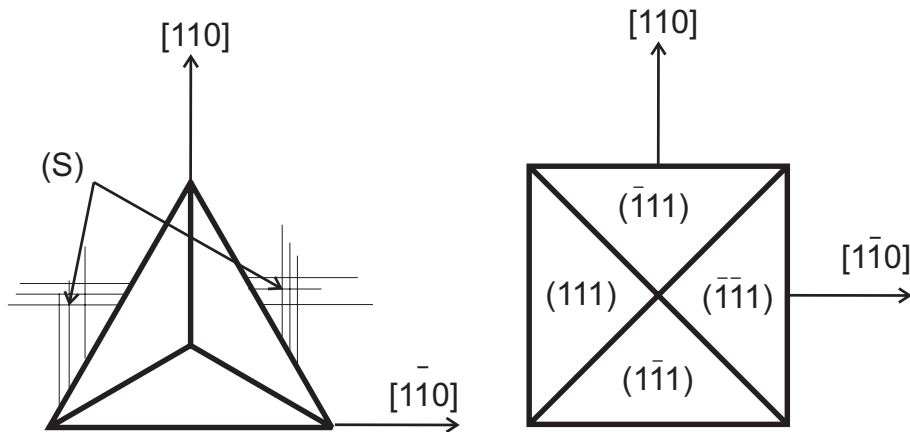


Figure 5.21: Schematic illustration of the initiation of Palmqvist cracks at the intersection of slip traces. The scheme on the left is a view of the residual imprint and the scheme on the right shows the four $\{111\}$ slip planes that can be activated as well as the $[110]$ and $[1\bar{1}0]$ directions.

From this we can conclude that both the indenter shape and apex angle influence the creation of new sites for crack nucleation. It seems that as the indenter apex angle is decreased, stress concentrations are much more pronounced at the edges and cracking will initiate preferentially at these sites (cube corner case). In contrast, as the apex angle is increased, stress concentrations at the edges diminish and the interaction of slip systems becomes a predominant mechanism of crack nucleation (Vickers case).

In addition, we see that when the orientation of the indenter is changed, the orientation of the global stress field with respect to the crystalline structure of

GaAs is also changed. The Resolved Shear Stress (RSS) acting on the different slip systems is modified and hence, more or less dislocations will be nucleated and propagated in intersecting slip systems. If a high number of dislocations is propagated, interaction between dislocations is most likely to occur and new sites for Palmqvist cracks initiation might be formed.

5.4 Conclusions

In this section, we have revealed that many new phenomena related to subsurface plasticity emerge from our observations. In particular, we have seen that the apex angle of the indenter influences the nature of the dislocations that are generated (twins, perfect dislocations) and also their arrangement below the indenter (converging or diverging patterns). It has also been proved that if the microtwinning process influences the nucleation process of the half-penny crack, it does not influence its propagation. We have suggested that the converging pattern of dislocations found under 90° and 120° indenters is a plastic shielding process that delays the formation of the half-penny crack.

In view of these results, and keeping in mind the context linked to the dicing of GaAs, we recommend to use a wedge indenter with an apex angle smaller than 70° in order to favour the nucleation of the half-penny crack. Above this particular value, the convergent pattern of dislocations will become progressively predominant and the half-penny crack initiation will be delayed.

We have shown that the deformation is not uniform and that the pile-up of material follows the shape of the indenter. The shape of the indenter also influences the number of activated slip planes and in some cases promotes the formation of new initiation sites for Palmqvist cracks.

Many interesting points remain however unresolved. In particular it would be of high interest to explain the relationship between the apex angle of the indenter and the formation of microtwins. It is also necessary to clarify the source of the half-penny crack formation in the case of 60° wedge indentations. The effect of the indenter apex angle on the strain hardening behaviour of the material is also an interesting point to clarify.

Although it is beyond the scope of this manuscript, we want to mention that in the case where the available indenter has an apex angle greater than 70° cases, it would be interesting to estimate which pattern (convergent-divergent) is predominant. Such analysis might be possible by computing the stress field beneath the indenter and considering the Resolved Shear Stress (RSS) that acts on particular slip systems. As an example, such estimation has been successfully applied by Roberts *et al.* [20] to the indentation of zincblende semiconductors by a flat punch (this work is based on an earlier work by Brookes *et al.* [36] on MgO).

Bibliography

- [1] J. W. Edington. *Practical Electron Microscopy in Materials Science*, volume 1 to 5. Philips Technical Library, 1977.
- [2] J. P. Hirth and J. Lothe. *Theory of dislocations*. Wiley-Interscience publication. John Wiley & Sons, 2nd edition, 1982.
- [3] P.D Warren, P. Pirouz, and S.G. Roberts. Simultaneous observation of α and β -dislocation movement and their effect on the fracture behaviour of GaAs. *Philosophical Magazine A*, 50(5):23–28, 1984.
- [4] R. W. Margevicius and P. Gumbsch. Influence of crack propagation direction on $\{110\}$ fracture toughness of gallium arsenide. *Philosophical Magazine A*, 78:567–581, 1998.
- [5] E. Le Bourhis, L. Largeau, G. Patriarche, and J.P. Rivière. Deformation of (011) GaAs under concentrated load. *Journal of Materials Science Letters*, 20:1361–1364, 2001.
- [6] L. Largeau, G. Patriarche, E. Lebourhis, A. Rivière, and J.P. Rivière. Indentation induced deformations of GaAs (001) at a high temperature. *Philosophical Magazine*, 83:1653–1673, 2003.
- [7] J. Alcalà, A. C. Barone, and M. Anglada. The influence of plastic hardening on surface deformation modes around vickers and spherical indents. *Acta Materiala*, 48(13):3451–3464, 2000.
- [8] E. Le Bourhis and Patriarche G. Transmission electron microscopy observations of low-load indents in GaAs. *Philosophical Magazine Letters*, 79(10):805–812, 1999.
- [9] K. Wasmer, Parlinska-Wojtan M., R. Gassilloud, C. Pouvreau, J. Tharian, and J. Michler. Plastic deformation modes of GaAs under nanoindentation and nanoscratching. *Applied Physics Letter*, 90:031902, 2007.
- [10] A. Lefebvre, Y. Androussi, and G. Vanderschaeve. A TEM investigation of the dislocation rosettes around a Vickers indentation in GaAs. *Phys. Stat. Sol. A*, 99:405, 1987.
- [11] A. Lefebvre and G. Vanderschaeve. The origin of microtwinning in room temperature indented undoped and n-doped GaAs. *Phys. Stat. Sol. A*, 107:647–653, 1988.
- [12] Y. Androussi, G. Vanderschaeve, and A. Lefebvre. Slip and twinning in high-stress-deformed GaAs and the influence of doping. *Philosophical Magazine A*, 59(6):1189–1204, 1989.
- [13] E. Le Bourhis and Patriarche G. Plastic deformation of III-V semiconductors under concentrated load. *Progress in Crystal Growth and Characterization of Materials*, pages 1–43, 2003.
- [14] C. Levade and G. Vanderschaeve. Rosette microstructure in indented (001) GaAs single crystal and the α/β symmetry. *Phys. Stat. Sol. A*, 171:83–88, 1999.

- [15] S. Koubaïti, C. Levade, and G. Vanderschaeve. Vickers indentation on the {001} GaAs under illumination and in darkness. *Philosophical Magazine A*, 80:83–104, 2000.
- [16] G. Vanderschaeve. Mechanical twinning in semiconductors. *Solide State Phenomena*, 59-60:145–164, 1998.
- [17] E.A. Stach, T. Freeman, A.M. Minor, D.K Owen, J. Cumings, M.A. Wall, T. Chraska, R. Hull, Jr Morris, J.W., A. Zetl, and U. Dahmen. Development of a nanoindenter for in-situ transmission microscopy. *Microscopy and Microanalysis*, 7:507–517, 2001.
- [18] T. Suzuki, T. Yasutomi, T. Tokuoka, and I. Yonenaga. Plastic deformation of GaAs at low temperatures. *Philosophical Magazine A*, 79(11):2637–2654, 1999.
- [19] S. Wang, M. Zhang, J. Bradby, and P. Pirouz. Static microindentation and displacement sensitive indentation tests on undoped GaAs. volume 904E, pages 0904–BB05–08. Materials Research Society, 2005.
- [20] S.G. Roberts, P.D. Warren, and P.B. Hirsch. Hardness anisotropies: A new approach. *Materials Science Engineering A*, 105-106:19, 1988.
- [21] J.E. Bradby, J.S. Williams, J. Wong Leung, M.V Swain, and P. Munroe. Transmission electron microscopy observation of deformation microstructure under spherical indentation. *Applied Physics Letter*, 77(23):3749–3751, 2000.
- [22] J.E. Bradby, J.S. Williams, J. Wong Leung, M.V Swain, and P. Munroe. Mechanical deformation of InP and GaAs by spherical indentation. *Applied Physics Letter*, 78(21):3235–3237, 2001.
- [23] J.E. Bradby, J.S. Williams, J. Wong Leung, S.O. Kucheyev, M.V. Swain, and P. Munroe. Spherical indentation of compound semiconductors. *Philosophical Magazine A*, 82(10):1931–1939, 2002.
- [24] J.E. Bradby, J.S. Williams, and M.V Swain. In situ electrical characterization of phase transformations in si during indentation. *Physical Review B*, 67:1–8, 2003.
- [25] J. T. Hagan and M.V. Swain. The origin of median and lateral cracks around plastic indents in brittle materials. *Journal of Physics D: Applied Physics*, 11:2091–2102, 1980.
- [26] J. T. Hagan. Shear deformation under pyramidal indentations in soda-lime glass. *Journal of Materials Science*, 15:1417–1424, 1980.
- [27] E. Le Bourhis and G. Patriarche. Plasticity of GaAs compliant substructures. *Materials Science and Engineering*, A309-310:478–482, 2001.
- [28] R. Hill. *The mathematical theory of plasticity*. Oxford engineering science series. Oxford university press, London, 1st edition, 1950.
- [29] D.S. Dugdale. Wedge indentation experiments with cold worked metals. *Journal of the Mechanics and Physics of solids*, 2:14–26, 1953.

- [30] J. Grunzweig, I. M. Longman, and J. Petch. Calculations and measurements on wedge-indentation. *Journal of the Mechanics and Physics of Solids*, 2:81–86, 1954.
- [31] J. B. Haddow. On a plane strain wedge indentation paradox. *Int. J. of Mech. Sci.*, 9:159–161, 1967.
- [32] A.G Atkins and D. Tabor. Plastic indentation in metals with cones. *J. Mech. Phys. Solids*, 13(3):149–164, 1965.
- [33] L.E. Samuels and T.O. Mulhearn. An experimental investigation of the deformed zone associated with indentation hardness impressions. *Journal of the Mechanics and Physics of Solids*, 5:125–134, 1957.
- [34] T.O Mulhearn. The deformation of metals by Vickers type pyramidal indenters. *J. Mech. Phys. Solids*, 7(2):85–96, 1959.
- [35] R. Hill. On the mechanics of cutting metal strips with knife-edged tools. *J. Mech. Phys. Solids*, 1(3):265–270, 1953.
- [36] C.A. Brookes, J.B. O’Neill, and B.A.W Redfern. Anisotropy in the hardness of single crystals. *Proceedings of the Royal Society of London: Series A, Mathematics*, 322(1548):73–88, 1971.

Chapter 6

Practical Applications

It has been seen in the previous chapters that when indentations are performed with a 60° wedge indenter, a well defined half-penny crack is created. We have also seen that in the case of longitudinal cross-sections, it is possible to make use of the half-penny crack as a precursor to cleave samples. Although the laboratory setup is similar to the industrial one, major differences remain. As an example of difference between laboratory experiments and industrial production, let us mention that our tests are mainly performed on blank GaAs wafers that have a thickness of $350\ \mu\text{m}$ while commercial structures consist of a set of epitaxial layers grown on a $150\ \mu\text{m}$ thick GaAs substrate.

In order to verify that laboratory results are transferable to an industrial context, we have performed some investigations in collaboration with Bookham AG, Zürich. The purpose of this study is to verify that commercial structures behave similarly to laboratory samples. Furthermore, it is an opportunity to test different experimental parameters under production conditions.

In the first part of this chapter, we first briefly describe the experimental procedure used. Results of the study are then summarised and discussed. Finally, conclusions pertaining to production applications are drawn from these results.

6.1 Experimental Procedure

The 60° wedge indenter (length $55\ \mu\text{m}$) was used to perform indentations on laser structures supplied by Bookham. The sample consists of a fully processed cell having 6 bars, numbered V01 to V06 (a description of a processed wafer is given in Section 1.1). Each bar contains thirty lasers, separated by a band also called street. This street is composed of a central GaAs band surrounded by two silicon nitride (SiN) layers as depicted in Figure 6.1. Indentations were usually centered on the GaAs layer.

The sample was glued with the help of a cyanoacrylate glue on an aluminium sample holder. After indentations, performed with the Nanoindenter XP, the sample was put in an acetone bath to separate it from the holder. The sample was then transferred on a special tape mounted on a ring. After that operation, and before separating lasers, indentations were observed with the help of an optical microscope and, the size of flakes is measured when they are present. Laser devices were finally separated at Bookham AG on the manufacturing facilities employed for the production of commercial lasers.

Five batch of indentations consisting of at least fifteen indentations were done. A single batch consists of at least fifteen indentations performed with the same conditions of load, loading rate. It is also worth noting that all experiments are performed on a single cell, i.e. on the same wafer. As the exact indentation cracking behaviour of GaAs with epitaxial layers was not known, maximal loads in the range of 100 to 500 mN were employed.

6.2 Results and Discussion

In Figure 6.2, we examine the typical load-displacement curves obtained when indenting laser structures with a 60° wedge indenter. Five distinct curves, corresponding to the five maximum loads used (100 to 500 mN), are presented.

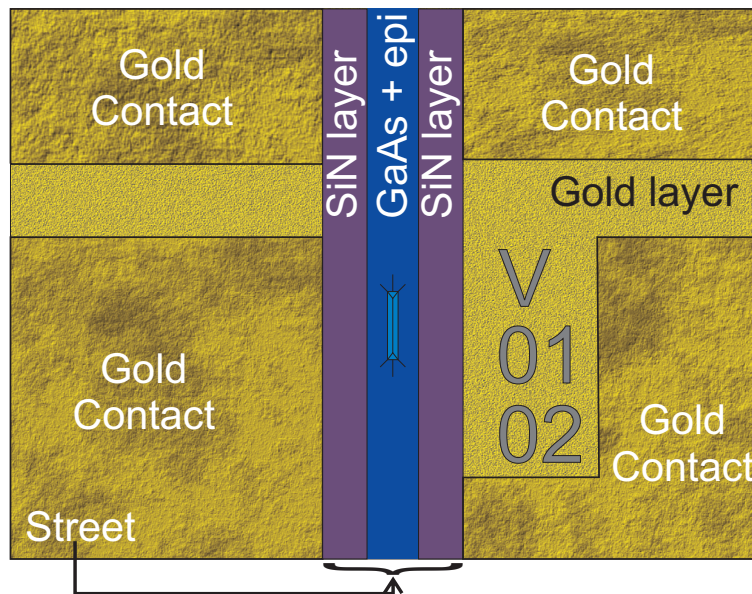


Figure 6.1: Schematic view of a laser structure showing location (inside the GaAs + epi band) of the indentation between lasers

Within a single batch, indentation curves are reproducible, and the presented graph shows a consistency of behaviour between the different loads. Two distinct behaviours of the load-displacement curves are noticed. For the 100 mN indentation curves, neither pop-in in the loading part, nor slope change in the unloading part are observed. For the 200 mN, pop-in is observed in conjunction with a slope change only in three cases out of sixteen indentations (19%). For the three other loading cases (300, 400 and 500 mN), pop-in excursions are observed on all indentations. The pop-in excursions are indicated by arrows in Figure 6.2 and the slope change in the unloading part is easily visible for loads above 200 mN.

As stated in Chapter 4, the absence of pop-in indicates that no half-penny cracks have been nucleated in these experiments conducted at loads lower than 300 mN. This conclusion is supported by both optical observations (presented in Figure 6.4) and subsequent cleavage step, where none of the lasers that belong to the 100 and 200 mN batches could be separated. Figure 6.3 focuses on the batch where the maximum load is 300 mN. The examination of indentation curves shows that as the pop-in load is increased, the corresponding length of the pop-in excursion is also increased. Following the energetic analysis conducted in Chapter 4 (see Section 4.2.2.1 for details), this observation suggests that the later the half-penny crack nucleates (i.e. pop-in load increased), the larger the initiated crack will be (i.e. more energy dissipated in crack formation).

Optical micrographs of the indentations show that those indentations performed with load lower than 300 mN do not exhibit traces of half-penny crack at the surface as shown in Figure 6.4. As stated before, none of the laser devices on these two samples (bar V05, laser 01 to 31) was correctly separated and this observation confirms that if no pop-in is observed in the load-displacement

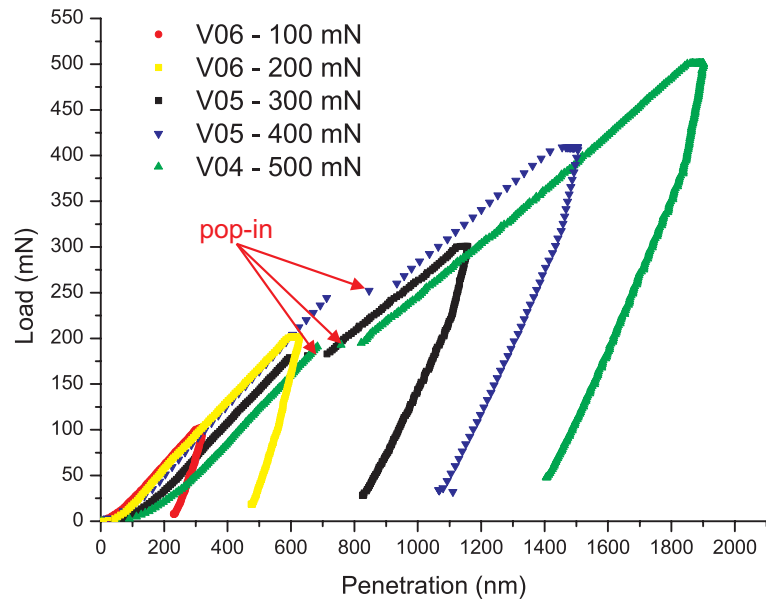


Figure 6.2: Typical load-displacement curves for 60° wedge indentations. The maximal loads are in the range of 100 to 500 mN.

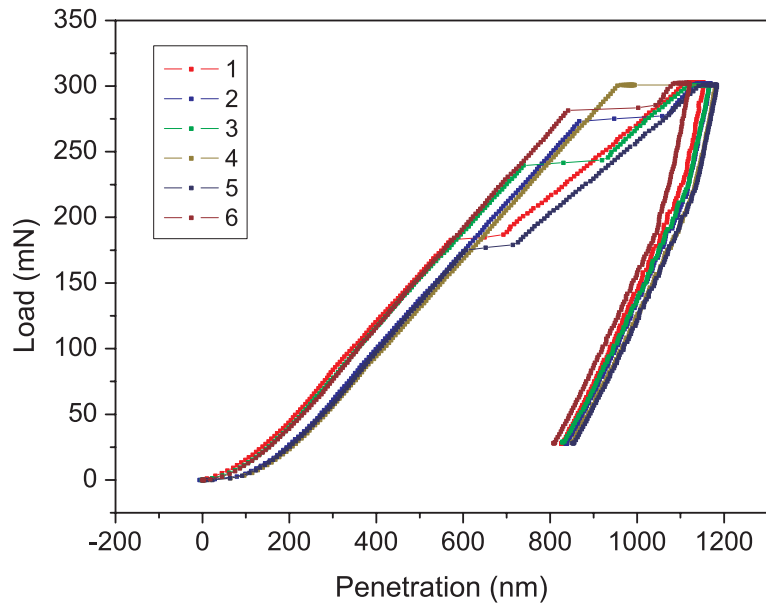


Figure 6.3: Typical load-displacement curves for 60° wedge indentations performed with a maximal load of 300 mN. Note the variations in the pop-in load as well as the different length of the corresponding pop-in penetration.

curve, no half-penny crack is nucleated.

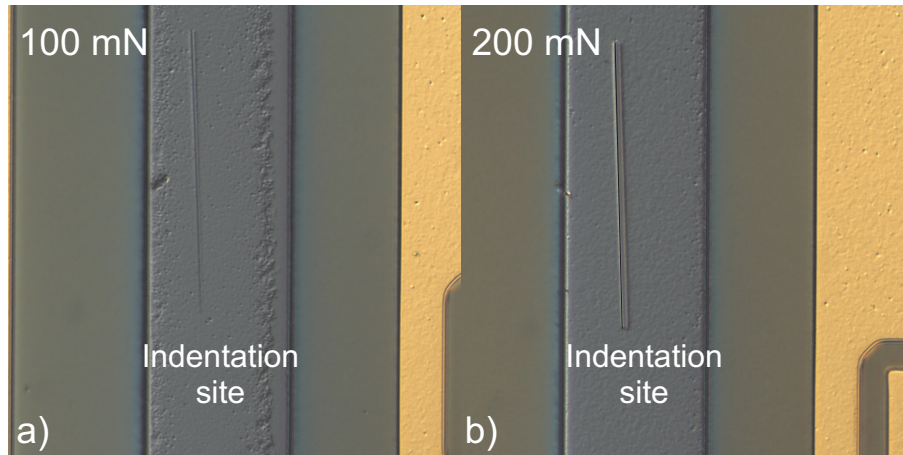


Figure 6.4: Optical micrographs of indentations performed with a 60° wedge indenter at a) 100 mN and b) 200 mN. Width of field $87 \mu\text{m}$.

Figure 6.5 presents optical micrographs of indentations performed with higher maximal loads. The typical traces of the half-penny crack as well as small chips spreading-out at the indenter extremities are visible at the surface.

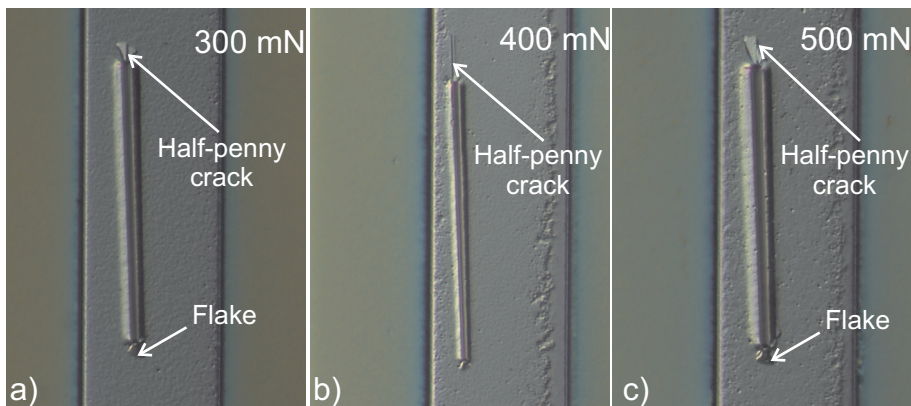


Figure 6.5: Optical micrographs of indentations performed with a 60° wedge indenter at a) 300 mN and b) 400 mN and c) 500 mN. Width of field $60 \mu\text{m}$.

Before cleavage, two different chipping configurations are observed. Figure 6.6 a) illustrates the first configuration where some flakes extend along the side of the indenter near an extremity of the indentation. The second configuration, illustrated in Figure 6.6 b), is observed when the indentation is made at the limit between the GaAs and the SiN epitaxial layers. In that case, the material is crushed along the side of the imprint.

After cleavage, the indented surface was carefully examined with an optical microscope to look at chipping-out. The level of chipping-out is determined for each laser and then classified in 4 levels. The definition for each damage level as well as an illustration is given in Table 6.1.

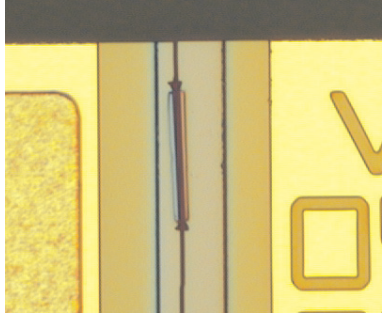
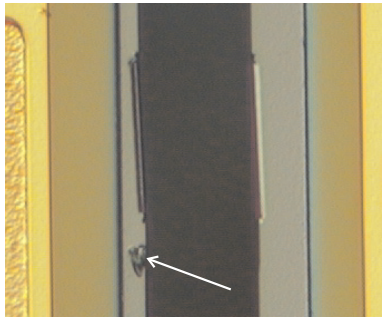
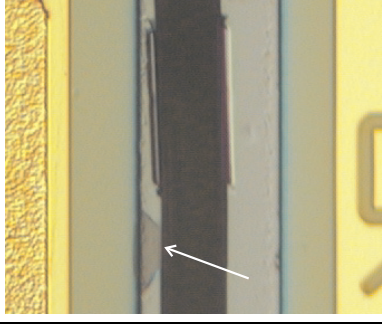
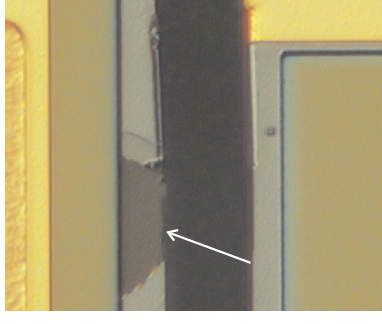
Chipping-out level	Illustration
Level 1: no chips	
Level 2: chips extend in GaAs layer	
Level 3: chips extend in SiN layer	
Level 4: chips extend in gold layer, laser is rejected	

Table 6.1: Classification of the levels of chipping-out after indentation and cleavage and the corresponding illustrations. Chips are indicated by white arrows.

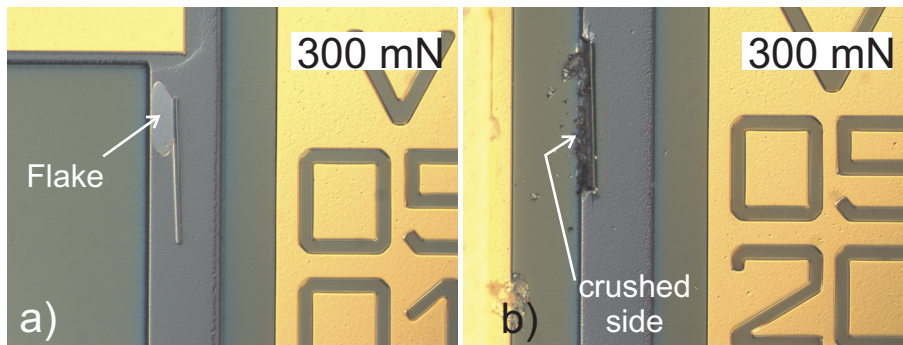


Figure 6.6: Optical micrographs of indentations performed with a 60° wedge indenter. a) a flake extend along the side of the indenter, b) material is crushed along the side of the indentation. Width of field $170\ \mu\text{m}$.

The results after the separation process are given in Figure 6.7 which plots for each load level, the percentage of lasers having either not been cleaved or having reached a certain level of chipping damage. Looking at the graph, we see that none of the lasers indented with loads of 100 and 200 mN were broken. This confirms that no half-penny crack was created for these loads. As the maximal load is increased from 400 to 500 mN, the number of unbroken lasers strongly diminishes (from approximately 40% down to 5%). At 500 mN, about 76% of the broken lasers exhibit chipping levels within level 1 and 2 (GaAs layer) and 20% are within level 3 and 4.

For all the experiments mentioned above, deviation of the cleavage crack from the prescribed path was found. This effect, sometimes encountered in the production for scribed lasers, is most likely due to the fact that the production tool parameters were not optimised to cleave samples with indentations. Indeed, as only a relatively small number of samples had been prepared by the indentation process, it was not possible to optimise the production setup for these conditions.

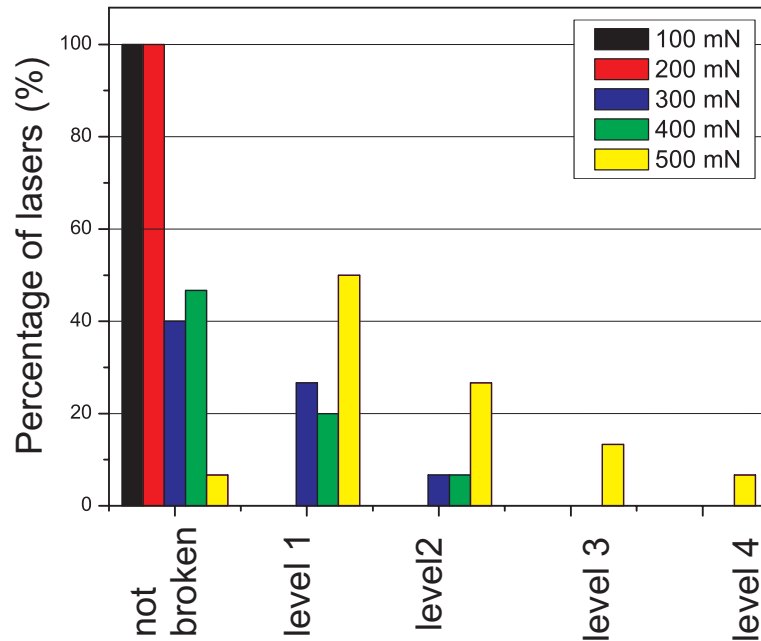


Figure 6.7: Summary of the results after laser separation for single indentation at load from 100 mN to 500 mN.

6.3 Conclusions

The results of experiments on commercial lasers show that it is possible to properly cleave laser devices from crack precursors generated by a 60° wedge indenter. Although the observed levels of chipping-out does not actually fit the requirements for production, these preliminary results are encouraging. In particular, we insist on the fact that neither the geometry of the wedge nor the parameters of the production setup were optimised. Therefore, our results underline that an effort has to be made on the optimisation of the wedge geometry in order to reduce the chipping-out occurrences.

In order to optimise the indentation process, we have to: 1) optimise the termination of the wedge (as proposed in Chapter 4) and 2) increase the wedge length to obtain cracks having a similar length to those obtain with the scratching process ($\sim 200 \mu\text{m}$).

Changing the length of the indenter will certainly result in an higher initiation load for the half-penny crack. This underlines the need to explore the relation between the wedge length and the load necessary to initiate the half-penny crack. This will also require to introduce the wedge length into models for crack growth prediction.

Chapter 7

Conclusions and Perspectives

7.1 Work Overview and Main Contributions

The main postulate of this thesis given in the introduction of this manuscript was that **indentation fracture using an indenter of appropriate shape will enhance the formation of a suitable half-penny crack necessary to the cleavage process while strongly reducing particles formation in both indentation and cleavage steps**. In the different chapter of this dissertation we have contributed new in sight and knowledge to many aspects of the indentation cracking of GaAs. In particular, we have demonstrated that the wedge indenter is an appropriate indenter to create precursor cracks of half-penny shape suitable for dicing applications. The principle of the wedge indentation for such purpose has been subjected to a U.S. Patent application¹. The following paragraphs summarise the different contributions of this dissertation.

7.1.1 Indentation Cracking in GaAs

7.1.1.1 Wedge Indenters

The cracking sequence under wedge indenters has been established with the help of in-situ SEM indentation. Along the [110] direction, the nucleation and unstable propagation of the half-penny crack has been correlated to a large pop-in excursion in the load-displacement history which is generally smaller in the orthogonal $[1\bar{1}0]$ direction. Palmqvist cracks nucleates also during loading at the extremities of the wedge indenter. During unloading, both half-penny and Palmqvist cracks progressively close while lateral cracks propagates under the surface and finally emerge at the surface in the last stage of unloading. Chips are formed by the merging of lateral and Palmqvist cracks. Therefore, these chips are usually confined to the indenter extremities.

Experimental evidence of the influence of the indenter radius and the loading rate on the initiation level of the half-penny crack has been given. Using FE simulations of the indentation process, the influence of the indenter radius on the pop-in load has been rationalised in terms of tensile stress present under the indenter. Using simple dislocation dynamic model, the effect of the loading rate on the pop-in load has been rationalised in terms of the yield stress of the material that is increased when the loading rate is increased.

The energetic analysis of the load-displacement histories of 60° wedge indentations has allowed us to evaluate the cleavage surface energy of GaAs as $1.03 J/m^2$. Assuming that plane strain conditions are achieved, the equivalence between the critical energy release rate and the fracture toughness of the material gives a K_{Ic} of $0.53 MPa\sqrt{m}$. Both cleavage surface energy and fracture toughness are in fair agreement with experimental values usually reported in the literature ($0.89 J/m^2$).

A semi-empirical relationship between the size and shape of the half-penny crack and the indentation load has been established on the basis of the CLHPC model. This model has been calibrated over experimental data from 60° wedge indentations. The calibrated model yields values of the fracture toughness K_{Ic} of GaAs ($0.38-0.44 MPa\sqrt{m}$) which are close to the values usually reported in the literature ($0.31-0.49 MPa\sqrt{m}$). This last result suggests that the CLHPC

¹U.S. Patent application: *Method of cleaving a crystalline material*, N° 34503, registered in May 2006 with Bookham AG, Zürich

model calibrated on experimental data is a reliable method to predict the size and shape of the half-penny crack with the indentation load.

7.1.1.2 Point Indenters

The crack field and cracking sequence has been established for three type of point indenters: conical, cube corner and Vickers indenters. It appears that, independently of the indenter shape, half-penny cracks that propagate along $\langle 110 \rangle$ directions and Palmqvist cracks that propagate in $\langle 100 \rangle$ directions nucleate and propagate during the loading sequence. Upon unloading half-penny and Palmqvist cracks progressively close and lateral or shallow lateral cracks merge with Palmqvist cracks to create chips that spread-out at the surface generally in the last stage of unloading. The shape of the indenter strongly influences the chipping pattern. Under cube corner indentation, the Palmqvist cracks and chipping patterns follows the three sided symmetry of the indenter. Under conical and Vickers indenters, the symmetry of both Palmqvist and chipping patterns is fourfold.

The prediction of crack growth with the applied load given by the $P \propto c^{3/2}$ relationship is in good agreement with experimental observations for both $\langle 110 \rangle$ and $\langle 100 \rangle$ cracks. However, our observations indicate that the range of load to be investigated must be carefully chosen in order to avoid pronounced chipping-out, which is not taken into account in semi-empirical models. In the case where rather large chipping-out takes place, significant deviations from the model are found.

The comparison of conical and Vickers indentations has confirmed that asymmetric half-penny crack propagation takes place in the orthogonal $[110]$ and $[\bar{1}\bar{1}0]$ directions. Thus $[110]$ cracks (i.e crack that propagates in the $(1\bar{1}0)$ plane) are easier to propagate than $[\bar{1}\bar{1}0]$ cracks. However, it has been also shown that the presence of edges contributes to reduce the anisotropy in crack propagations. Namely, at a given load level, the difference in the crack length between $[110]$ and $[\bar{1}\bar{1}0]$ cracks was much larger with conical indenters than with a Vickers one.

By investigating the propagation of $\langle 100 \rangle$ cracks (responsible of flake formation), we have seen that the Palmqvist crack extension is much more limited when using obtuse apex angles rather than acute ones.

7.1.2 Deformation and Crack Nucleation Mechanisms

In Chapter 5, we have obtained new results about the deformation mechanisms of single crystal GaAs and about the interaction of these deformation mechanism with cracks.

Experimental observations of cross-sections performed with the cathodoluminescence setup have evidenced the large difference in the crack field when the apex angle of the wedge indenter is changed. TEM observations of wedge indentations performed with different apex angles have shown that the apex angle of the indenter influences the nature of the dislocations that are generated (twins, perfect dislocations) and also their arrangement below the indenter (converging or diverging patterns). Concerning the nucleation of microtwins, our observations suggests that microtwinning takes place preferentially under obtuse indenters. These observations also suggest that there is a competition

between the effects coming from the indenter angle and the one coming from the alignment of the indenter along either the $[110]$ or the $[\bar{1}\bar{1}0]$ direction. Thus with a 60° wedge indenter microtwinning takes place when the main edge of the indenter is aligned with $[\bar{1}\bar{1}0]$ and not in the orthogonal $[110]$ direction while microtwinning is the main deformation mechanism under 90° and 120° indentations aligned with $[110]$.

The comparison of the load-displacement curves of two 60° wedge indentations performed along $[110]$ and $[\bar{1}\bar{1}0]$ suggests that the deformation of GaAs by the formation of microtwins rather than by perfect dislocations influences the pop-in feature. In particular, the formation of microtwins along the $[\bar{1}\bar{1}0]$ direction results in a smaller pop-in at crack initiation and hence in a more smooth initiation of the half-penny crack.

Under the 60° wedge indenter, the diverging pattern of dislocations was always associated with a half-penny crack. Although FE simulations and slip line fields models of the wedge indentation shows that there is an intense tensile stress field beneath the indenter, the origin of the half-penny crack nucleation is not clearly understood. There are many indications that the converging pattern of dislocations found under 90° and 120° indenters acts as a plastic shielding process that delays the formation of the half-penny crack. These results suggest that the pile-up of dislocations under the indenter tip is not necessarily a mechanism of crack nucleation since such dislocation pile-up is found under 90° and 120° wedge indentations where the half-penny crack formation is delayed while no dislocation pile-up is found under the 60° wedge indenter.

We have shown that the deformation around point indenters is not uniform and that the pile-up of material follows the shape of the indenter. The transition of the piling-up to the sinking-in behaviour as the indenter apex angle is decreased is mainly explained by the geometrical effect. However, the examination of the dislocation arrangement under the indentation in the case of 120° wedge indentations indicates that obtuse indenters possibly favour a strain-hardening behaviour that would also partially account for the sinking-in behaviour. It has been proved that the shape of the indenter also influences the number of activated slip planes. Point indenters favour the activation of intersecting slip planes and hence promote the formation of new initiation sites for Palmqvist cracks.

7.1.3 Application to Dicing of Commercial Lasers

The practical case study on commercial laser devices has given promising results. We have demonstrated that it is possible to separate properly such devices directly from crack precursors generated by a 60° wedge indenter. The better dicing conditions were obtained with 60° wedge indenters at loads in the range of 500 mN.

Although the level of chipping-out does not fit yet the requirements for industrial production (at least 98% of the lasers with no or extremely small chips), the results are really encouraging. Indeed, in this study, the geometry of the wedge indenter had not been optimised, and the parameters of the production tool used to separate lasers had not been adjusted for indentations.

The pop-in excursion and the slope change in the unloading portion of the load-displacement curve are two interesting features in the context of commercial laser dicing. Both features are related to the formation of the half-penny crack

and they can be used as ways to control that a half-penny crack has been nucleated. To our opinion, the pop-in excursion is a practical way to monitor the wear of the indenter. Namely, as the indenter wears, the radius of the edge generally tends to increase. It has been experimentally shown that, as the indenter radius is increased, the load of pop-in and the pop-in displacement gradually increase. Hence, the indentation with a worn indenter having a larger edge radius will result in a delayed formation of the half-penny crack as well as in a larger first crack after pop-in².

7.1.4 Indentation vs Scratching: Advantages and Drawbacks

7.1.4.1 Advantages

- it is possible to use indentation curves to detect the formation of the half-penny crack and monitor the wear of the indenter;
- for a given indenter geometry, we are able to establish a correlation between the load and the size of the half-penny crack on the basis of the CLHPC model and of only a few calibration experiments;
- in the indentation process, the wear of the indenter is less rapid than in the scratching process;
- the indentation process is less sensitive to small shape variations than the scratching process³;

7.1.4.2 Drawbacks

- the indenter geometry needs to be optimised for indentation (this has already been done for scratching);
- the scratching process is more flexible since the scratch length can be adapted without changing the indenter;
- scratching process might be more rapid than the indentation process (~ 1 second vs *sim* 10 seconds respectively).

7.1.4.3 Practical Guidelines for Dicing of GaAs

- the indenter apex angle must be less than 70° (which is the angle between $\{111\}$ planes);
- the loading rate must be comprised between 10 and 50 mN/s to avoid important lateral cracking;
- the edge radius of an ideal wedge indenter is in the range of 100-200 nm;
- the edge first configuration (see Chapter 4 for details) must be privileged to terminate the wedge indenter.

²We recall that the pop-in length is related to the size of the crack just after its sudden nucleation.

³in the scratching process, the tool is pulled on the wafer surface to create the defect. Consequently, the nucleation **and** the propagation of the crack is dependent on the indenter radius

7.1.5 Original Contributions

While most of the studies in the literature concentrate on either Vickers or spherical indentation, the main contribution of this dissertation is the investigation and the comparison of the indentation cracking behaviour of GaAs for several indenter types. We have established a detailed map of **the morphology of the crack field and the cracking sequence** for wedge, conical cube corner and Vickers indenters.

Indentation fracture modelling has been widely developed for Vickers indentation. Our contribution to this field is the adaptation of existing SIF analysis using weight functions to successfully explore the stable propagation of the half-penny crack under wedge indentation.

In this work, a particular attention has been placed on the deformation and cracking behaviour around wedge indentation of GaAs. The investigation of the interaction between the indenter apex angle, the crystalline structure of GaAs and the resulting deformation mechanism, dislocation structure and cracking behaviour of GaAs has contributed newly to the knowledge of the indentation process of GaAs.

In this dissertation, we have used new experimental techniques. The in-situ SEM instrumented indenter is a major step forward in the field of indentation testing at a microscopic scale. This tool is of a critical importance since it allows to correlate experimental observations and features in the load-displacement curves. The adaptation of cross-sectioning techniques to the special case of GaAs is a new step to the understanding of the subsurface crack field. The unique combination of cross-sectioning techniques, cathodoluminescence and TEM have brought complementary results that allows a better understanding of the cracking mechanisms in GaAs under indentation.

At last, this dissertation is a bridge between materials science, mechanical engineering and production engineering that has contributed to develop practical guidelines for the indentation process as a mean to produce a precursor crack for GaAs dicing.

7.2 Perspectives

7.2.1 Crack initiation and propagation

The investigation of the indentation cracking of GaAs is still an exciting subject as some aspects of this subject are still not understood. Further work could be conducted to address several issues:

Firstly, it would be interesting to introduce the wafer thickness, and more important the distribution of the load along the wedge length, in the CLHPC model. These parameters are of critical importance to refine the predictions of crack growth with the indentation load. In that case, the load is distributed along the wedge length ($2L$) on part of the crack lips as described in Figure 7.1.

The description of the SIF along the crack front with the actual model which is $K = f\left(\frac{a}{c}; \varphi\right) \cdot \frac{P}{c^{3/2}}$ would become:

$$K = f\left(\frac{a}{c}; \frac{c}{L}; \frac{a}{W}; \varphi\right) \cdot \frac{P}{c^{3/2}} \quad (7.1)$$

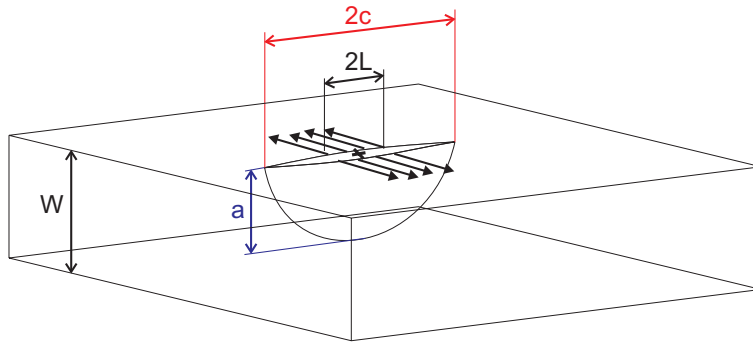


Figure 7.1: The distributed load configuration modelling wedge indentation.

where a/c is a parameter that takes into account the shape of the crack, c/L is a parameter that represents the distribution of the load on the crack through the length of the wedge, a/W is a parameter that takes the thickness of the sample into account, φ is the angular coordinate along the crack front. An advantage of this model over the actual CLHPC configuration should be that once the model is calibrated over experimental data for a given indenter length, this calibration remains valid for other indenter lengths. Furthermore, it is clear that when the crack depth becomes large with respect to the wafer thickness, boundary effects will influence the crack propagation. The introduction of the wafer thickness in the model allows to be free from such effects.

Secondly, it is necessary to conduct further experimental work in order to investigate the effect of the indenter geometry (angle, length, radius) on the initiation load of the half-penny crack. It would be also interesting to implement specific procedures in the experimental setups to measure more precisely the cleavage surface energy from wedge indentation, or the Palmqvist crack extension with the load.

7.2.2 Deformation mechanisms

Concerning the deformation mechanisms under indentations, many interesting points remain unsolved. In particular it would be of high interest to explain the relationship between the apex angle of the indenter and the formation of microtwins. Experiments with 90° and 120° wedge indenters on a (001) face along $[110]$ would be of critical interest for that purpose. It is also necessary to clarify the source of the half-penny crack formation in the case of 60° wedge indentations. The effect of the indenter apex angle on the strain hardening behaviour of the material is also an interesting point to clarify.

Preliminary investigations of 60° wedge indentations on a (110) face have shown that a significantly different cracking behaviour of GaAs is obtained on this face. It would be interesting to explore in more details the indentation of GaAs on $\{110\}$ faces with either wedge or point indenters.

Further understanding has to be gained in order to predict the extension of divergent or convergent structures of dislocations with the apex angle below both wedge and point indenters. A first step in this direction would be to use existing models of the elastic stress fields under wedge or point indentations and

to compute the Resolved Shear Stress (RSS) acting on the different slip systems of GaAs.

7.2.3 In-Situ SEM Testing and Extension of the Work to Other III-V Semiconductors

The in-situ SEM indentation tool serves to explore new fields in materials testing. Thus, the indentation of bulk metallic glasses (Moser *et al.* [1]), the microscratching of GaAs (Wasmer *et al.*[2, 3]), or the compression of micropillars (Michler *et al.* [4]) are some of the fields that are actually explored at EMPA Thun.

Preliminary investigations conducted on Indium Phosphide⁴ have shown that the wedge indentation also produces well defined half-penny crack in this material. As in the case of GaAs, a pop-in excursion accompanies the nucleation of the half-penny crack. Therefore, it would be of high interest to conduct investigations similar to those performed in this dissertation on various semiconductors. Such comparison might be of great interest to clearly understand the different interactions that exist between cracking and deformation mechanisms in semiconductors.

Finally, it would be interesting to see if the principle of the wedge indentation to create a crack of well defined half-penny shape can be extended to other classes of brittle materials such as glasses and ceramics.

Bibliography

- [1] B. Moser, J. Kuebler, H. Meinhard, W. Muster, and J. Michler. Observation of instabilities during plastic deformation by in-situ sem indentation experiments. *Advanced Engineering Materials*, 7(5):388–391, 2005.
- [2] K. Wasmer, C. Ballif, C. Pouvreau, D. Schulz, and J. Michler. Dicing of gallium-arsenide high performance laser diodes for industrial applications: Part i: Scratching operation. *J. Mater. Process. Tech.*, 2007.
- [3] K. Wasmer, C. Pouvreau, J. Giovanola, and J. Michler. Scratching and brittle failure of semiconductor in-situ sem. In E.E. Gdoutos, editor, *Fracture of Nano and Engineering Materials and Structures*, pages 117–118. Springer, July 2006.
- [4] J. Michler, K. Wasmer, S. Meier, and F. Östlund. Plastic deformation of GaAs micropillars under uniaxial compression at room temperature. *Applied Physics Letter*, 90:043123, January 2007.

⁴InP is another semiconductor of the III-V family that has the same zincblende structure as GaAs

Appendix A

Microscopy techniques

A.1 Atomic Force Microscopy (AFM)

A.1.1 Principle

The AFM consists of a microscale cantilever with a sharp tip (probe) at its end that is used to scan the specimen surface. The cantilever is typically made of silicon or silicon nitride with a tip radius in the nanometer range. When the tip is brought into proximity of a sample surface, the forces between the tip and the sample lead to a deflection of the cantilever according to Hooke's law. Depending on the situation, forces that are measured in AFM include mechanical contact force or Van der Waals forces. Typically, the deflection is measured using a laser spot reflected from the top of the cantilever into an array of photodiodes (see Fig.A.1 a)). A feedback mechanism is employed to adjust the tip-to-sample distance in order to maintain a constant force between the tip and the sample.

The AFM employed was a Topometrix TMX 1000 Explorer (Figure A.1 b)) with a tripod scanner. Contrary to other systems, the sample is fixed and the tripod scanner system (X,Y,Z axis) lies in the AFM head.

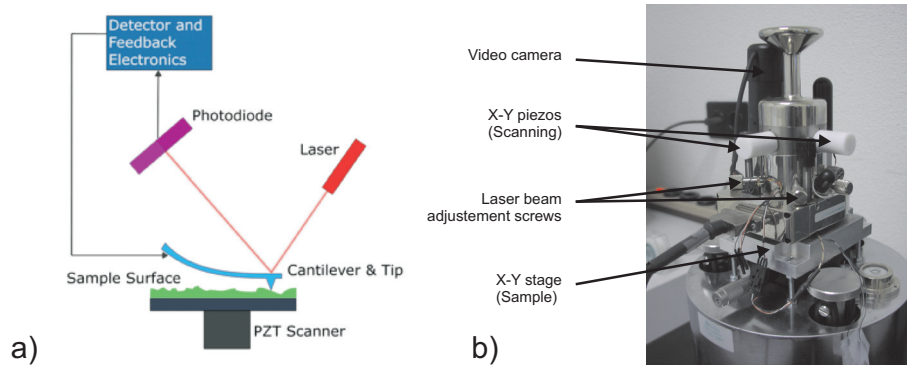


Figure A.1: a) Schematic view of the AFM principle and b) photograph of the Topometrix Explorer head.

A.1.2 Operating Modes

The AFM can be operated in a number of modes, depending on the application.

The primary modes of operation are contact and non-contact modes. In the contact mode operation, the static tip deflection is used as a feedback signal and the force between the tip and the surface is kept constant during scanning by maintaining a constant deflection.

In the non-contact mode, the cantilever is externally oscillated at or close to its resonance frequency. The oscillation amplitude, phase and resonance frequency are modified by the tip-sample interaction forces; these changes in oscillation with respect to the external reference oscillation provide information about the sample characteristics. Schemes for non-contact mode operation include frequency modulation and the more common amplitude or phase modulation. In amplitude modulation, changes in the oscillation amplitude provide

the feedback signal for imaging. The amplitude modulation, non-contact mode was privileged for our observations since it is more sensitive.

A.1.3 AFM/SEM Comparison

The AFM has several advantages over the SEM. Unlike the electron microscope which provides a two-dimensional projection or a two-dimensional image of a sample, the AFM provides a true three-dimensional surface profile. Additionally, samples viewed by AFM do not require any special treatments (such as metal/carbon coatings) that would irreversibly change or damage the sample. While an electron microscope needs an expensive vacuum environment for proper operation, most AFM work perfectly in ambient air or even a liquid environment.

Nonetheless, when compared to the SEM, the AFM is less flexible. Namely SEM width of field goes from the millimetre to the micrometre square range with a better depth of field. In comparison, AFM is restricted to scanning range of 100 micrometer with a depth of field of 12 micrometres. Another inconvenience is that, at high resolution, the quality of an image is limited by the radius of curvature of the probe tip, and an incorrect choice of tip for the required resolution generally lead to image artifacts. The relatively slow rate of scanning during AFM imaging often leads to thermal drift and distorted images. Lastly the adjustment of the feedback loop requires some experiences and is a time consuming task.

A.2 Electron Microscopy

A.2.1 Operating Principle of Electron Microscopes

The basic principle of any electron microscope is detailed on Fig. A.2. In a typical SEM electrons are emitted from a cathode (a) and are accelerated towards an anode (b) forming a beam. The electron beam, which typically has an energy ranging from a few hundred eV to 50 keV, is focused by one or two condenser lenses (c) into a beam with a very fine focal spot. The beam passes through pairs of scanning coils (d) in the objective lens (e), which deflect the beam in a raster fashion over a rectangular area of the sample surface. The interaction of the impinging electron beam with the surface of the sample produces a number of radiations ranging from secondary electrons to X-rays that can be detected by appropriate detectors.

The electron source is divided into two categories: the thermoionic electron gun or the Field Emission Gun (FEG). In a thermionic gun, a tungsten filament or LaB_6 crystal is heated so that electrons are driven off, whereas in the second case it is a strong electrical field that causes electron extraction from the filament.

It is worthwhile to note that FEG sources produce a smaller probe than thermionic guns thus improving the resolution.

Electron microscopes can be divided in two categories, the Scanning Electron Microscope (SEM) and the Transmission Microscope (TEM). Both type can be mixed in the Scanning Transmission Microscope (STEM).

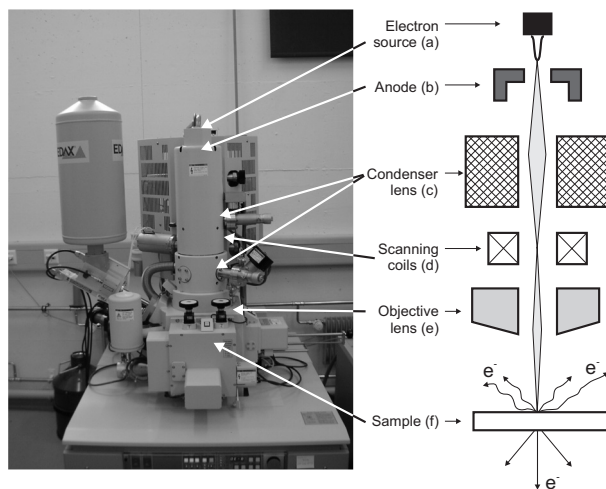


Figure A.2: The Hitachi S-4800 FEG-SEM and the working principle of a SEM.

A.2.2 Transmission Electron Microscope(TEM)

In the TEM, the electrons are accelerated with a voltage of about 200-300 kV. The accelerating voltage determines the energy of electrons in the electron beam and so its wavelength [1]. The higher the energy of electrons is, the smaller their wavelength. Typically, in a TEM, the wavelength of electrons is below the nanometer range. When focused on very thin specimens, part of the electron beam is transmitted directly through the specimen, causing an enlarged version to appear on a fluorescent screen or to be detected by a CCD camera.

Generally, in a TEM, the sample is set between the condenser lenses and the objective lenses as illustrated on Fig. A.3. The image appears on a fluorescent screen that can also be replaced by a CCD camera.

A crystalline material interacts with the electron beam mostly by diffraction [2], although the intensity of the transmitted beam is still affected by the volume and density of the material through which it passes. The intensity of the diffraction depends on the orientation of the planes of atoms in a crystal relative to the electron beam. At certain angles the electron beam is diffracted strongly, sending electrons away from the axis of the incoming beam, while at other angles the beam is largely transmitted. Specific diffraction conditions and apertures placed below the specimen allow the user to select electrons diffracted in a particular direction.

A high contrast image can therefore be formed by blocking electrons deflected away from the optical axis of the microscope by placing the aperture to allow only unscattered electrons through. This produces a variation in the electron intensity that reveals information on the crystal structure, and can be viewed on a fluorescent screen, or recorded on photographic film or captured electronically.

This technique, known as *Bright Field* (BF), is particularly sensitive to extended crystal lattice defects (such as dislocations) in an otherwise ordered crystal. As the local distortion of the crystal around the defect changes the angle of the crystal plane, the intensity of the scattering will vary around the defect.

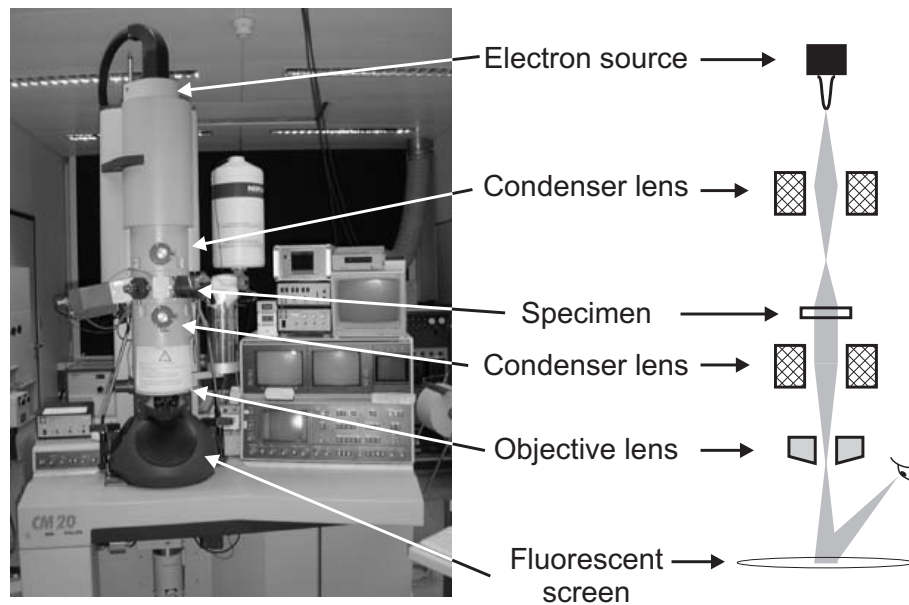


Figure A.3: The CM20 and the principle of the TEM (Source: <http://cime.epfl.ch>)

It is also possible to produce an image from electrons deflected by a particular crystal plane. By either moving the aperture to the position of the deflected electrons, or tilting the electron beam so that the deflected electrons pass through the centred aperture, an image can be formed of only deflected electrons, known as a *Dark Field image* (DF).

In the most powerful diffraction contrast TEM instruments, crystal structure can also be investigated by High Resolution Transmission Electron Microscopy (HRTEM), also known as phase contrast imaging as the images are formed due to differences in phase of electron waves scattered through a thin specimen [3].

The employed TEM were a CM20 from Philips, with a LaB6 source (point resolution 2.8 Å) operated at an accelerating voltage of 200 kV, and a Philips CM 300 operated at 300 kV (FEG source). High resolution images were taken with the CM300 whereas dislocation analysis was made on the CM20 due to its larger tilt capacity (maximum specimen tilt capacity is ± 45 degrees).

Among the drawbacks of the TEM technique, one can cite the often tedious and expensive preparation of samples since lamella need to be thinned down to a few hundred nanometers. Also the sample size is relatively small, raising the possibility that the region analysed may not be characteristic of the whole sample. At last, there is a probability that the sample is damaged by the electron beam, particularly in the case of biological materials, or by the sample preparation (loss of residual stresses for example).

A.2.3 Scanning Electron Microscope(SEM)

Two SEM were employed during this work. The Zeiss DSM 962 served for in-situ indentation testing whereas the Hitachi S-4800 was used for post-mortem

observations.

In the SEM, the primary electrons strike the surface they are inelastically scattered by atoms in the sample. Through these scattering events, the primary electron beam effectively spreads and fills a teardrop-shaped volume, known as the interaction volume, extending from less than 100 nm to around 5 μm into the surface. Interactions in this region lead to the subsequent emission of electrons which are then detected to produce an image.

The most common imaging mode employed here monitors low energy (<50 eV) secondary electrons. Due to their low energy, these electrons originate within a few nanometers from the surface. The electrons are detected by a scintillator-photomultiplier device and by synchronising the signal from the scintillator with the position, a two dimensional image is obtained.

The spatial resolution of the SEM depends on the size of the electron spot which in turn depends on the magnetic electron-optical system which produces the scanning beam (a typical resolution of $\sim 5\text{-}10$ nm is achieved with Field Emission Gun (FEG) sources). The resolution is also limited by the size of the interaction volume, or the extent of material which interacts with the electron beam. The main advantage of the SEM compared to other imaging systems resides in its ability to produce images from the millimeter scale down to the nanometer scale and this with a large depth of focus. Moreover, a variety of available detectors (X-rays, EBSD, ...) are also available which provide many analytical facilities into a single apparatus.

The main difference between the two apparatus employed is the source that is employed to produce the electron beam and the detectors. For the DSM 962, the source is an heated tungsten filament whereas for the S-4800, it is a FEG source. The advantage of the FEG over the tungsten source is the reduced size of the source itself which diminishes the need of subsequent condenser lens and hence reduces the aberrations. Moreover, the in-lens detector of the S-4800 allows to have a working distance from 8 mm down to 1.5 mm, therefore enhancing the resolution.

Bibliography

- [1] D. B. Williams and C. Barry Carter. *Transmission Electron Microscopy: Basics*. Springer, first edition, 1996.
- [2] D. B. Williams and C. Barry Carter. *Transmission Electron Microscopy: Diffraction*. Springer, first edition, 1996.
- [3] D. B. Williams and C. Barry Carter. *Transmission Electron Microscopy: Imaging*. Springer, first edition, 1996.

Appendix B

Methodology for Subsurface Damage Determination

In chapter 4, we have seen that the amount of lateral cracks is dependent on the loading rate. The goal of this appendix is to present the methodology that was used to quantify the level of subsurface damage.

On a piece of wafer, 4 batches of indentations are performed with different loading rate conditions. These indentations are made according to the method of longitudinal cross-sectioning described in chapter 3 (see 3.3.1 for details). Samples are then cleaved on a manual cleavage apparatus following a precise procedure in order to minimise differences in cleavage conditions.

High resolution pictures of the cleaved cross-sections are taken with an Hitachi S-4800 SEM.

After a preliminary set of observations, three indentations are chosen (qualitatively representative of the batch) for each loading conditions. A high magnification ($\times 11.000$) is chosen so that the deepest lateral crack on the more damaged indentation is visible on the pictures. A series of picture is then taken for each indentation and the pictures are subsequently assembled as illustrated in figure B.1.

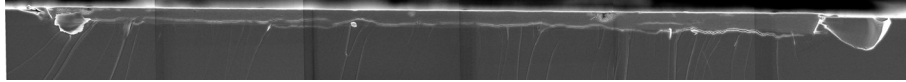


Figure B.1: Assembly of HRSEM pictures of a longitudinal cross-section made with a 60° wedge indenter. Loading conditions: 500 mN, loading rate 1 mN/s and unloading rate 1 mN/s. Width of field $60\mu\text{m}$.

In order to quantify the level of damage, the following procedure is applied to treat the image:

The area of interest under the wedge indentation is delimited. The investigated area is comprised below the edge of the indenter ($55\mu\text{m}$) and is $4\mu\text{m}$ deep.

In the PaintShopPro software, cracks are underlined with a black square marker of size 4×4 pixels in order to enhance their visibility. This size of pencil is taken since it correspond to the mean width of cracks.

The image is then binarised as illustrated in figure B.2. In that picture, dark pixels represent cracks and white pixels represent undamaged material.

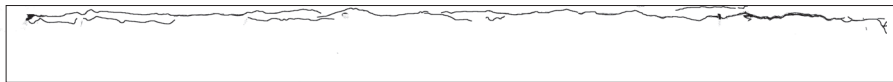


Figure B.2: Binarised HRSEM pictures of the longitudinal cross-section presented in figure B.1. Width of field $55\mu\text{m}$.

Finally, the ratio of black pixels over white pixels gives the amount of lateral cracks present beneath the imprint.

Appendix C

Finite Element Simulations

In this thesis, numerical simulations of wedge indentations have been performed and the results are presented in chapter 4 and 5. The aim of this appendix is to give further details on the modelling using the Finite Element (FE) method. Numerical simulations are performed with the FE commercial code ABAQUS (release 6.5.2) using the CAE interface of the program.

The first goal of these simulations is to look at the differences in the tensile stress relative to half-penny crack opening when we vary the apex angle or the radius of the indenter. The second goal is to identify the major differences in the stress field beneath the indentation that arise when one modifies the apex angle of the wedge indenter.

Despite recent progresses that have been made in the field of contact modelling, we need to simplify the complex problem of wedge indentation of GaAs in order to be able to solve it. The wedge indenter is assumed as sufficiently long to consider that plain strain conditions occur in the middle of the wedge. Although they clearly play a role in the indentation cracking (relatively to chip formation for instance), end effects due to wedge terminations are neglected. The three dimensional wedge problem is thus simplified into a 2D plain strain problem. In addition, due to the symmetry of the problem, only one half of the substrate is modelled.

The substrate is modelled as a deformable solid using a mesh box structure of 3378 quadrilateral elements and 3600 nodes. The metal plasticity model using the Von Mises stress potential simulated in our case necessitates to use either the reduced integration or the hybrid formulation. Consequently, four node quadrilateral elements with either reduced integration (CPE4R) or hybrid formulation (CPE4H) were chosen. The mesh box structure presented in figure C.1 allows to minimise the number of elements (and so the computation time) while keeping a sufficient precision in the area of interest.

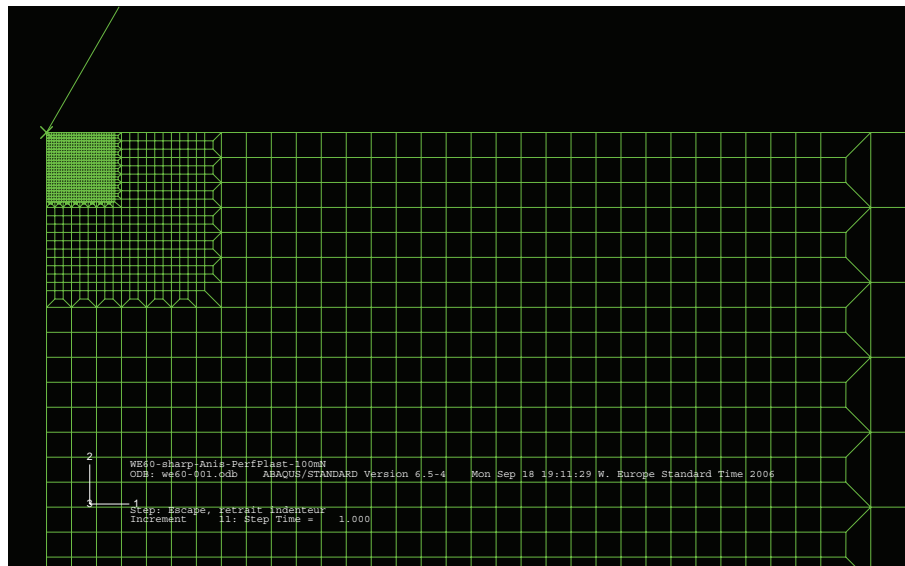


Figure C.1: Picture showing the mesh box structure employed to mesh the GaAs substrate. Note the refined mesh structure in the contact area and the half wedge indenter.

In the contact zone (a square of around $3.6 \times 3.6 \mu\text{m}$), elements are rectangles that are 30 nm wide and 100 nm high. The rectangular shape of elements in the contact area helps to enhance the precision of the interpolation as the substrate deforms. The ratio of width over depth is kept greater than 1/10, according to the recommendations of the manual [1], in order to prevent instabilities. The width of the elements has to be chosen so that the substrate can follow quite accurately the shape of the indenter and this more particularly when using rounded indenters.

Wedges are modelled as rigid solids. Two different apex angles (60° and 120°) and 4 different radius (infinitely sharp, $R=200$, $R=400$ and $R=600$ nm) are simulated.

Elastic and plastic mechanical properties are strongly dependant of the orientation of the crystal and this has to be incorporated into the model. Following the work of Kaajakari [2] the anisotropic elastic stiffness matrix of GaAs is implemented using the *orthotropic anisotropy* option of ABAQUS. We calculate the matrix with the Matlab routine developed by V. Kaajakari, and modified for our purpose. The matrix is oriented so that the [110] direction of the crystal is aligned with the main edge of the indenter, and GaAs elastic coefficients are determined:

$$S_{\text{GaAs},[110]} = \begin{vmatrix} 145.8 & 26.6 & 53.4 & 0 & 0 & 0 \\ 26.6 & 145.8 & 53.4 & 0 & 0 & 0 \\ 53.4 & 53.4 & 119 & 0 & 0 & 0 \\ 0 & 0 & 0 & 59.6 & 0 & 0 \\ 0 & 0 & 0 & 0 & 59.6 & 0 \\ 0 & 0 & 0 & 0 & 0 & 32.8 \end{vmatrix}$$

The plastic behaviour of GaAs is more complicated to implement. The FE method is based on continuum mechanics analysis and aspects of the indentation problem linked to crystal plasticity were not addressed here. Indeed, in GaAs, plastic deformation takes place as a discrete phenomenon oriented along $\{111\}$ slip planes. However, we know that plastic deformation plays a crucial role in the indentation contact problem, and it is necessary to take it into account even if only in a simplified manner. A general plastic behaviour with isotropic hardening is chosen and strain stress values are implemented in the code. These values are obtained from micro-compression tests realised at EMPA by Michler *et al.* on GaAs samples from the same wafer [3].

Stress (GPa)	2.54	2.81	3.10
Plastic Strain (%)	0	0.05	0.13

Table C.1: Plastic strain-stress values obtained from compression tests performed on GaAs micropillars after [3].

In order to validate the model, we have plotted the distribution of the contact pressure under wedge indenters having different radii. Figure C.2 shows the distribution of the contact pressure for a sharp indenter as well as for indenters having a radius between 200 nm and 600 nm. On this graph, data points

from the FE simulations (blue points) are compared to the distributions of the contact pressure derived from the analytical model of Ciavarella *et al.* [4]. When the indenter has a finite radius (i.e. $R=200-600$ nm), the pressure distribution derived from the theory of Hertzian contact takes the form:

$$p(x) = \frac{2P}{\pi a^2} \sqrt{a^2 - x^2} \quad (\text{C.1})$$

where P is the indentation load, a the contact radius and x the coordinate along axis 1 (see Figure C.1).

The pressure distribution given for sharp wedge indenter is derived from the paper of Ciavarella *et al.* [4]. Following this model, the pressure distribution takes the form:

$$p(x) = \frac{2\theta}{\pi A} \cosh^{-1} \left(\frac{a}{|x|} \right) \quad (\text{C.2})$$

where θ is the angle of the indenter, a is the contact radius, and A is the relative Young's modulus:

$$A = \frac{1 - \nu_{mat}^2}{E_{mat}} + \frac{1 - \nu_{indenter}^2}{E_{indenter}} \quad (\text{C.3})$$

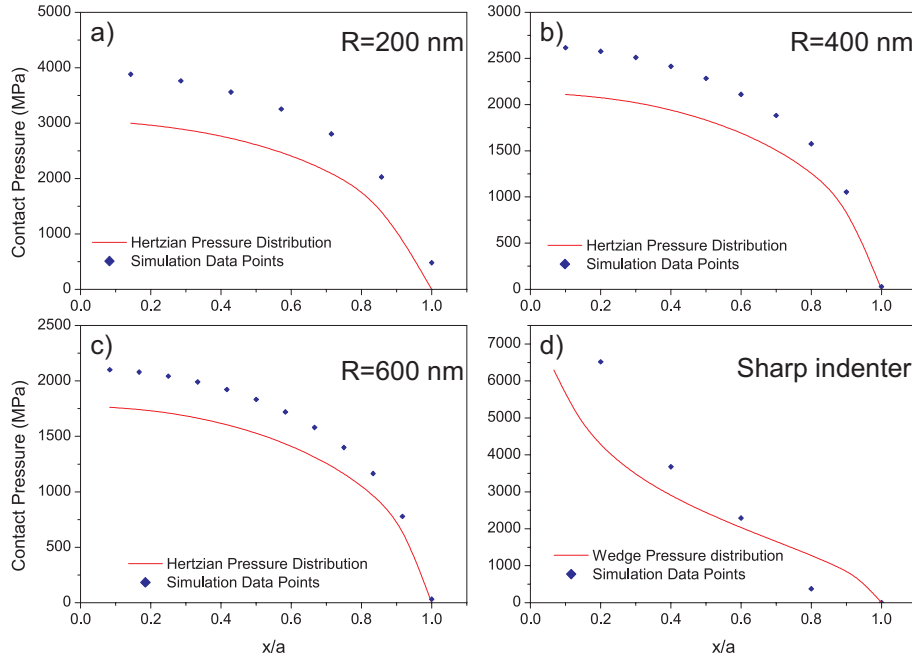


Figure C.2: Contact pressure distribution for 60° wedge indenters with various radii. a) $R=200$ nm, b) $R=400$ nm, c) $R=600$ nm and d) sharp indenter. The abscissa x has been normalised over a , the contact "radius", i.e. the last point of contact between the indenter and the material. When $x/a=0$, the data point is on the symmetry axis, when $x/a=1$, the data point is on the contact radius.

In the case of wedge indenters with a finite radius, we see that FE simulations overestimate the contact pressure and more specifically the maximum contact

pressure in the plane of symmetry of the indenter. As we approach the radius of contact, the error progressively reduces. It is also seen that as the indenter radius is increased, the error between simulations and the model progressively reduces.

When the indenter is sharp, FE simulation deviates significantly from the distribution of the contact pressure given by the model. In both cases (indenter with a radius or sharp indenter) the observed deviations are at least partially accounted for by the large strains that are induced by the acute apex angle of the wedge indenter. Indeed, the models described by Ciavarella *et al.* are formulated from small strain which is not exactly the case especially for a sharp wedge indenter.

Bibliography

- [1] Abaqus Inc. *ABAQUS/CAE 6.5, User Manual*. Abaqus Inc., third edition, 2005.
- [2] V. Kaajakari. Anisotropy of silicon single crystal: a tutorial. Available at <http://www.kaajakari.net>, April 2003.
- [3] J. Michler, K. Wasmer, S. Meier, and F. Östlund. Plastic deformation of GaAs micropillars under uniaxial compression at room temperature. *Applied Physics Letter*, 90:043123, January 2007.
- [4] M. Ciavarella, D.A. Hills, and G. Monno. Contact problems for a wedge with a rounded apex. *International Journal of Mechanical Science*, 40(10):977–988, 1998.

Curriculum Vitae

Cédric POUVREAU

Français, marié, 29 ans

1 rue de l'espérance

69003 Lyon

+33 (0)4 72 36 95 38

cedric.pouvreau@epfl.ch



Expérience professionnelle

- 2003-2007** **Doctorat, EPFL¹ / EMPA² / Bookham AG³**
Étude de la fissuration sous indentation dans GaAs. Application à un procédé industriel de séparation des lasers semi-conducteurs
- 2003-2005** **Projet CTI , EPFL / EMPA / Bookham AG**
Étude multi-échelle de la propagation de fissures dans GaAs (mode I et mode mixte I-III). Développement d'un banc de clivage instrumenté fonctionnant sous vide

Cursus

- 2001-2002** **Université de Rennes 1, France**
DEA mécanique des matériaux (mention assez bien)
Option matériaux fragiles
- 1999-2001** **Université de Rennes 1, France**
Licence & Maîtrise de technologie mécanique

Publications

Articles

Pouvreau C., Drissi-Habti M., Michel K. *et al.*; *Mechanical properties of a TAS fiber: a preliminary study*; Journal of non crystalline solids, **316** (1): 131-137 (2003)

Pouvreau C., Hessler A., Wasmer K. *et al.*, *Dislocations-cracks interactions under wedge indentation in gallium arsenide*, en cours de rédaction.

Pouvreau C., Wasmer K., Breguet J.-M. *et al.*, *In-situ SEM indentation of gallium arsenide: a study of the crack field under wedge and conical indentation*, en cours de rédaction.

Michel K., Bureau B., **Pouvreau C.** *et al.*, *Development of a chalcogenide glass fiber device for in situ pollutant detection* Journal of non crystalline solids, **326**: 434-438 (2003)

Wasmer K., Ballif C., Gassilloud R., **Pouvreau C.** *et al.*, *Cleavage fracture of brittle semiconductors from the nanometer to the centimeter scale*, Advanced Engineering Materials, **7** (5): 309-317 (2005)

Wasmer K., Ballif C., **Pouvreau C.**, Schulz D. and Michler J., *Dicing of Gallium-Arsenide High Performance Laser Diodes for Industrial Applications: Part I: Scratching Operation*, Accepted in J. Mater. Process. Tech.

Wasmer K., Ballif C., **Pouvreau C.**, Schulz D. and Michler J., *Dicing of Gallium-Arsenide High Performance Laser Diodes for Industrial Applications: Part II: Cleavage Operation*, Accepted in J. Mater. Process. Tech.

Conférences, Symposiums

Pouvreau C., Wasmer K., *et al.*, *In-situ Scanning Electron Microscope Indentation of Gallium Arsenide*, 16th European Conference on Fracture, Alexandroupolis, Greece, (2-7 July 2006)

Pouvreau C., Wasmer K., *et al.*, *Indentation fracture of GaAs: dicing applications*, EMPA PhD Symposium, Dübendorf, Switzerland, (19 octobre 2006).

Posters

In-situ SEM indentation of Gallium Arsenide - EPFL Research Days, Lausanne, (Octobre 2005)

Indentation fracture of GaAs: dicing applications - EPFL Research Days, Lausanne, (26 novembre 2006)

Brevet

U.S. Patent application: *Method of cleaving a crystalline material*, N° d'enregistrement 34503, enregistré le 5 mai 2006, conjointement avec Bookham AG, Zürich.